PHD

Self-Propelled Leidenfrost Droplets

Arter, James

Award date:
2019

Awarding institution:
University of Bath

Self-Propelled Leidenfrost Droplets

James Matthew Arter

A thesis submitted for the degree of Doctor of Philosophy

University of Bath

Department of Mechanical Engineering

October 2019

Copyright Notice

Declaration of Any Previous Submission of the Work

The material presented here for examination for the award of a higher degree by research has not been incorporated into a submission for another degree.

Declaration of Authorship

I am the author of this thesis, and the work described therein was carried out by myself personally.

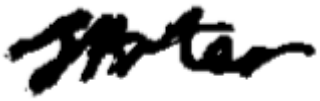

Acknowledgements

I would like to thank my supervisors Andy Rhead, David Cleaver and Kei Takashina for their support and guidance over the course of my PhD. I would also like to thank the technical staff at the university, including but not limited to: Clare and Mat Ball, Andy Church, Paul Reddish, Mike Linham, Jenny Williams and Isabel Wells. My work would have been a lot more difficult without their support.

Finally, I would like to thank my friends and family for their help, love and support. Particular mentions include Tom, for his bus service and sharing my write up pain, Marie, for her liberal views on portion control, Iain, for showing us all how bad it could really be and Alex and Chris, for being in the appropriate time zone for early morning mental breakdowns.

Contents

Abstract

Droplets of liquid in the transition and film boiling regimes can be driven in a direction by viscous drag forces from their own vapour that has been directed by a ratchet toothed surface. To move towards engineering applications of this phenomenon the effects of tooth shape on the dynamics of these droplets must be well understood.

In evaluating the dynamics of droplets, the velocity, reliability, operational temperature range of droplet propulsion and forces acting on the droplet all need to be considered. To accomplish this droplet dynamics have been evaluated experimentally to take data on velocity, reliability and operational range and the simplified case of sublimating pucks have been evaluated in a CFD (Computational Fluid Dynamics) simulation to take data on the forces acting on pucks due to vapour flow.

Previously, to perform experiments on multiple different tooth shapes, many different ratcheted blocks would have to be produced. To remove this problem, a variable ratchet block was designed which uses many thin stacked cards to create a changeable ratchet surface. This allowed for many ratchet shapes to be tested. The most striking result from the experiments performed is the effect of overhang on droplet dynamics. Increasing the overhang angle of teeth is seen to increase the operational range and reliability of propelled droplets.

The CFD model of a dry ice puck above ratchet teeth is set up so that the ratchets can be changed in the same way as the variable block, and thus experimental data points can be matched to modelled ones. The simulation is also set to be periodic in the direction of puck motion, to reduce computational cost. Comparing blocks with overhangs to blocks without overhangs in CFD visualisations of vapour flow reduces the extent of vapour flow in the negative direction, as well as the peak velocity of this flow as compared to the peak velocity of the forward flow. From the CFD simulations it can also be seen that driving force acting on the puck increases as teeth get deeper. As tooth depth increases the puck sits at a lower height, and the gap beneath the puck and the teeth is constricted, increasing the interaction of the flow with the teeth.

Finally, preliminary work on a possible application for self-propelling droplets of a Leidenfrost pipe is described. Such a pipe would have ratchets coating its inner surface. These pipes were found to propel liquid at Leidenfrost temperature in an open system and alter the boiling characteristics of liquid introduced to them in a closed pressurised system. This suggests they may be useful in a cooling application.

Nomenclature

A_s – A surface area a viscous force is acting on.

a – Variable ratchet surface card height.

b – Variable ratchet surface card width.

c_i – Coefficient of inertial resistance.

D – Length of the front edge of a ratchet tooth.

d – Distance from tooth top to puck in CFD simulation.

d_{eq} – Distance from tooth top to puck in CFD simulation at equilibrium.

e – Height of vapour film beneath a droplet/puck.

F_p – Propulsive force acting on a droplet.

F_v – Viscous force.

F_x – Force acting on the bottom face of a puck in the x direction.

F_{eqx} – Force acting on the bottom face of a puck in the x direction at equilibrium.

F_y – Force acting on the bottom face of a puck in the y direction.

f_v – Viscous force per ratchet tooth.

g – Acceleration due to gravity.

H – Length of the back edge of a ratchet tooth.

h – Height of a ratchet tooth.

h_{puck} – Height of a dry ice puck.

k – thermal conductivity of the Leidenfrost test pipe.

L – Total height of the variable ratchet surface block.

l – Capillary length of a liquid.

m – Droplet mass.

N – Number of mesh elements.

P – Ratchet tooth pitch, the distance between one tooth peak and the next.

p – Pressure of vapour beneath a droplet/puck.

q – Heat flux to water in the Leidenfrost test pipe.

R – Radius of a puck.

s – Displacement from the start of a droplet movement.

s_t – The distance between the outer and inner thermocouple in the Leidenfrost test pipe.

T_{subl} – Sublimation temperature of dry ice.

T_1 – Temperature of thermocouple closest to the hotplate in the Leidenfrost test pipe.

T_3 – Temperature of thermocouple closest to the pipe centre in the Leidenfrost test pipe.

t – Time from the start of a droplet movement.

u – Fluid velocity in the x direction.

v – Fluid velocity in the y direction.

v_d – Droplet velocity.

v_m – Mass flow normal speed.

v_t – Terminal droplet velocity.

We – Weber number.

w – Fluid velocity in the z direction.

x – Axis along the length of a ratcheted block encompassing the periodicity of the teeth. Positive in the standard direction of droplet propulsion.

y – Axis extending vertically up the height of a ratcheted block and encompassing the tooth height.

z – Axis across the width of a ratcheted block perpendicular to the central symmetry plane.

α – Variable ratchet surface card cut angle.

β – Variable ratchet surface card tilt angle.

γ – Variable ratchet surface block incline angle.

ΔH_{subl} – Latent heat of sublimation of a puck.

ΔT – Temperature difference between a puck/droplet and a ratchet tooth beneath it.

ε_{dry} – The emissivity of dry ice.

$\varepsilon_{ratchet}$ – The emissivity of a ratcheted surface.

Λ – Length scale of the order of the gap between a ratchet tooth and a droplet/puck that sits on it.

λ – Thermal conductivity of the vapour layer beneath a droplet or puck.

μ – Dynamic viscosity.

ρ – Density of a liquid.

ρ_{CO2} – Density of CO_2.

ρ_{dry} – Density of dry ice.

σ – The Stefan-Boltzmann constant.

τ – Relaxation time of droplet movement.

τ_x – Shear stress acting in the x direction on the bottom face of a puck.

φ – Ratchet tooth front face angle.

ω – Ratchet tooth overhang angle.

List of Figures

1. Introduction

1.1 Overview

When a droplet of liquid is placed onto a surface heated far above the boiling point of the liquid, a portion of the liquid is vaporised and trapped beneath the liquid. This vapour insulates the droplet from the heat of the surface, regulating further production of vapour from the droplet and extending the lifetime of the drop significantly compared to droplets in the nucleate boiling regime. The vapour also greatly reduces friction between the droplet and the surface, by entirely supporting it and lifting it away from the surface. This is known as the Leidenfrost effect, named after and documented by Johann Gottlob Leidenfrost [1].

In many cooling applications, the Leidenfrost effect has been considered a problem as it reduces heat transfer to the liquid due to the insulating vapour layer. Because of this, a good amount of work has been done on the effects of different surfaces and conditions on the Leidenfrost temperature.

Droplets in the Leidenfrost regime were found to self-propel on asymmetrically-ratcheted surfaces in 2006 [2], as shown in figure 1. This propulsion is generally accepted to be due to the asymmetry of the teeth directing the flow of vapour, and this vapour exerting a viscous force on the droplet [2, 3]. The effect can also be used to propel droplets up inclined ratcheted surfaces [2].

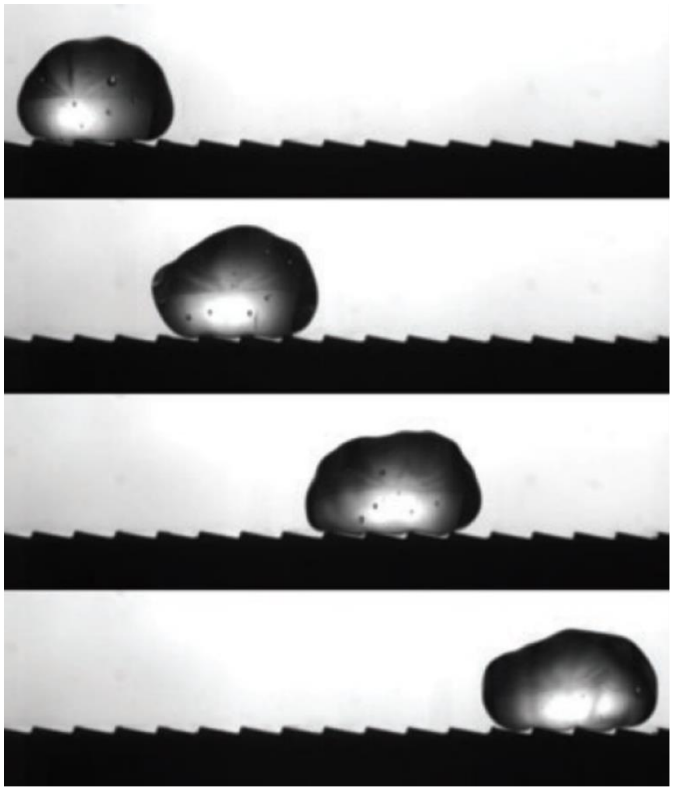

Figure 1. A Leidenfrost droplet being propelled by a ratcheted surface [3].

Sublimating solids, such as dry ice, can exhibit the same frictionless and thermally insulating properties as a droplet at high enough temperature above their sublimation point. As a consequence of this sublimating solids are also propelled on asymmetric ratcheted surfaces [4, 5], as can be seen in figure 2. The important qualitative differences between a droplet and puck include, their shapes, the lack of deformability of a puck and the lack of internal flow in a puck. These factors should be considered when comparing the two.

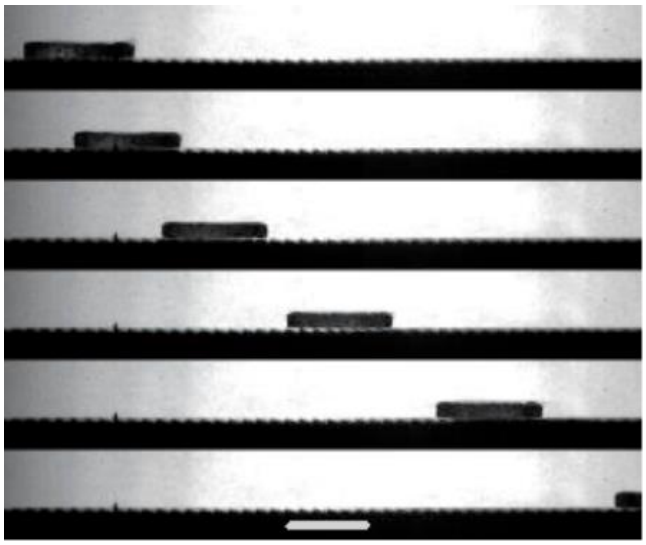

Figure 2. A dry ice puck being propelled by a ratcheted surface [5].

The shape of teeth is an important factor governing the dynamics of propelling droplets. Throughout this work several parameters will be used to describe the shape of the teeth. Figure 3 shows an example overhang tooth profile, with important parameters labelled. H and D are the lengths of the back and front of the tooth respectively. P and h are the pitch and the tooth height. φ is the front face angle of the tooth and ω is the overhang angle.

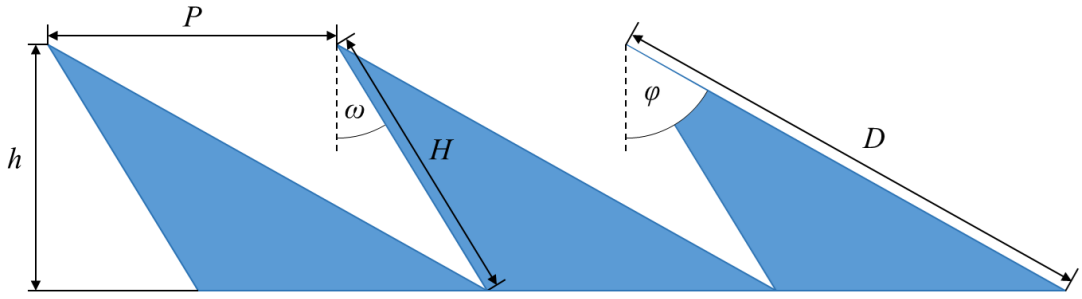

Figure 3. An overhang tooth profile with important parameters highlighted.

This work focuses on gaining understanding of how the shape of the surfaces used affect the movement and reliability or movement of droplets and solids that propel across them, a key step in moving towards industrial applications of this phenomenon. Also presented is an example of an application in a Leidenfrost ratcheted pipe.

Chapter two performs a literature review to explain the background of this work, current understanding of the mechanisms for the self-propelling effect and to highlight the need for this work.

Chapter three focuses on the design of a variable ratchet surface and subsequent experiments with droplets moving on it. The surface allows for a large range of ratchets to be tested, including previously untested overhang geometries, where the peak of a tooth hangs over the trough of the previous tooth.

Chapter four describes the setup and results from a Computational Fluid Dynamics (CFD) simulation of a semi-infinite dry ice puck above a variable ratcheted surface. This simulation was intended as a comparison to the experimental data in the previous chapter. The model considers the equilibrium case, sitting at the appropriate height with appropriate mass flow for the dry ice puck as well as preforming a parameter study across sets of fixed values. Visualisations of the flow beneath the puck are presented and used to help explain the effect of overhang.

Finally, conclusions of the work are given, and possible future work is proposed. A highlight of the proposed future work is the preliminary work performed on Leidenfrost pipes – pipes coated with internal ratchets. These pipes are explored in terms of their ability to propel droplets in the Leidenfrost and transition regime and the effect ratchets have on the heat flux transferred to the liquid within the pipe.

1.2 Aims and Objectives

This work aims to optimise the geometry of the ratcheted surfaces with respect to the droplet velocity and reliability by considering experimental data and a simplified dry ice computational model. The work also aims to investigate a possible application of the phenomenon in a pipe with a ratcheted interior surface.

This gives some specific objectives:

- Perform an in-depth literature review of relevant background work.
- Design and manufacture a variable block to enable the testing of many different ratcheted surfaces.
- Test droplet dynamics on many combinations of surface shapes, temperature and inclination angle using this variable block.
- Create a computational fluid dynamics model of a dry ice puck, which can be considered to be a reduced complexity scenario as compared to modelling droplets, as it removes internal droplet dynamics and deformations.

- Use the computational data to understand the effect of the surface geometry on vapour flow beneath the dry ice puck.
- Use the experimental and computational data to describe and explain trends in droplet dynamic behaviour.
- Design and manufacture a pipe with ratchets on the interior surface.
- Investigate the operation of this pipe in a closed pressurised system at high temperature by comparing it to a pipe without ratchets.

2. Literature Review

2.1 Leidenfrost Droplets

In this section work is considered that researches Leidenfrost droplets on flat planes, studying their shape, dynamics and boiling points in different conditions. A fundamental understanding of these will help inform study about their self-propulsion over ratchets and is by itself useful in any area that requires an understanding of cooling with droplets.

Following a single phase convection regime (see left hand section of figure 4), a boiling droplet can fall into three main regimes, as shown in the boiling curve in figure 4. The lowest temperature boiling regime is nucleate boiling which has the droplet in contact with the surface and bubbling throughout. The highest temperature boiling regime is the film boiling (or the Leidenfrost) regime. Droplets in the film boiling regime do not bubble and have a continuous vapour layer supporting them. Between these two regimes droplets are considered to be in the transition regime. Droplets in this regime bubble and are supported by vapour in a random distribution of areas, which change with time. The extent of this forming vapour layer increases with temperature. There are also two important points highlighted on figure 4. Between the nucleate and transition regimes is the critical heat flux, which is a local maximum of heat flux and local minimum of droplet lifetime. Between the transition and film boiling regimes is the Leidenfrost point. At this temperature the vapour layer fully supports the droplet for the first time [6]. The specific form of droplets depends on their size, with Leidenfrost droplets having a limit in height of twice the capillary length [7]. Droplets in the film boiling

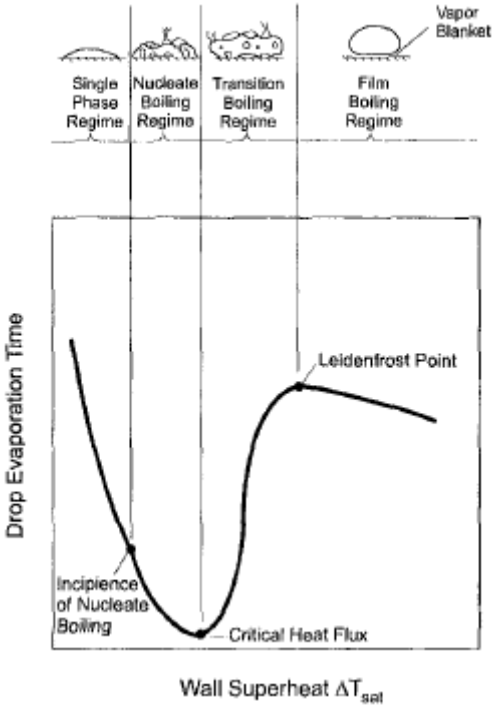

Figure 4. Boiling curve for a stationary droplet [6].

regime are near-spherical with a slightly flattened base at droplet radii well below the capillary length, and flat discs at droplet radii far above the capillary length. The capillary length of a liquid is defined as

$$l = \sqrt{\frac{\gamma_s}{\rho g}}, \tag{1}$$

where γ_s is the liquid surface tension, ρ is the density of the liquid and g is acceleration due to gravity.

A report by Gottfried et al. [8] gives an account of the historical developments of studies on film boiling droplets. A theoretical model of these droplets is developed by considering the heat, mass, force and momentum balance in the top and bottom half of the droplet. Evaporation times are measured for droplets of different liquids and volumes to determine their Leidenfrost point. A sudden increase in evaporation time as temperature increases is indicative of the Leidenfrost point, as heat flux to a droplet drops sharply when it is held off the surface entirely by its own vapour. The temperature of the Leidenfrost point is found to vary strongly with surface material, usually increasing as thermal diffusivity of the surface increases. It is also found to vary weakly with initial droplet temperature, decreasing with increasing initial temperature. The Leidenfrost point is found to vary substantially for water, possibly owing to its large heat capacity. The Leidenfrost point is found to be constant with respect to droplet size for volumes studied. The vapour flow beneath the droplets is found to be laminar.

The effect of surface porosity on the Leidenfrost point and droplet evaporation time was studied by Avedisian et al. [9]. Increasing surface porosity was found to increase Leidenfrost temperature and the temperature range where droplets wet the surface also increases with porosity. With increasing porosity more vapour can be absorbed into the surface, thus requiring a greater evaporation rate from the droplet to provide enough vapour to sustain the vapour layer beneath a droplet. A greater evaporation rate requires greater heat transfer to the droplet. Droplets on a porous surface in the film boiling regime are found to evaporate faster than on an impermeable surface, with this being explained by the droplet being closer to the heated porous surface than the impermeable one.

Bernadin et al. [6] note discrepancies in the literature available for the Leidenfrost point of water and cite pressure, solid surface condition and thermal characteristics and the temperature, size and deposition method of liquid droplets as parameters influencing the Leidenfrost point. The Leidenfrost temperature is measured on different surfaces. It is found that surface roughness increases the Leidenfrost point and suggested that this is due to a rougher surface requiring a thicker vapour layer to avoid surface contact and heat transfer. Surface contamination also increases Leidenfrost point, with deposits acting as nucleation

sites. The temperature of the droplet before surface contact was found to have little effect on the Leidenfrost point. Also of little effect is liquid degassing of the droplet. Previously proposed models of the Leidenfrost point are found not to account for all parameters effectively.

Following directly on from this work, the authors propose a model for the Leidenfrost point based on characterising surface cavity size, bubble growth, nucleation and merging criteria [10]. This model suggests micron scale cavities on the heated surface act as nucleation sites for bubbles within droplets. As temperature increases more, smaller cavities are activated, and bubble growth rate increases. At some maximum point these bubbles merge to form a vapour film. At the Leidenfrost point and higher liquid that would contact the surface is almost instantaneously boiled. Good agreement is found for water on three different metallic surfaces as well as FC-72 on aluminium. The model has worse agreement for acetone tests, suggesting it is still missing some intricacies of the boiling behaviour.

Biance et al. [7] report some important properties of Leidenfrost droplets. Firstly in the film boiling regime, the water droplet itself sits at 99±1°C. Secondly at radius of 1cm^3 or higher droplets become unstable with bubbles of vapour rising through the centre of the droplet – caused by a Rayleigh-Taylor instability, an instability at a fluid-fluid interface where the lower density fluid pushes into and through the higher density fluid. It is proposed this size limit scales with capillary length. Thickness of vapour beneath the water droplet is measured to be on the order of 10-100μm (see figure 5). Film thickness increases with drop radius. This rate of thickness increase is higher below the capillary length than above. As the droplet boils away, this film thickness decreases. The droplet evaporates at a steady rate until the end of its lifetime where there is an increase in evaporation rate.

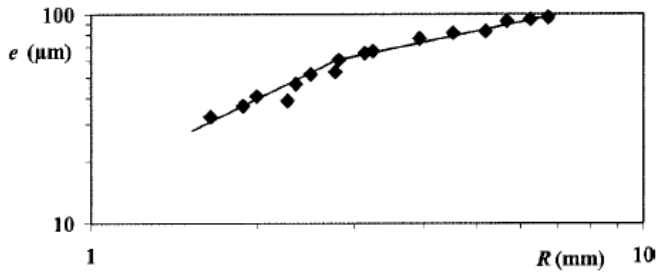

Figure 5. Thickness of vapour layer against droplet radius for a water droplet at 300°C [7].

The effect of contact angle on droplet evaporation time and Leidenfrost point is discussed in work by Takata et al. [11]. It is found that both the evaporation time and the Leidenfrost temperature decrease as the contact angle increases.

Bleiker et al. [12] propose a model for film boiling droplet lifetime based on their shape. Lifetime models are created for droplets at the extremal cases of completely spherical (very small) droplets and large flat disk like droplets. An expression is then given combining these two cases to describe the lifetime of much more common intermediate droplets. This expression is then compared to experimental data from the literature.

A model for the maximum radius of a droplet that can be stably supported by a vapour cushion for small flow rates is described by Snoeijer et al. [13]. The model calculates values of maximum droplet radius that are in agreement with Biance et al. [7] and agrees that the chimneys formed above this maximum radius occur due to a Rayleigh-Taylor instability.

Kim et al. [14] discuss the effects of roughness height, wettability and nanoporosity on the Leidenfrost point. Nanoporosity, in the form of silicon oxide nanoparticles, was found to have the most significant effect raising the Leidenfrost temperature of water on a silicon oxide surface to 359°C (up from 274°C). This was found to promote nucleation of bubbles and rapid bubble growth, resulting in disruption of the liquid vapour interface, and making it harder to maintain a vapour layer. Roughness height, governed by 15 micron pillars, was found to noticeably increase the Leidenfrost point to 325°C. Filaments of water can be observed forming between the surface and the drop when surfaces are coated with micro-pillars, increasing heat transfer and reducing evaporation time. These effects can be combined to increase the Leidenfrost temperature substantially, by coating the micro-pillars with nanoparticles. Wettability had comparatively little effect, increasing the Leidenfrost point slightly.

The geometry layer beneath a Leidenfrost drop has been studied in work by Burton et al. [15]. The shape beneath the droplet is found to be close to independent of surface temperature. A concave vapour pocket forms on the base of the drop for larger droplets, introducing a neck radius and height – i.e. the ring at which the droplet sits lowest above the vapour. This pocket flattens for small droplets. The vapour pocket fluctuates considerably in time and space, and its extent is governed by the droplets size. Examples of smaller and larger droplets interference patterns can be seen in figure 6.

Sobac et al. [16] describe a theoretical model of the shapes of Leidenfrost droplets. The droplet shape, shown in figure 7, has a vapour pocket underneath for larger drops that flattens as the droplet radius decreases (as seen experimentally by Burton et al [15]). Comparison of shape geometry with experimental values from Burton et al. [15] and Biance et al. [7] shows good agreement for most droplet sizes, with larger droplets agreeing less well. Scaling laws based on a defined evaporation number are presented.

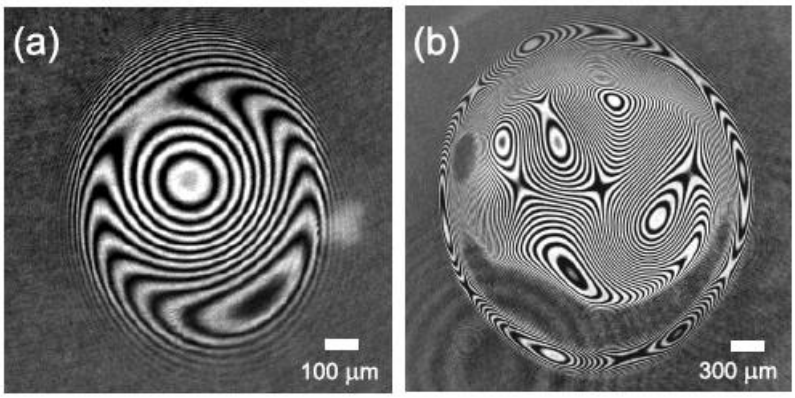

Figure 6. Interference patterns of Leidenfrost droplets of maximum radius 1.2mm (a) and 2.7mm (b) [15].

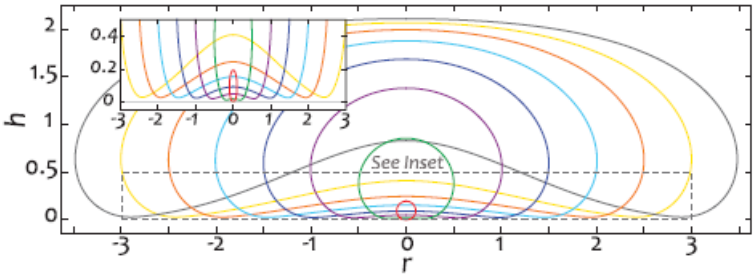

Figure 7. Numerically determined droplet shapes for droplets of different radius [16].

A situation where very small Leidenfrost droplets take off (ascend to a height much larger than their radius) from a heated surface is described by Celestini et al. [17]. This is explained by the breakdown of the lubrication regime at very small values of droplet radius. This breakdown is confirmed by Sobac et al. [16].

Maquet et al. [18] describe the effect of increased gravity on the boiling of Leidenfrost droplets. As gravity increases, droplet lifetimes are found to be shorter. For large drops where vapour instabilities erupt (initially demonstrated in ref [7]), increasing gravity is found to decrease their separation. Gravity increasing is also found to slightly increase the Leidenfrost temperature, with this increase being suggested to be due to a decrease in the neck height previously documented in scaling laws in ref [16].

A capacitive method has been developed to study vapour thickness beneath a Leidenfrost droplet by Roques-Carmes et al. [19]. The electrical capacitance across the vapour layer is measured and linked to a height. This measurement is taken such that the substrate on which the droplet sits is one capacitor plate, the droplet is the second plate, and the vapour layer is the dielectric. This height is measured to be somewhere between the neck height and centre height of the vapour pocket described by Burton et al. [15]. This method allows a continuous monitoring of this vapour layer height, but no way to observe the different heights at the neck and centre of the vapour layer.

The propulsion of Leidenfrost droplets on a flat surface is evaluated by Bouillant et al. [20]. Droplets of radius on the order of a millimetre or less are found to propel in random directions, as opposed to larger droplets which propel in a consistent direction. For small droplets directed propulsion is caused by flow patterns within the droplet (Figure 8b), governed by their initial conditions (for example, dynamics of the needle that dropped them). A single cell of rotating convection is set up. This causes the base of the droplet to be tilted, and thus the levitating force balancing the weight of the drop will have a component in the horizontal, propelling the drop. Larger drops set up two opposing convection cells in this plane (Figure 8a), so no such directional preference is developed. In 3d, this convection pattern is one torus within the droplet. The chosen path of the larger drop is influenced by gravity and a very slight incline on the flat surface they are dropped onto.

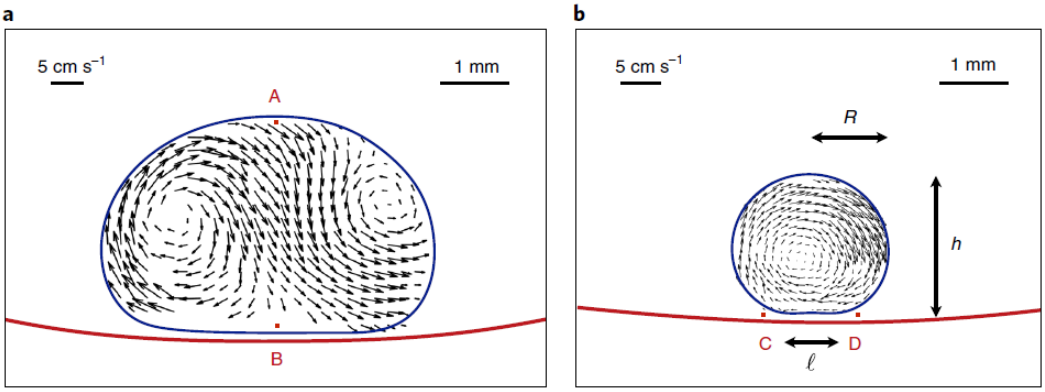

Figure 8. PIV measurements of flow within (a) a large Leidenfrost droplet flattened by gravity and (b) a smaller Leidenfrost droplet with a semi-spherical shape [20].

This section contains work that will be useful in describing interactions between droplets and ratchets. Particularly important is documentation of the shape of droplets and how this shape is governed by their vapour layer, as the shape of droplets is extremely important in the dynamics of self-propelling droplets. Work on the Leidenfrost temperature and how it changes with variables such as surface roughness is important in the context of droplets moving across ratchets, as previously it has been seen transition boiling droplets can behave noticeably different to fully Leidenfrost droplets. This is also useful in the wider context of industrial cooling processes and boiling phenomena, which is likely why it has received so much work.

2.2 Controlling Leidenfrost Drops

This section reviews work to change the Leidenfrost point of droplets, primarily with the aim of supressing this point.

Work by Qiao et al. [21] considers the effect of adding a surfactant, SDS, to boiling water droplets. Surfactants reduce the contact angle of water droplets. In the nucleate boiling regime, bubbles formed increased as surfactant concentration increased. Evaporation time, shown in figure 9, also dropped due to the increase in contact area of the droplets. Leidenfrost temperature was reduced with increasing surfactant concentration, but lifetime of droplets was not changed in the Leidenfrost regime, although more bubbles are generated with increased surfactant concentration. Increasing surfactant concentration reduced heterogeneous nucleation on droplet impact and droplet evaporation time in the transition region.

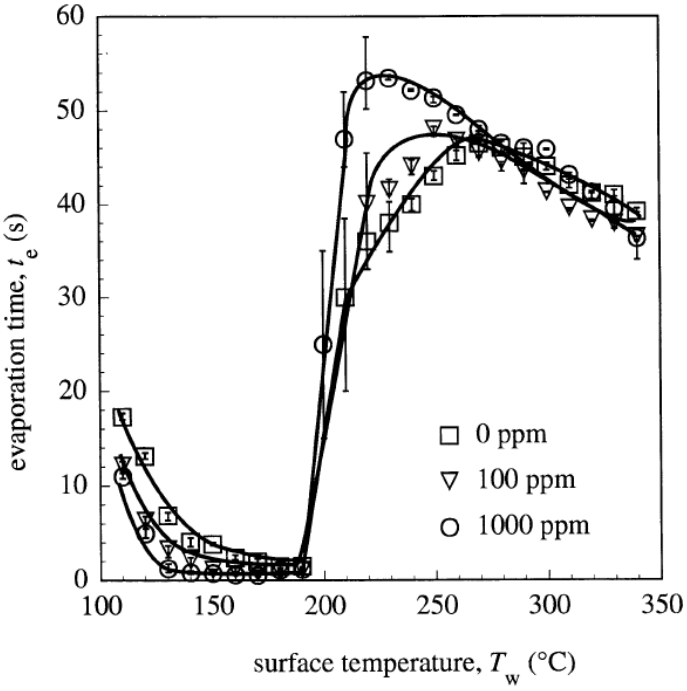

Figure 9. Evaporation time against temperature for three different concentrations of surfactant [21].

Moreau et al. [22] describe Leidenfrost droplets of water and SDS exploding due to the formation of a gel-like shell on the surface of the droplet. This occurs at a specific value of SDS concentration within the evaporating drop. Temperature increase of the drop and the concentration of SDS within the droplet promotes nucleation and fast bubble growth, tearing the shell and causing the explosion. This is only found to occur at temperatures above 250°C.

The effect of an applied electric field to a Leidenfrost droplet is documented by Celestini et al. [23]. Using a similar imaging method to that in ref [15], the vapour layer beneath the droplet was studied. With no voltage applied the authors note the millimetre sized droplet does not

have an axisymmetric vapour layer. As voltage is applied the vapour pocket moves closer to being axisymmetric, and its radius increases. The height of the neck above the vapour layer at the front and back of the droplet is also not the same. Applying a low frequency pulsating voltage to the droplet sees the neck at the front and back of the droplet decrease in height as voltage increases. Conversely the centre of the vapour pocket increases in height explained as the decrease in neck heights increasing viscous pressure beneath the centre of the drop. At a threshold value of voltage, the neck of the droplet contacts the surface, and the Leidenfrost effect is entirely suppressed.

Magnetic fields have been used to control paramagnetic liquid oxygen drops. Piroird et al. [24] propelled liquid oxygen drops in the Leidenfrost regime at small magnets. Scenarios were demonstrated where the droplet had its trajectory changed, and was even trapped in an orbit around the magnet. In some conditions droplet deformations due to the magnet cause energy dissipation via vibrations. And increase in droplet speed is also reported using a planetary slingshot style effect with a moving magnet.

Ng et al. [25] evaluated the effect of low frequency surface vibrations on impinging boiling droplets. Complete suppression of the Leidenfrost effect is demonstrated for a regime where the surface temperature is approximately equal to the static Leidenfrost temperature of the surface and the surface acceleration of the plate is on the order of 10^3 m/s^2. Other regimes are demonstrated that increase cooling with low frequency vibrations of the surface.

Ng et al. [26] consider high frequency vibrations generated by a tip inserted into a Leidenfrost droplet. The vibrations can form capillary waves at the liquid interface and these waves can cause contact with the heated solid surface at high enough tip displacements, effectively suppressing the Leidenfrost regime. Reducing the distance between the tip and the liquid vapour interface and increasing the vibration displacement of the tip increases the suppression effect.

In this section we see a major focus of effort for Leidenfrost droplets is work to change the characteristic temperatures of the Leidenfrost regime, suppressing the effect. This is due to the Leidenfrost effect being a hindrance in many industrial cooling processes, as the vapour film reduces the cooling power of the liquid.

2.3 Droplet Impacts and Bouncing

The impact of droplets is important to consider when performing experiments with Leidenfrost droplets. Impact phenomena will have an effect on any experiment in which a Leidenfrost droplet is dropped. In this section a subset of work, most looking at droplets impinging on flat plates at high temperatures, is reviewed.

Xiong et al. [27] consider impinging droplets of different liquids and sizes onto a hot surface at Weber numbers between 1 and 10. Graphs of evaporation time against surface temperature are displayed all showing a characteristic jump at the Leidenfrost point, with the shape being qualitatively similar across all liquids tested. Small droplets are seen to bounce at temperatures above the Leidenfrost point compared to levitating larger droplets. This can cause droplet lifetime to increase past the Leidenfrost point for very small droplets.

The collision of heptane droplets with a solid flat heated surface at a range of temperatures and a Weber number of 43 has been documented by Chandra et al. [28]. Photographs of the progression of droplets spreading on initial impact are used to describe temperatures effect on these interactions. Droplet spreading on initial impact was found to be independent of temperature, with behaviour splitting with temperature after the first two milliseconds, as can be seen in figure 10. As temperature increases more and more bubble formation from nucleation is seen within the droplet. At and above the Leidenfrost temperature bouncing and rebounding behaviour can be seen, similar to behaviour displayed by Xiong et al. [27] but being displayed here with much more clarity in the photographs.

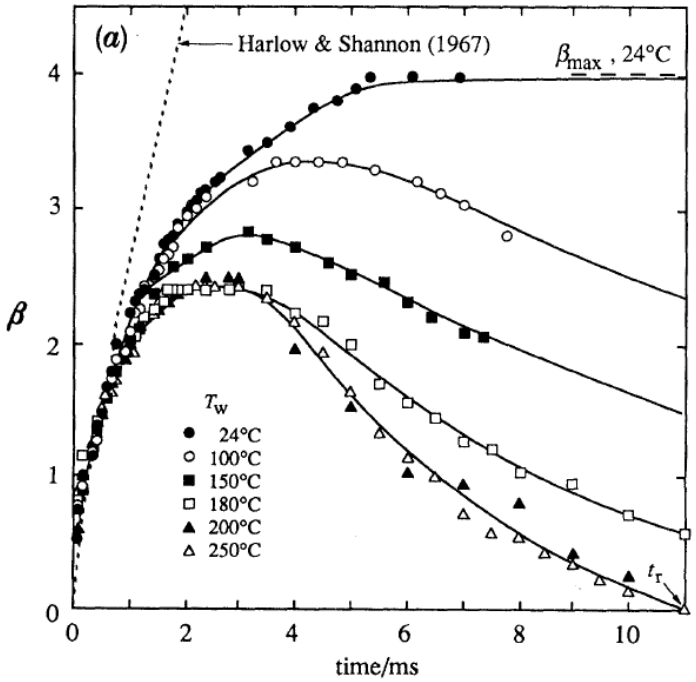

Figure 10. Evolution of the ratio of the impacting droplets liquid film diameter to its initial droplet diameter (β) with time for several different surface temperatures [28].

Bernardin et al. [29] record water droplet impacts across a range of temperatures at three different Weber numbers and document their characteristics and heat transfer properties. Maps of the impact behaviour are displayed for all three Weber numbers, with the behaviour seen at the low Weber number of 20 matching well with what is seen by Xiong et al. [27] and Chandra et al. [28]. More break up of droplets is seen at higher Weber numbers. Weber number is not found to have any significant effect on the point of critical heat flux and the Leidenfrost point.

This work is built upon again by Bernardin et al. [30] extending to different values of surface roughness. Maps of droplet impact behaviour are collected and displayed in the same way as their previous work. Contrary to the behaviour seen in droplets placed on a surface, impacting droplets are seen to decrease in Leidenfrost temperature for increasing droplet roughness. This is explained in terms of the Leidenfrost temperature for impacting droplets being dependant on the pressure beneath the droplet, and higher surface roughness tending to rupture the liquid, reducing this pressure.

Impinging drops are evaluated in terms of droplet velocity and surface inclination by Celata et al. [31]. Increased velocity is reported to decrease Leidenfrost temperature, which would appear to contradict the result from Berndardin et al. [29] that suggests Weber number has no significant effect, and Weber number is proportional to the square of a droplets speed. Leidenfrost temperature is found to decrease with surface inclination.

The formation of holes in the lamella of a droplet impact above the Leidenfrost temperature is considered by Biance et al. [32]. A lamella is the thin film that forms and expands radially from a drop as it impacts a surface. These lamella holes are seen to occur at high Weber number, past some critical velocity, and cause the drop to fragment into satellite droplets. Surfaces with a defect on them cause earlier hole formation in the droplet impact and at lower impact velocities. The size of the defect determines the size of the hole formed.

With this work, it can be seen how most droplets impact on a heated flat surface. However equivalent data appears to be missing for droplets impacting on a ratchet surface. As much as this is specific work it could be very useful in understanding how initial contact of the droplet on the ratcheted surface affects the progression of the dynamics of the droplet.

2.4 Self-Propelling Droplets and Solids on Ratchets

This section considers the mechanisms behind and variations and applications of self-propelling droplets and solids on ratchet surfaces.

Droplets can be self-propelled on asymmetric ratcheted surfaces in both the Leidenfrost regime and the high end of the transition boiling regime [2, 33]. Leidenfrost droplets and sublimating solids self-propel on ratcheted teeth with the same mechanism as one another. The vapour produced beneath the droplet supports it so that it sits on a vapour cushion which in turn sits on the teeth. The further flow of vapour is directed by the teeth, as shown by figure 11. The majority of the vapour moves along the period of the tooth in the direction of droplet motion, whilst descending into the deep part of the tooth. The vapour then flows out either side of the teeth. Most of the outflow occurs at this deep point of the tooth where there is most space beneath the droplet (as indicated by the blue circle in figure 11), however some outflow occurs across the length of the space beneath the droplet. There is also some backwards flow at the apex of the tooth, which escapes outward in the same way as the forward flow. The flow in both the forward and backward direction exerts a viscous force on the underside of the droplet [2, 4, 5, 34]. The balance of these forces in a propelling drop on a ratcheted surface generally pushes the drop forward along the tooth but some tooth shapes can reverse this direction [35]. The flow of vapour beneath a droplet or puck is pressure driven (Poiseuille flow).

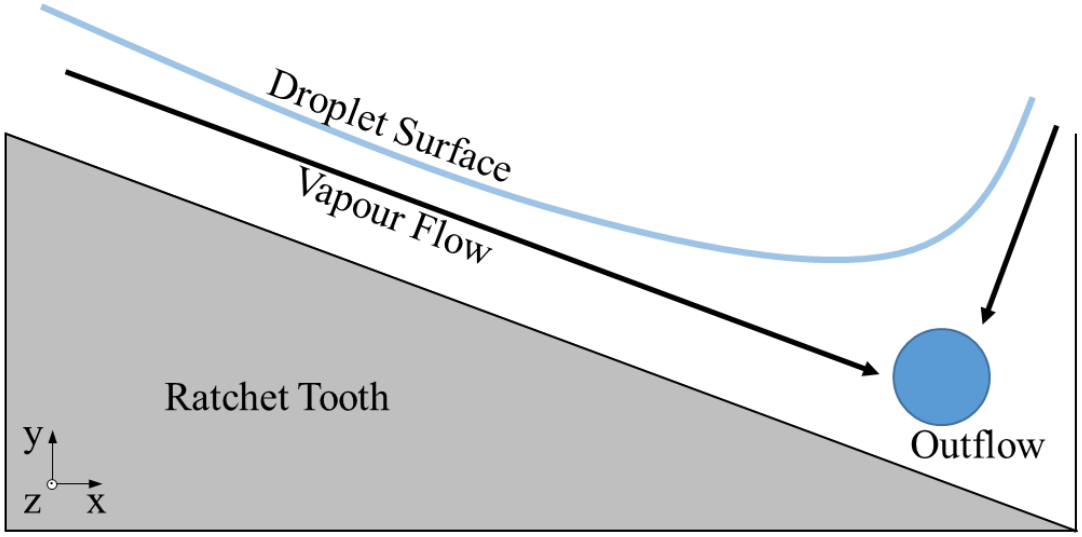

Figure 11. Vapour flow direction beneath a droplet and above a ratchet tooth. Blue circle represents point of maximum lateral outflow.

The standard form of a viscous force acting on a surface due to a moving fluid is given as

$$F_v = \mu A_s \frac{\partial u}{\partial y}, \tag{2}$$

where μ is the dynamic viscosity, A_s is the surface area the force is acting on and u is the fluid velocity in the direction of the force (the x direction in the case of figure 11). Dupeux et al. [34] give an equation for this driving force in the simplest case of a self-propelling dry ice puck, expressed as a force per tooth

$$f_v \sim \frac{\mu u}{e} RP, \tag{3}$$

where, e is the vapour film thickness, R is the radius of the dry ice puck and P is the ratchet period. The velocity of the vapour in this cases scales as $(d^2/\mu)(dp/dx)$, where p is pressure of the vapour. Linke et al. [2] give a very similar viscous driving force for a droplet using a parallel plate model

$$F_v = 0.5 A_s e \left|\frac{dp}{dx}\right| \cos\varphi, \tag{4}$$

where φ is the front face angle of the tooth.

2.4.1 Mechanisms

Some competing theories on the mechanisms behind droplet and sublimating solids have been put forward. The first report of self-propelling Leidenfrost droplets on a ratcheted surface is given by Linke et al. [2]. Crucially, the mechanism for the self-propelling droplets is put forward here as the viscous force interaction described at the start of this section, but the article contains many interesting and important initial observations of the phenomenon. As well as the viscous force, thermocapillary flow is noted as important, with superhydrophobic ratchets propelling droplets at temperatures less than the Leidenfrost point being predicted. Terminal velocities of droplets are found to be on the order of several cm/s. Droplets of various types of liquids are found to propel including water, nitrogen and ethanol. Ratchets of pitch between 1 and 3 mm and tooth height of between 0.1 and 0.3 mm are used to propel droplets. Droplets of radius less than 30% of the pitch do not propel, but droplets with radius much larger than the tooth pitch do. It is noted that, whilst moving, larger droplets tend to elongate in the direction of forward motion. Droplets given an initial velocity in the opposite direction to the expected forward direction will turn around and propel forwards. Self-Propulsion is shown to occur at the high end of the transition boiling regime, but that there is a large variation in acceleration seen due to the random nature of nucleate boiling events. Slugs of liquid are also reported to move within a flat-bottomed channel with ratcheted sides – with decreasing channel width increasing the propulsion. Finally, a possible application of a ratchet pump powered by waste heat is given.

Dupeux et al. [34] analyse the mechanism behind self-propelling dry ice pucks by considering dry ice pucks sublimating above heated ratcheted surfaces and comparing these with pucks

above flat surfaces. The pucks are held above the surfaces and solid glass beads used as tracers to visualise the vapour flow. Flow velocities are on the order of 10 cm/s. The flow is shown to be isotropic above a flat plate, i.e. equal flow is measured in the forward and reverse directions. For a ratchet the flow is found to be anisotropic, i.e. there is a flow preference in the forward direction (the direction of puck travel on a ratchet). The vapour flow, shown in figure 12, is reported to descend the long edge of the teeth and escape from the sides. The flow is cellular below dry ice – each tooth contributes a part of the force acting on the puck. With this vapour flow, and an estimate of its Reynolds number the mechanism of propulsion for dry ice pucks is concluded to be viscous stress generated by the vapour flow. Driving force acting on the dry ice puck is found to vary linearly with puck height (for constant radius of 0.65 mm) and between 1-100 μN for pucks between 0.75 and 9 mm tall.

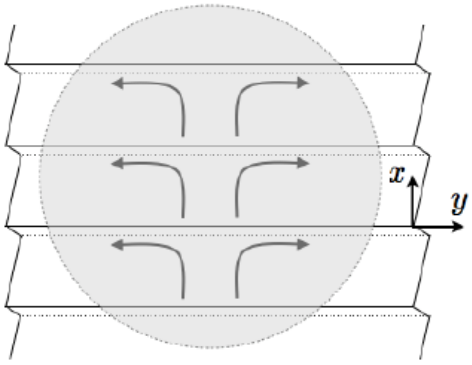

Figure 12. The cellular vapour flow beneath a sublimating Leidenfrost solid on a ratchet. Adapted from ref [34].

This overturns a previous result from Lagubeau et al. [5], suggesting that the propulsion mechanism was jet thrust, whereby mass ejected in the gas propel droplets and pucks forward. Some useful insight remains in this work. Dry ice pucks with ratchets cut into their base are reported to propel along a flat surface in a similar fashion to how pucks propel across ratcheted surfaces. Measurements of the forces propelling droplets of radii between approximately 0.9 and 5 mm are taken and found to be within 1-100 μN. Terminal velocity of drops is evaluated and found to vary with radius, R, as $\sim R^{1/4}$. Droplets with radius less than the pitch do not propel. Symmetric crenellations decreasing the speed of moving droplets that cross them is predicted by estimating the frictional force due to deformations into the teeth dissipating energy. This suggests that sublimating solids would not experience nearly as much friction as droplets.

An alternative theory that was proposed for the mechanism behind droplet self-propulsion is that of thermal creep [36]. This relies on thermal gradients parallel to the tooth gradient inducing flow of gas down the teeth and up the vertical back edges. This flow would push the

droplet or solid from the underside. This description of the propulsion mechanism has been disputed in other work (most notably by Hardt et al. [37]).

Propulsion of droplets across ratchets in the transition regime is investigated in work by Grounds et al. [33]. Three ratcheted blocks are used to test the steepness of incline droplets can climb. The results of these tests are shown in figure 13. The maximum incline droplets can climb occurs at the lower end of the temperature range tested and the sharpest teeth allowed droplets to climb at the highest incline angle. Both these factors indicate that droplets in the transition regime climb inclined ratcheted blocks more readily, with the intermittent wetting contact being suggested as a reason for the droplets increased grip. This work also notes a link between the substructures of a ratchet and the motion of a droplet crossing it. The substructures here refer to the topography on the surface of individual teeth. A machined block with diagonal substructures from cutting is found to change the trajectory of a droplet from falling off the right of the ratcheted block to falling off the left as temperature increases. It is proposed that at higher temperatures gas flow is driven through these substructures, thus giving a directionality to the gas flow beneath the droplet, and thus the viscous force driving it. At the lower temperatures transition boiling is expected to occur and thus wetting contacts are thought to be the cause of directionality in this regime. Finally the sounds of boiling are analysed in an attempt to determine their differences from flat to ratcheted surfaces and across different boiling regimes.

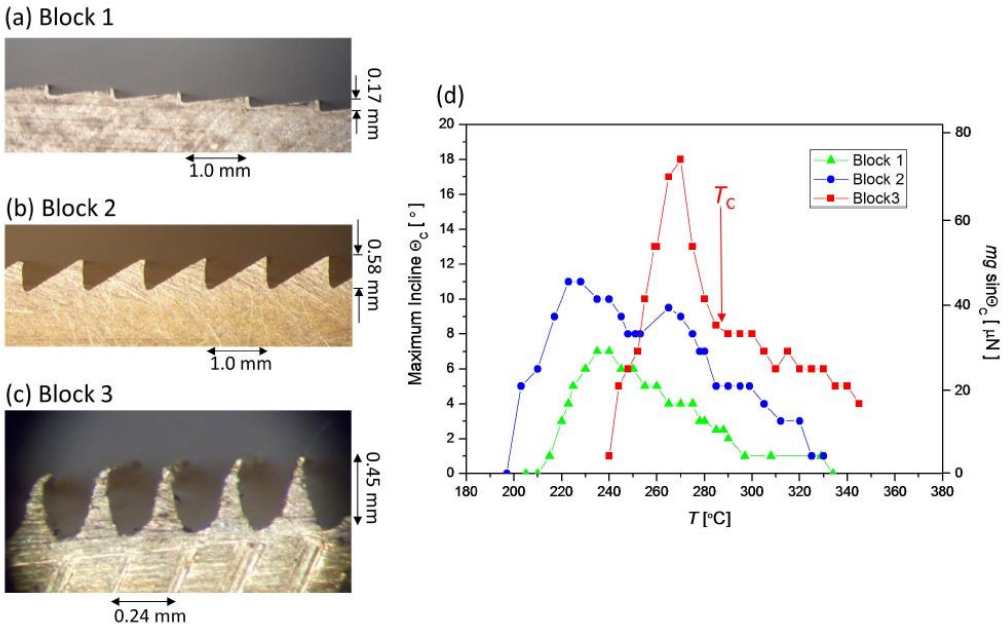

Figure 13. (a), (b) and (c) show the ratcheted surfaces used to propel droplets in collecting data in (d) for the maximum block incline droplets can climb at different temperatures. Droplets travel from right to left. Adapted from ref [33].

Baier et al. [4] describe a model for the propulsion mechanism of Leidenfrost solids over ratchets, based on viscous drag forces of the vapour, and assuming pressure driven flow described by the Navier-Stokes equations in the lubrication regime. The model is solved for a single ratchet groove in 2D and 3D (with periodic boundary conditions from the front to the back of the single tooth) and for a circular puck in 2D. The model is tested against experimental data of shear stress against height of a dry ice puck. The model consistently gives values below those of the experimental values, suggesting the model misses some details of the flow profile. Some scaling of stress values with respect to geometric parameters of the ratchet teeth and the puck is performed and tested with respect to scaling the radius of a puck. This model along with tested experimental data shows decreasing radius increases average shear stress on the puck.

Jia et al. [35] demonstrate conditions in which droplet propulsion direction can be reversed on ratcheted surfaces. Twenty-five ratchet geometries occur of which five can produce droplets that travel in reverse direction at certain temperatures. For those geometries that can reverse there is a temperature at which the drops remain stationary known as the stagnation temperature. A model for this behaviour is described in terms of the deformation beneath the droplet and the effective contact area of the front and back face of each tooth, shown by the red dashed lines in figure 14. This change in contact length changes the direction of vapour flow beneath the droplet (as denoted by the red arrows in figure 14). This allows for a situation where the contribution of force acting in the reverse direction is greater than in the forward direction, reversing the propulsion direction.

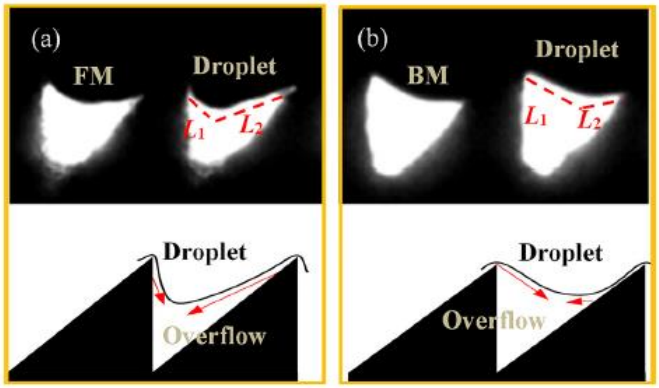

Figure 14. Profile of droplet deformation beneath droplets experiencing (a) forward motion and (b) backwards motion. L_1 and L_2 are effective contact lengths [35].

From the literature discussed in this subsection it is clear that a consensus has formed for the main propulsion mechanism of sublimating surfaces and Leidenfrost drops on ratchets being driven by the viscous force of the vapour acting on the underside of the drop or solid. The impact of the droplet being deformable is suggested, but the full implications of this and the

effect it has on the propulsion of a droplet has not been completely determined. Another area where further work is needed is the effect of the shape of the ratchets and how this changes with the size of the droplets and solids as many of these studies discussed using few droplet sizes and ratchet shapes.

2.4.2 Computational Work

This subsection looks at efforts to model aspects of the mechanisms of self-propelling droplets and sublimating pucks via CFD and other computational methods.

In the work by Baier et al. [4] to describe a 3D model for the propulsion mechanism of Leidenfrost solids, model equations are solved using a finite element discretisation. The results give a velocity profile of the vapour beneath a puck in a single tooth, shown in figure 15. These solutions are for a stationary puck and show both the flow in the *x* direction and the outflow in the lateral *y* direction.

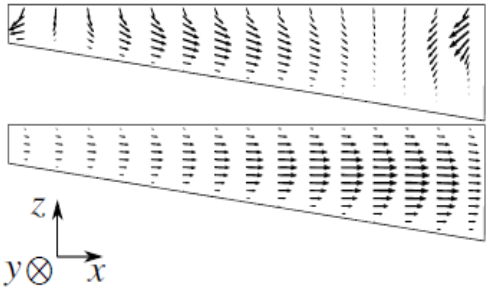

Figure 15. Projected vapour velocity profiles of a single tooth model of a sublimating solid taken halfway between the centre and edge of the tooth in the *y* direction. Top shows *xz* velocities, and bottom shows *yz* velocities. Arrow scales are on the order of a factor of 10 higher for *yz* velocities [4].

In their work demonstrating a ratchet trap, Cousins et al. [38] model a Leidenfrost solid over smooth and ratcheted surfaces by direct numerical solution of the Navier-Stokes equations. The solid is modelled as a disc in air, which has a base that produces a uniform influx of air into the system at a constant velocity. No-slip boundaries are used on the disc and the surfaces. Both problems are modelled exploiting their symmetries, with the flat surface being modelled as 2D and a semi-circular half of a disc being modelled over a ratcheted surface. In the case of a solid above a flat surface, the flow forms a wall jet structure at the edges of the disc. Forces acting on the disc are found to be dominated by viscous traction on the base of the disc. In the case of the ratcheted surface (see figure 16), flow is seen to move towards the deepest part of the tooth then laterally outward, similar to many of the models and predictions from work in the previous subsection and reaches the same conclusion of a viscous mechanism behind the propulsion of droplets. Note the similarities in the velocity profile between the single tooth model previously discussed and the profile about the central tooth in this example, the shape and extent of the *u* flow (velocity in the *x* direction) in particular, and as one might expect the periodically bounded case of the single tooth to have flow similar to the centre point of the finite case.

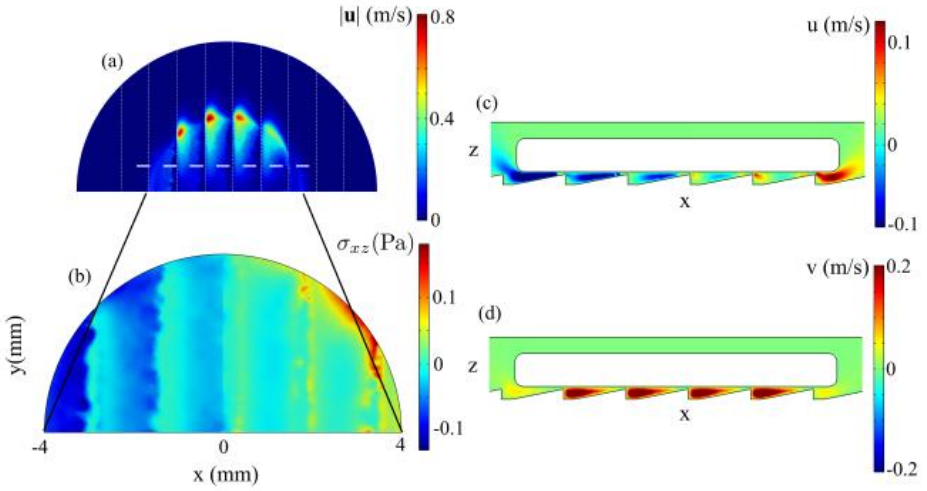

Figure 16. Numerical results of airflow over a ratchet surface. (a) Magnitude of velocity on a plane between the disk and the ratchet surface. (b) Component of in-plane viscous stress in the *x*-direction. Velocity in the *x* (c) and *y* (d) direction along the dashed white plane shown in (a) [38].

Li et al. [39] use Lattice Boltzmann modelling to model small Leidenfrost droplets in 2D. The Lattice Boltzmann method does not use direct numerical solutions of the Navier-Stokes equations, but solves the discrete Boltzmann equation with a collision operator, in this case the multiple-relaxation-time collision operator. This is used to model Leidenfrost droplets (rather than solids as in the previous cases) as well as droplets climbing inclined ratchets. Predictions of this work include a *H*/*D* value of 1/3 giving highest droplet speed for the droplet sizes tested for a specific ratchet shape. It also suggests that smaller droplets can climb larger inclines of ratchets.

Hardt et al. [37] consider the effect of thermal creep flows previously put forward by Würger [36] as a main contributor to the propulsion of Leidenfrost solids. A situation is considered with a 2D ratchet and a solid above it with gas and a thermal gradient between the two, both surfaces being isothermal. No flux of vapour is applied so the only effects driving the vapour will be thermal. The Boltzmann equation is solved, here using a Monte Carlo scheme. Contrary to the description given by Würger [36], vortices form around the back edge of the tooth, seen in figure 17, which shows cases at two Knudsen numbers. The Knudsen number is a ratio of the mean free path of a molecule compared to a representative length scale of the problem being evaluated. For the Navier-Stokes equations to be valid, this number should be very small – smaller than the two cases displayed in figure 17. This thermally induced flow is found to contribute 1.4 and 0.3% (for 17 (a) and (b) respectively) of the pressure induced shear stress acting on the base of the solid. Considering a more realistic situation of a metal ratchet gives dimensionless shear stress values two or more orders of magnitude smaller than in the case of an isothermal surface, effectively confirming the dominance of pressure driven forces in the propulsion of Leidenfrost solids.

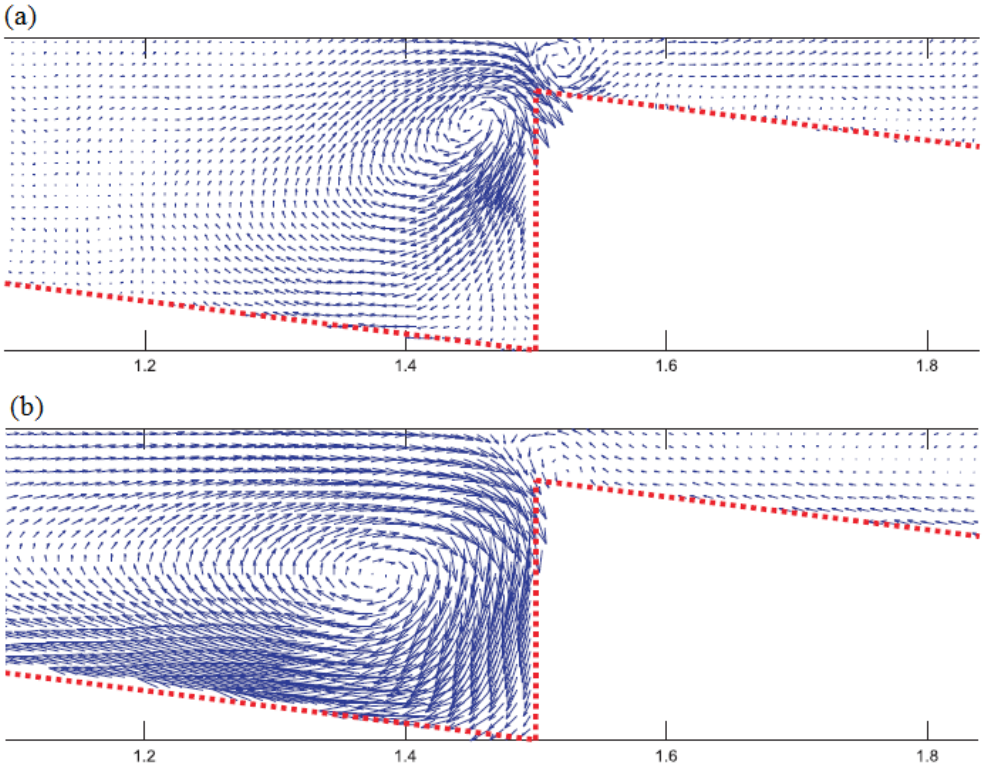

Figure 17. Velocity vectors for flow of vapour driven purely by thermal gradients at two Knudsen numbers: 0.06 (a) and 1 (b) [37].

The limited nature of this subsection shows the opportunity for further computational work to be performed. Of particular use would be more comprehensive work on droplets, especially if this could be managed in 3D, but any widening of the studies here should also be useful. Studies covering variations in ratchet shapes could provide significant data, as generating many different ratchet shapes would be far easier than manufacturing them.

2.4.3 Ratchet Variations

In this subsection, logical extensions of the types of ratchets produced are discussed. Micro and nanoscale ratchets are fabricated and tested in work by Ok et al. [40]. At lower temperatures (the L regime on figure 18), where droplets are in the transition boiling regime, the propulsion speed of the droplets is affected noticeably by the ratchet shape, in this case the period. Droplet velocity increases with decreasing ratchet period. This result is explained by expecting more contact with the tops of teeth by the droplets (as there are more tooth tops beneath the drops at smaller ratchet periods) and thus enhanced heat transfer to the droplets. This explanation fits with similar results presented by Grounds et al. [33] as well as previously discussed work from Hardt et al. [37] which concludes that thermal creep flow could not be a dominant driving force for such small ratchets. Further to this, at high temperature (H regime on figure 18), ratchet size does not significantly affect droplet velocity. It is also noted that

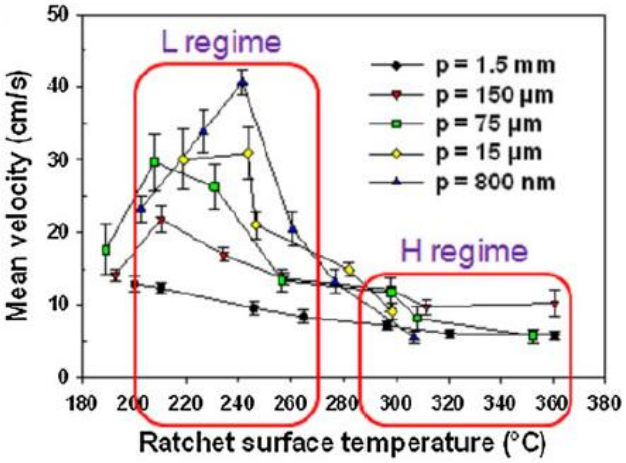

Figure 18. Mean droplet velocity as a function of ratchet surface temperature for ratchets with different periods [40].

droplet velocity is not seen to be affected by droplet size for droplets above the size of the ratchet period. Finally, increasing hydrophobicity of ratchet surfaces reduces the threshold temperature for droplet propulsion, and increases mean droplet velocity.

Work by Marín et al. [41] discusses how droplets at less than the capillary length are propelled across micrometre scale ratchets. Similar to work by Ok et al. [40] it is found that, as temperature increases past the Leidenfrost point, acceleration decreases. This is explained here as the distance between the droplet and ratchet increases and thus the net viscous force acting on the droplet decreases. Comparing to work by Dupeux et al. [34] and Lagubeau et al. [5] who report velocities dropping to zero when droplet size becomes comparable to ratchet period (1.5mm), this work finds a considerable increase in droplet velocity at these droplet sizes (data displayed in figure 19), with large velocity fluctuations due to oscillations in the droplet. The difference noted comes from the size scales involved as at these droplet sizes on micro scale ratchets, there are still multiple ratchets beneath the droplet. Again this result correlates directly with those discussed by Ok et al. [40].

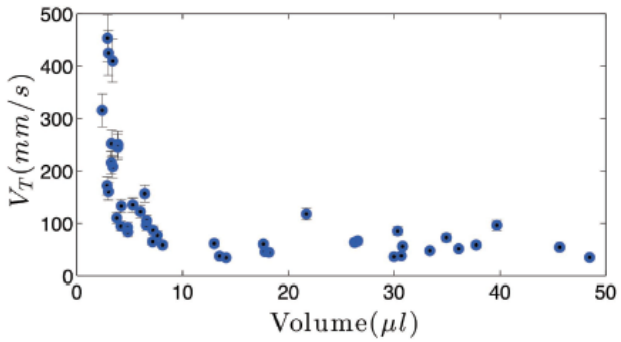

Figure 19. Droplet velocity compared to droplet volume for droplets on micrometre scale ratchets [41].

A ratchet trap is demonstrated by Cousins et al. [38]. This trap is created using concentric circles of inward facing ratchets. Droplets orbit the trap as they move to its centre, in a way analogous to orbits seen in planetary motion. Two main types of orbit are observed, an elliptical orbit for drops with small initial angular momentum and a circular orbit for droplets with large initial angular momentum. Droplets are found to spin in the opposite direction to which they are orbiting. Fission of droplets is observed as well as lobes on spinning droplets.

Further work by Dupeux et al. [42] demonstrates droplets propelling on superhydrophobic surface. With this surface droplets can propel at temperatures much less than the Leidenfrost point, and even temperatures less than the boiling point of the liquid. These low temperature droplets travel at speeds on the order of cm/s slightly lower than a standard self-propelling droplet. At high temperature on a superhydrophobic ratchet, speeds are comparable to those on a standard ratchet. Whilst the prediction of droplets propelling was made in the initial description of the phenomenon [2], the mechanism given there of thermocapillary flow is not the origin of propulsion described by this work. Instead pressure beneath the droplet causes vapour to flow through the micro-channels created by the microstructures on the superhydrophobic surface and, as for a standard self-propelling droplet, this vapour flow imparts a viscous force on the underside of the droplet.

Following on from work from Lagubeau et al. [5] which predicts crenellations slowing down moving droplets, Dupeux et al. [43] investigate this surface topography. Crenellations are found to reduce the speed of the droplets, and with correct geometry and initial droplet velocity, can trap droplets. This can reduce the length in which they decelerate from metres to centimetres. The frictional force is explained as having two components, one from the droplet deformations hitting the side of the crenellations and the second a gravitational component from deforming in and out of the grooves. For shallow teeth the component of crenellation collisions is dominant. Extending to ratchets this frictional force also applies, and is shown to be anisotropic, with droplets moving in the expected direction on a ratcheted surface experiencing twice the frictional drag compared to droplets moving in the opposite direction.

In this subsection the effects of both ratchet scale and droplet size were confirmed to be important for the dynamics of droplets, reinforcing their need for study. Also, the production of superhydrophobic ratchets opens up a new set of opportunities for applications, as it greatly reduces the operational temperature of the phenomenon.

2.4.4 Devices and Applications

This subsection looks at devices and applications of self-propelling droplets and solids on ratchets.

A sublimation heat engine has been demonstrated by Wells et al. [44]. The device (diagram shown in figure 20) consists of a heated turbine like circular metal ratcheted surface on which a dry ice disk, or water droplet supporting a metal disk will rotate. This rotational motion occurs through the same viscous force mechanism that cause droplets and solids to self-propel, with the force applying a torque in the anticlockwise direction. The majority of the energy input as heat is found to be used up in the phase change to vapour, and thus the efficiency of the engine is low (~10^{-6}). A simple electric generator was also created from this heat engine. Finally, the authors suggest microsystems as a possible field to extend thin film boiling systems into, due to their friction reducing nature.

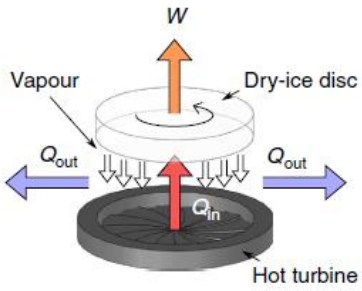

Figure 20. Diagram of a sublimation heat engine [44].

Building on work from Grounds et al. [33] that discussed the influence of ratchet surface substructures on droplet directionality, a Leidenfrost thermostat has been created as shown in figure 21 [45]. The device consists of a ratcheted bar and frame with channels for the droplets to follow when leaving the block. When the block is above the set temperature droplets generally move left and are carried below the block to a mesh to boil away, cooling the system. At or below temperature drops are carried away from the block. The block is demonstrated to have a stable range of temperatures it can operate in.

The transport of a small "cart" on Leidenfrost regime water has been demonstrated by Hashmi et al. [46]. It was found that liquid could hold a mass of 40g. The cart was propelled on an inclined flat block and a ratchet surface. On the ratchet surface, increasing initial water volume supplied to the cart increased its terminal velocity.

This is another subsection where its short length speaks for the need of more work in this area. As the mechanisms are being manipulated more and more, for example with the introduction of superhydrophobic ratchet surfaces and micro-scale ratchets, more applications should be conceived and developed.

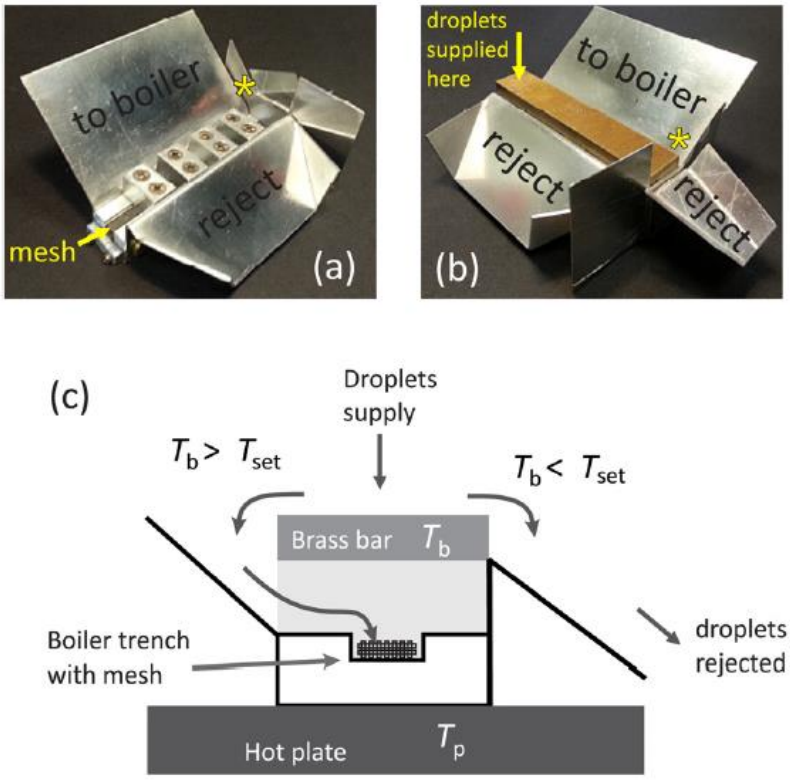

Figure 21. (a) and (b) Photographs of the Leidenfrost thermostat without and with the ratcheted bar. (c) Schematic diagram of the thermostat [45].

2.5 Propulsion on Other Surfaces

Finally, in this section surfaces other than ratchets that propel Leidenfrost and transition boiling drops and solids are considered.

Leidenfrost solids that are distributed unevenly with mass are shown by Dupeux et al. [47] to propel in the direction of the applied mass on a flat surface. The propelling force for dry ice here is an order of magnitude higher than a dry ice puck on a ratchet. It also has the benefit of having no surface variation for the puck to get stuck in. The mass on the puck causes it to sit at an inclined angle across the vapour layer. The pressure due to vapour on the bottom of the puck then propels the puck forward. Rotation can also be induced by linking two pieces of dry ice together with an off-centre rod. The rod induces forward propulsion in the two pucks in opposite directions, with the rod acting as the mass pushing down on each puck. This applies a torque about the centre of the rod.

Titled nanopillar arrays are found to direct droplets in the transition boiling regime in work by Agapov et al. [48]. Leidenfrost regime droplets do not have any directionality on this surface, suggesting asymmetric wettability to be the driving force of this motion. Asymmetric wettability refers to different parts of a structure having different wettability (and local contact angles) and thus changing the amount of surface contact for droplets in the transition regime,

droplets move in the direction of the tilt of the pillars. Decreasing temperature within the transition regime increased horizontal velocity of the drops, in line with achieving more contact with the arrays. There is a limit of Weber numbers where asymmetric wetting propulsion is seen (70-3000 observed in this experiment, with We < 70 showing random motion on the pillars). Velocities were on the order of 10cm/s.

Agapov et al. [49] continue this work by considering the effect of the height of tilted pillar arrays and how this affects the dominant mechanism, and thus direction of the propulsion of transition and Leidenfrost droplets. A summary of findings is shown in figure 22. Below 2µm asymmetric wettability is found to be the dominant effect and droplets travel in the direction of the pillar tilt. Above 2µm the dominant effect is asymmetric vapour flow, and droplets travel in the opposite direction.

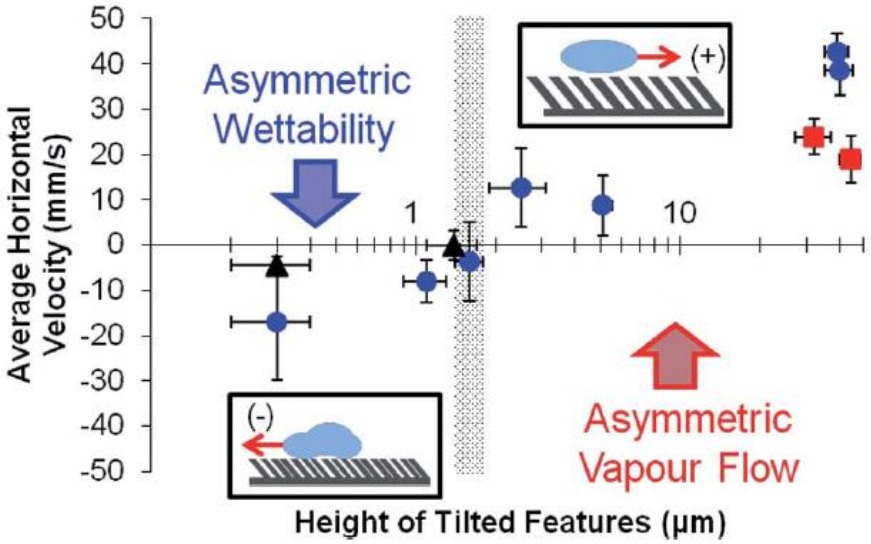

Figure 22. Average velocity of droplets compared to the height of feature on the propelling surface [49].

Kruse et al. [50] detail microstructures that propel Leidenfrost droplets in the direction opposite to that seen in work by Agapov et al. [48, 49] This is suggested to be because the microstructures in this study have no space for the lateral outflow seen in conventional ratchets and thus the vapour would be directed into the microstructures then back out on itself. This is illustrated in figure 23.

Impacting droplets on a surface of micropillars of varying density are studied by Li et al. [51]. The micropillar surface varies along its length in density, keeping pillars the same height and diameter. As a water droplet impinges on this surface between a temperature of 225-290°C, two boiling states exist across the surface, contact boiling in the sparser region and Leidenfrost boiling in the denser region, with a gradient of vapour layer height between them. The droplet

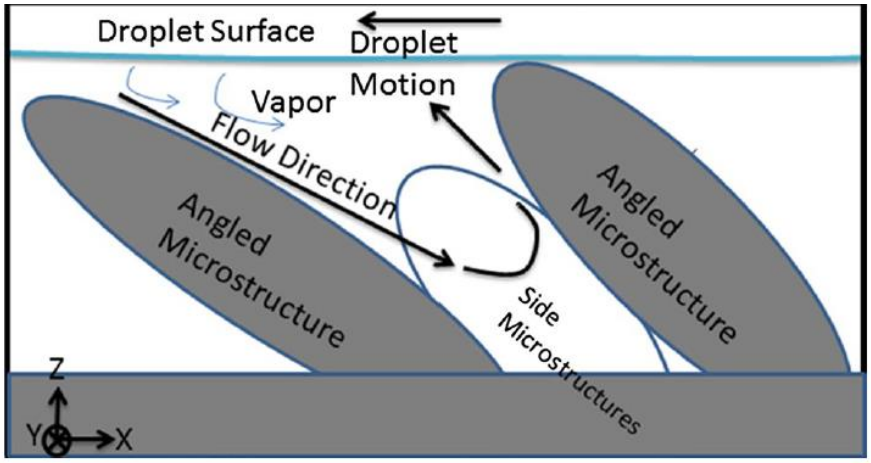

Figure 23. Proposed flow direction beneath a Leidenfrost droplet on angled microstructures [50].

is then ejected from the surface towards the sparser contact boiling region. This behaviour is maintained on an inclined surface.

Soto et al. [52] describe a herringbone surface, seen in figure 24, which can propel Leidenfrost droplets. This works, similar to the ratchets, on the basis of vapour rectification, i.e. vapour being directed by the surface. Maximum droplet speed and propelling force compared to pattern angle are found, both of these exist at a different pattern angle. This serves as a simpler, easier to model example of vapour rectification than the ratchet case.

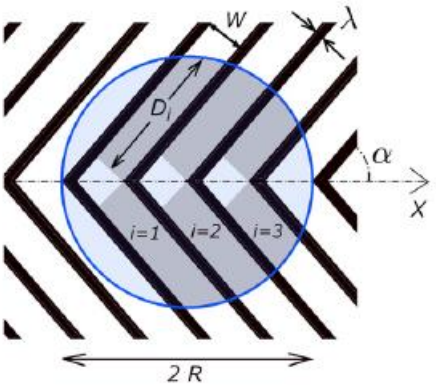

Figure 24. Droplet on a herringbone surface. Droplet is propelled in the x direction. α is the pattern angle [52].

Dodd et al. [53] expand on the herringbone surface design by combining it with a ratcheted surface - i.e. the ratchets form a herringbone arrangement instead of in straight lines across the block. This pattern propels droplets at speeds similar to those of a standard ratcheted block with speeds reported of 330 mm/s for the herringbone ratchet with a front face angle $\varphi = 15°$ compared to 350 mm/s for a standard ratchet block. The herringbone ratchet also has the effect of keeping the droplet centred along the midpoint of the pattern as it is propelled. This allows

for greater droplet control without the use of walls, which can be a source of unwanted random contact boiling events and energy dissipation due to collisions.

All the surfaces considered in this section work on either flow rectification of the vapour beneath the droplet, or some version of asymmetric wettability. Many of the cases driven by flow rectification give weight to the idea that the ratchet mechanism is also flow rectification, given that most ratchets do not work on the length scales asymmetric wettability works on. It is also possible the phenomenon of asymmetric wettability has an effect on the dynamics of droplets moving across ratchets in the transition regime, if the ratchet has a non-uniform roughness, as suggested by Grounds et al. [33].

2.6 Summary of Review

With the self-propelling Leidenfrost droplets being a relatively recent discovery, the current literature available on them can be limited. A description for the underlying mechanism is in place and consistent across much of the work reviewed, but some questions have not been answered. The effect of the deformable nature of the droplets when compared to Leidenfrost solids is a complicated topic, and one that has not been fully explored. The full extent of the effect of droplet size and ratchet shape on droplet dynamics also has room for expanded work, with most current studies only considering a few of each variable at most. With such little data available it can sometimes be difficult to compare like for like data within the literature, with few studies matching in droplet size or ratchet shape.

Computational modelling work was the smallest subsection of literature detailed and as such any broadening of this area will be useful. In particular studies are generally limited to modelling pucks of dry ice in only one or a few ratchet configurations. Any study considering more ratchet shapes or modelling droplets will be impactful.

There are also few devices demonstrated that use self-propelling droplets or solids. There is clearly room for expansion in terms of proof-of-principle devices, and even suggestions on possible devices within the literature reviewed.

To gain further perspective on self-propelling Leidenfrost droplets, work was evaluated on Leidenfrost droplets, the Leidenfrost point, suppressing the Leidenfrost effect, Leidenfrost droplet impacts and propulsion across other surfaces. This information will be useful in explaining experimental results and understanding mechanisms of self-propelling droplets. This also highlighted that data has not been collected on the impact of Leidenfrost and transition boiling droplets on ratcheted surfaces.

3. Droplets on a Variable Topography Surface

3.1 Introduction

One of the gaps noted in the literature review was an explanation of how the dynamics of a self-propelled droplet is affected by the shape of the ratchet surface. The velocity, droplet trajectories, reliability and range of operation of different ratchet geometries are studied in this chapter. Documenting these relationships is extremely important for moving towards engineering applications, as a high degree of control will be important with regards to all these variables.

To study this, a problem with the way experimental work on Leidenfrost ratchets has been performed previously needs to be addressed. As mentioned in the literature review, all previous experimental studies have been performed with only a few ratchet shapes. Constructing the ratchets can be both costly and time consuming, even for small samples. A design was therefore conceived for a variable ratcheted surface, based on the principle of a tilting stack of cards, with the edge making the ratcheted surface. The design and operation of this device will be discussed in the next section, but its construction allowed for the testing of many ratchet shapes.

Much of the work in this section has been published in the article reproduced in appendix 1 [54].

3.2 Variable Topography Device

The basic principle of this device is centred on a stack of thin metal cards, seen in figure 25. The cards can be tilted to create a range of ratcheted surfaces. These tilted cards can be cut flat to create another set of cards that will give another range of ratcheted surfaces. Cut plates can also generate ratchet surfaces with an overhang feature, where the trough of the previous tooth occurs after the peak of the next tooth, leaving a triangular gap beneath the tooth peak. This device therefore gives some excellent experimental advantages in that it allows a large range of ratcheted surfaces to be tested as well as accessing the previously untested overhang geometries.

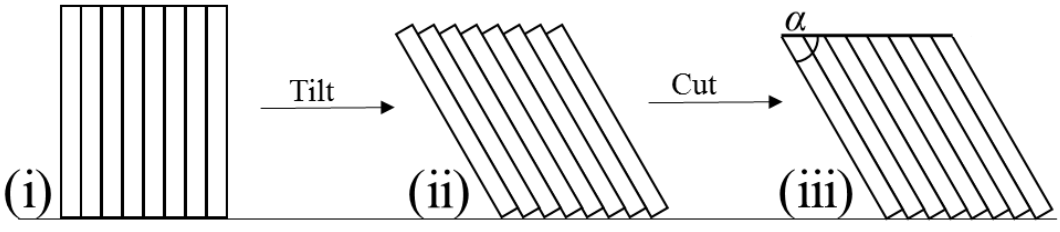

Figure 25. A stack of cards (i) is tilted (ii) and then cut (iii). α is the cut angle.

The principle was realised in the device, shown in figure 26 (a) and (b), that allows a stack of plates to be moved freely and then held rigidly. First, plates were created out of 1mm thick steel gauge plate to ensure consistent plate thickness. Each plate was cut with a cylinder pin either side. The plates were held together in an adjustable frame, with rails along its centre line to fit to the pins on the plates. This kept the pivot points of the plates along the same line whilst allowing them to move back and forwards along the rail. At the ends of the rail were two end bars. These could be tightened with screws to hold the current shape of the plates. In some of the experiments, these end bars were capped with blocks cut to a specific angle to force a certain angle on the stack of plates (there was also a flat cap for holding the plates vertical). The plates were initially ground flat on top, giving $\alpha = 90°$ (figure 25 (i)). α is then decreased by cutting the plates flat at tilted angles (figure 25 (iii)).

Figure 26 (c) shows a representative diagram of the block with most of the relevant variables α is plate cut angle, β, plate incline angle, γ, block incline angle, P, tooth pitch, h, tooth height, L, total block height, and ω is the defined overhang angle (displayed for a negative angle in figure 26 (c)). Two relevant variables not displayed are a, plate height, and b, plate width.

The total block height is used in the experiment to determine values of β. This is calculated as

$$L = \begin{cases} a\sin(\beta) + b\cos(\beta), & 0 \le \beta \le \frac{\pi}{2} \\ a\sin(\beta), & \frac{\pi}{2} \le \beta \le \pi - \alpha \\ a\sin(\beta) - b\cos(\beta) - \frac{b\sin(\beta)}{\tan(\alpha)}. & \pi - \alpha \le \beta \le \pi \end{cases} \tag{5}$$

Pitch and tooth height were used as easier parameters to visualise than cut angle and incline angle. Pitch is calculated as

$$P = b\,\mathrm{cosec}(\beta) \tag{6}$$

and the tooth height as

$$h = |b\,\mathrm{cosec}(\alpha)\sin(\alpha + \beta)|. \tag{7}$$

Overhang angle is defined as

$$\omega = \begin{cases} \beta - \frac{\pi}{2}, & \frac{\pi-\alpha}{2} \le \beta < \pi - \alpha \\ \frac{\pi}{2} - \beta. & \pi - \alpha < \beta \le \pi - \frac{\alpha}{2} \end{cases} \tag{8}$$

Positive ω represents teeth with an overhang, negative represents teeth with an extending back face (or anti-overhang), as seen in figure 26 (c), and $\omega = 0$ represents a vertical backed tooth (or more generally a perpendicular back to the incline angle the entire block sits on). A graph showing the conversion between plate cut angle, incline angle, pitch and tooth height, as well

Figure 26. The device is formed of 1 mm thick plates each with an initial height of ~20mm. (a) plan and (b) side views of the device. (c) conveys key variables, ω is negative in this diagram.

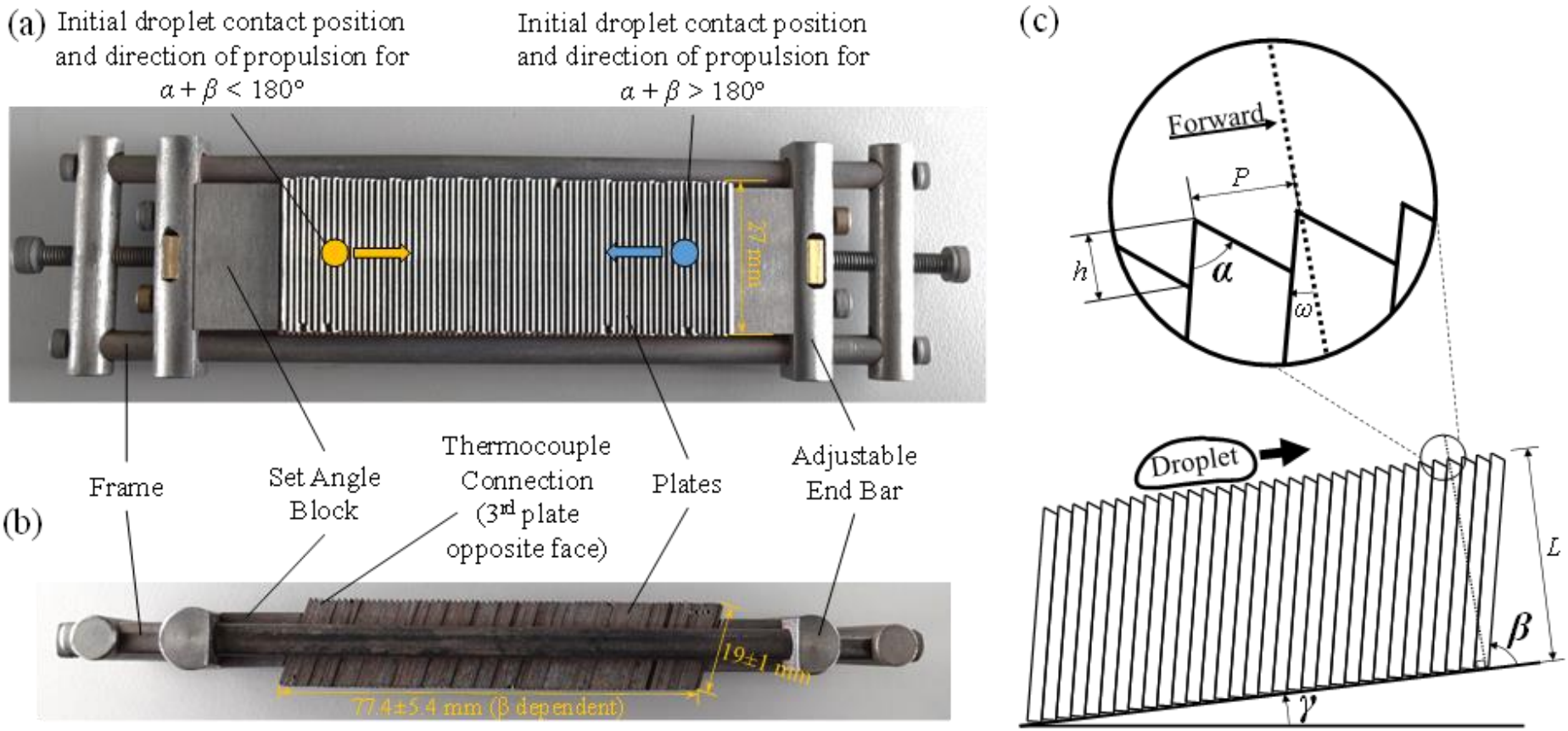

as the operational limits of the device, areas containing an overhang and example cases is shown in figure 27. From the equations 6-8 and this figure, it can be seen that the important parameters of the device (Pitch, height and overhang angle) are entangled – i.e. changing the incline angle changes them all. This is to some extent true of all ratchet shapes, if the tooth height is changed for example, the incline of one or both of the tooth faces, or the pitch will need to be changed to compensate. This problem is, however, exacerbated by having fixed size plates governing the shape of the ratchets. This is one of the negatives associated with making ratchets this way and will make the data harder to evaluate in terms of single ratchet features, and their effects on droplet dynamics.

Also seen in figure 27 is a symmetry across the space of possible ratchet configurations. All configurations below the line of $\alpha + \beta = 180°$ are repeated above the line, with the ratchets facing the opposite direction. In practice this meant for some orientations the entire block needed to be turned around, so the ratchets were facing the correct direction. For the case of flat-topped plates there is also symmetry about $\beta = 90°$, meaning that flat topped plates have a smaller range of unique ratchet shapes than asymmetric plates.

Figure 27. A contour plot of teeth height h as functions of α and β. The pitch P is indicated on the right vertical axis. Shaded areas indicate regions where teeth have an overhang geometry. Diagrams (i) to (viii) illustrate arrangements of plates for specific α and β combinations.

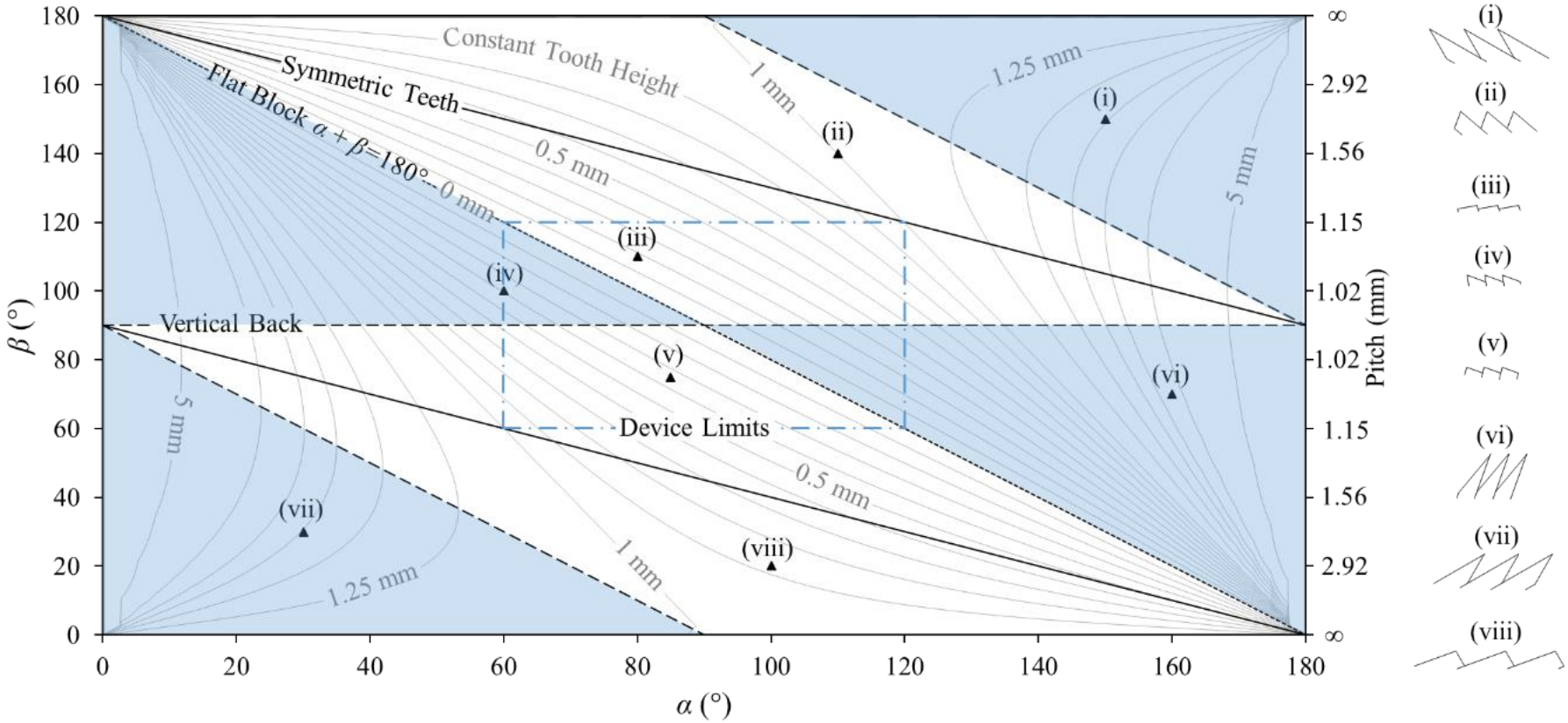

3.3 Experimental Methods

3.3.1 Overview of Main Experiment

The variable ratcheted surface was tested for twenty configurations, split across four α values with five β values for each. These ratchet configurations are displayed in figure 28, a zoomed in version of figure 27 encompassing only the region within the limits of our variable block. The block is placed on a hotplate which was used to vary the block across a temperature range of 200-350°C. The hotplate was placed on a single axis tilting stage to control the incline, of which three values were considered: γ = 0, 2.5 and 5°.

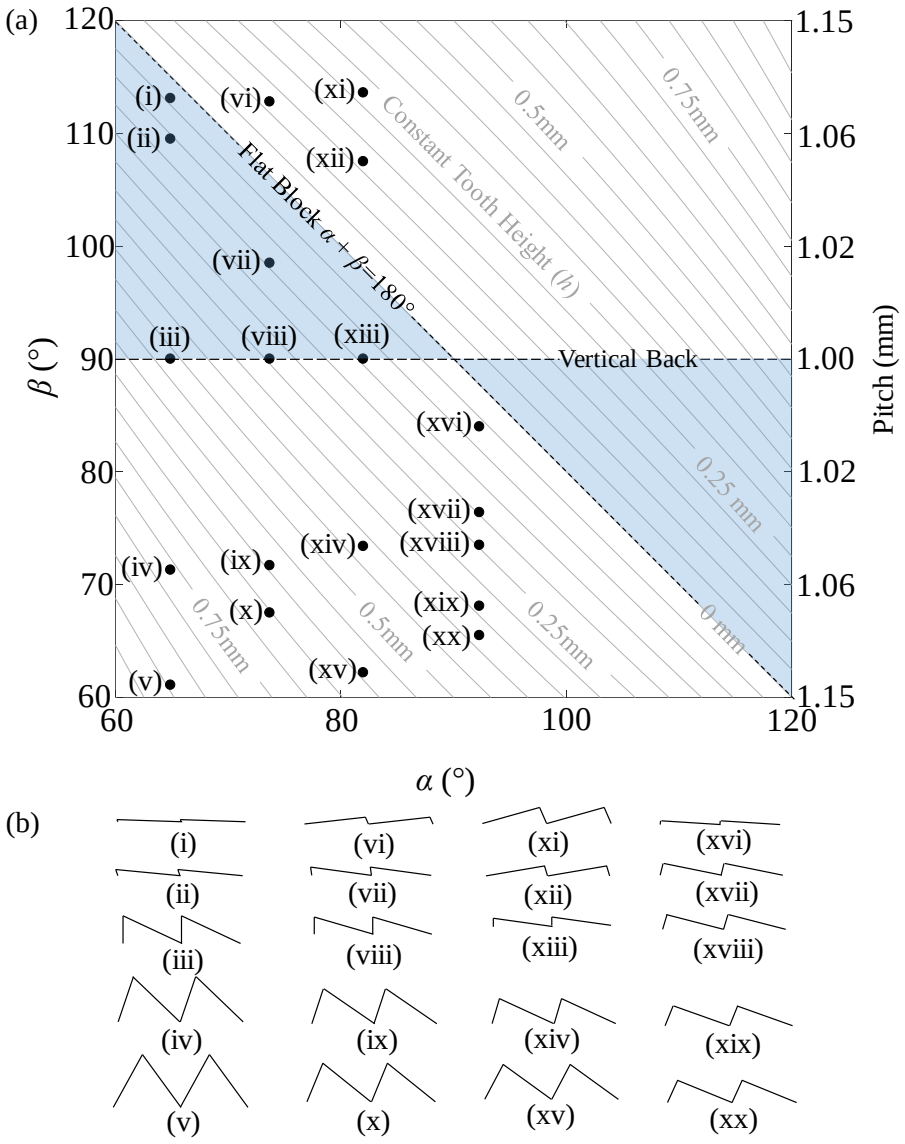

Figure 28. (a) Tooth height and pitch given by varying α and β within the limits of the device. Curves indicate configurations with constant tooth height h. Shaded regions indicate teeth with an overhang geometry. (b) Example tooth geometries from (a).

The temperature of the block was measured using a thermocouple positioned at the indicated spot in figure 26 (a). The temperature of the hotplate was measured with a thermocouple inserted into a drilled hole on its surface. A PID controller used this thermocouple as a reference point to control the temperature of the hotplate.

A peristaltic pump was used to create a slow droplet dispenser. This produced droplets of de-ionised water of 57±3 mg at a rate of roughly 4-5 drops a minute and dropped them at one end of the block, near where block temperature was being measured. Each droplet was filmed by a Nikon D750 camera with a Nikon AF-Nikkor 28 mm f/2.8D lens that was held above the block. A mirror was positioned so both a top-down view and a side-on view, which includes the region underneath the droplet dispenser, could be taken in the same shot. An example shot is shown in figure 29.

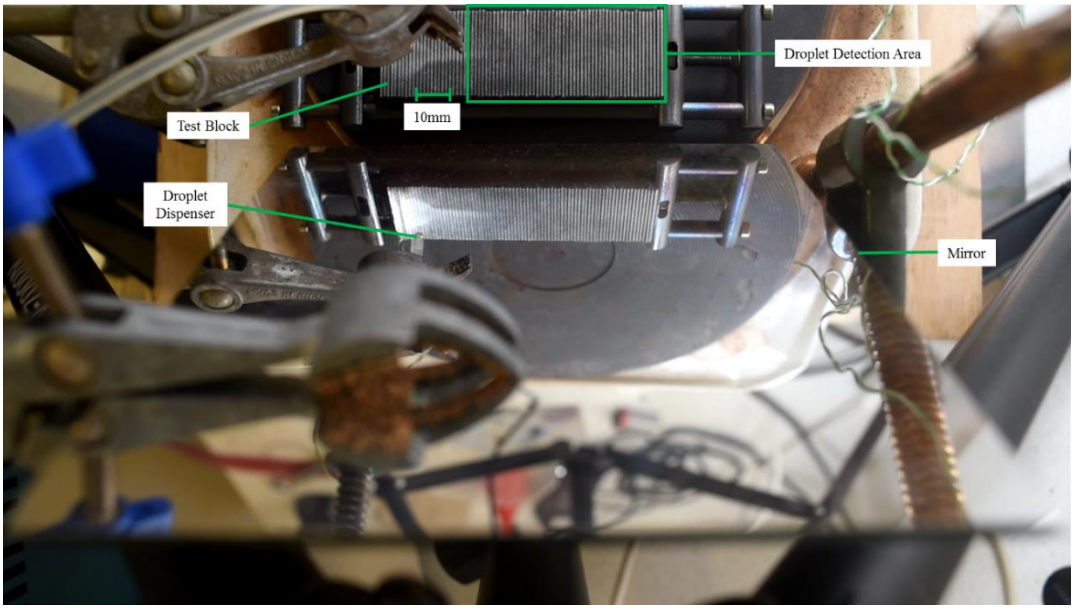

Figure 29. Shot of the experimental setup from the camera used to video droplet trajectories.

Before each test, the variable block was set to a β angle, and L was measured with callipers. If the plates were asymmetric, the direction they were rotated was recorded. The block was oriented on the hotplate with the long edge of the teeth declining forwards, as it was expected the majority of droplets would travel in this direction. The block incline was set with an appropriately levelled digital protractor, accurate to ±0.1°. For each experiment, approximately 100 droplets were dispensed as the block was heated from 200-350°C. A video was taken of this process, and the temperature was recorded for each droplet dispensed. The video was used to extract data on droplet propulsion reliability, trajectories and velocities.

A further experiment was performed with the variable block, taking high speed video footage of droplets moving across it. These videos were recorded side on to the block to try and capture the deformation of the droplets on their underside at 500-2000 fps.

3.3.2 Profilometry and Errors Due to Variable Surface

When taking a value for L, the callipers measured to an accuracy of ±0.02 cm. This error is propagated to β through equation 5, and shown in table 1. Plate thickness was taken as 0.1 cm, with the error on this value being considered small as the plates were made from gauge plate. Plate height was taken as height of the block whilst the plates were held vertical ($\beta = 90°$), so the plate height was also considered to have an accuracy of ±0.02 cm. Note that there was some variation in plate height along the frame, as will be seen in the profilometry data, from slip of the held plates and inaccuracies in the manufacturing process. Care had to be taken on near-vertical plates to ensure that all height variation was accounted for, as there were two separate equations governing L above and below $\beta = 90°$ (see equation 5). For plates that had a direction of rotation recorded, an absolute maximum or minimum bound of $\beta = 90°$ could be set. The alpha variation was found in profilometry data to be very small, and was thus not expected to have significant effect on determining β values.

Alpha (°)	92.3 ± 0.3	82.0 ± 0.3	73.7 ± 0.4	64.9 ± 0.8
Beta (°)	74.9 ≤ 84 ≤ 90	74.8 ≤ 90 ≤ 103	74.5 ≤ 90 ≤ 102	74.1 ≤ 90 ≤ 102.2
	71.2 ≤ 76.4 ≤ 90	69 ≤ 73.4 ≤ 80.2	90 ≤ 98.5 ≤ 104.7	67.2 ≤ 71.3 ≤ 77.4
	69.2 ≤ 73.5 ≤ 80.3	101.2 ≤ 107.5 ≤ 111.6	67.6 ≤ 71.7 ≤ 77.7	105.1 ≤ 109.5 ≤ 112.9
	64.8 ≤ 68.1 ≤ 72.1	109.9 ≤ 113.6 ≤ 116.7	64.1 ≤ 67.5 ≤ 71.6	109.6 ≤ 113.1 ≤ 116.2
	62.6 ≤ 65.5 ≤ 68.9	59.6 ≤ 62.2 ≤ 65.2	108.9 ≤ 112.8 ≤ 116.2	58.4 ≤ 61.1 ≤ 64.1

Table 1. Errors calculated for all α and β combinations.

Profilometry was used to determine α after each cut of the plates. The profilometer measures height variation across a surface, using an optical interference method, and was used to measure the plate sets within the frame set to be held vertically. There will be some slight error associated with this if the plates are not quite vertical. Representative data is shown at different scales and zooms in figures 30-32.

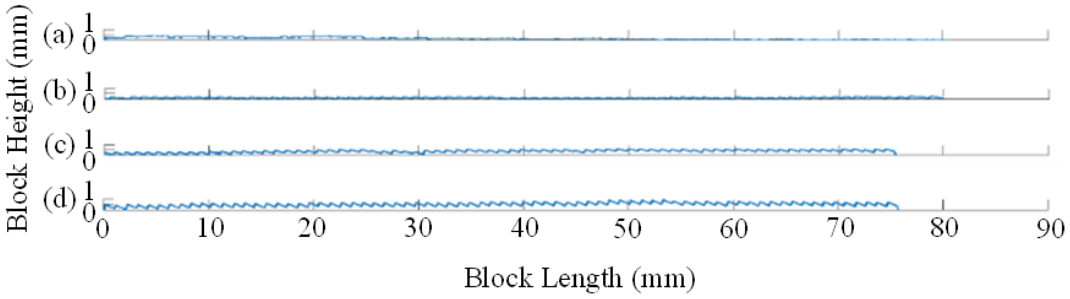

Figure 30. Profilometry data across the entire block on a 1:1 scale. Data taken at $\beta = 90°$ for α values of a) 92.3° b) 82° c) 73.7° d) 64.9°

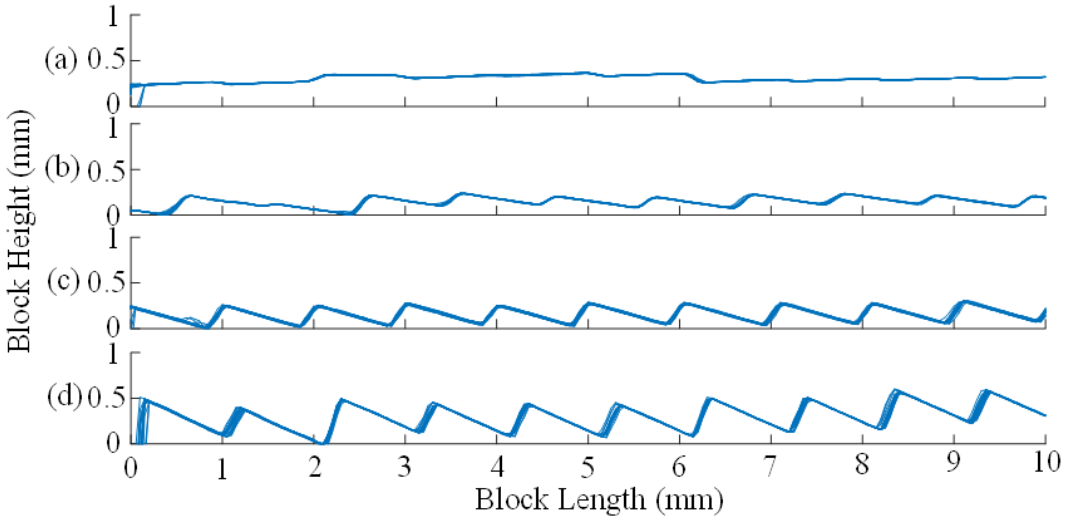

Figure 31. Profilometry data across the first 10 mm of the block on a 1:1 scale. Data taken at β = 90° for α values of a) 92.3° b) 82° c) 73.7° d) 64.9°

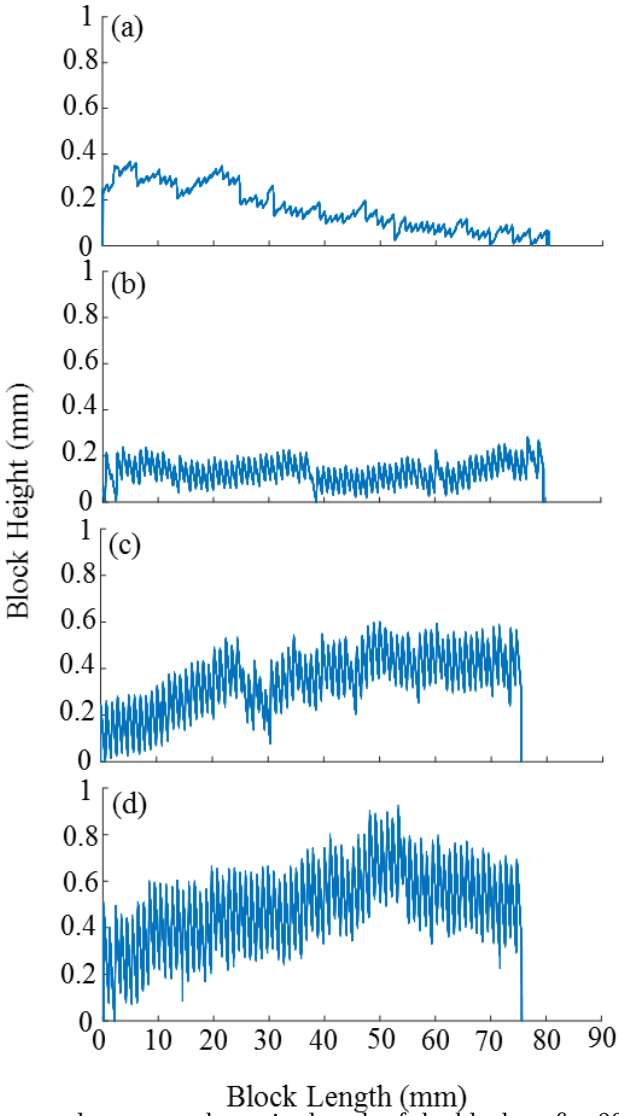

Figure 32. Profilometry data across the entire length of the block at β = 90° for α values of a) 92.3° b) 82° c) 73.7° d) 64.9°. Scale approximately 1:40.

The back surface slope seen in figure 31 (b)-(d) on the left side of the teeth, is an artefact due to the finite laser spot size of the profilometer. A sample profile data of ten teeth is taken and used to calculate values of α. The slope of the tooth is found from the second highest and second lowest value in any given slope, to avoid any errors from taking values past the point where the peak and trough of the slope occurs. These α values are averaged, and this average value taken to be the α value for this plate set. The standard deviation of this data set was used as an error in α. Values of α and associated errors are given in table 1. Also from this profilometry data an average standard deviation in h was calculated as 88 μm. Sample Individual tooth faces were examined for each plate set, and compared to the calculated slope for that set of plates. Standard deviations were taken as a measure of roughness and found to have an average value of 3.3μm. The samples used are displayed in figure 33.

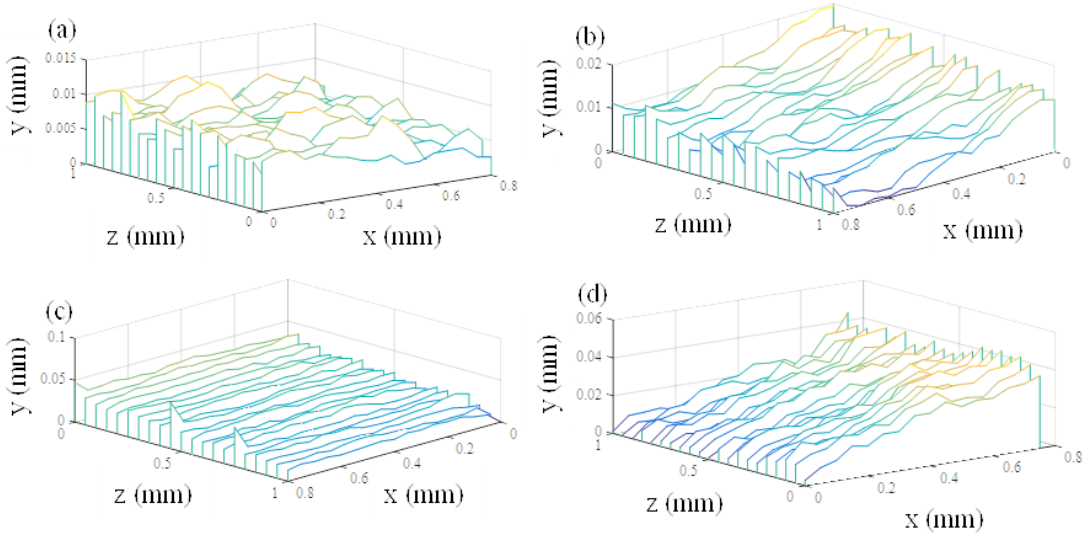

Figure 33. Profilometry data across a single tooth. Data reduced by expected slope (calculated from α) to help evaluate the roughness of the surface. Data taken at $\beta = 90°$ for α values of a) 92.3° b) 82° c) 73.7° d) 64.9°. x varies along the block, along the axis of propulsion, z is across the block, and y the height of the block.

The $\alpha = 92.3°$ plates were cut to be 90 degree plates (flat topped) and as such they were treated as flat topped throughout the experiment. This meant when it was discovered they were not flat and they had no direction of plate rotation associated with them it was unknown which direction the slight slope was pointing. Given this, and the slight nature of the slope, the $\alpha = 92.3°$ data was plotted twice as if it were symmetric about $\beta = 90°$.

3.3.3 Extraction of Data

For each experimental run, a video was taken. From these videos (coupled with observations noted in the experimental run), data on droplet reliability of propulsion, ratchet range of operation, droplet trajectories and, where appropriate, droplet velocity could be extracted.

For each droplet a description of its trajectory was assigned. These were split mostly into the position in which the droplet fell off the block, as shown in figure 34, however there are some exceptions to this grouping. Firstly a droplet that moves forwards initially but then changes direction and falls off the purple backwards section is grouped as “forwards then backwards”. A droplet that boils away on the block is grouped as “contact boiling”. A droplet that splits into more than one droplet is grouped as “split”. Finally, a droplet that moves to the propelled edge but stops or changes direction to backwards and then back to forwards is grouped as “Propelled (stop or change direction)”. These categories represent the entire range of behaviour observed. For the presentation of data these groups were often amalgamated to simplify them.

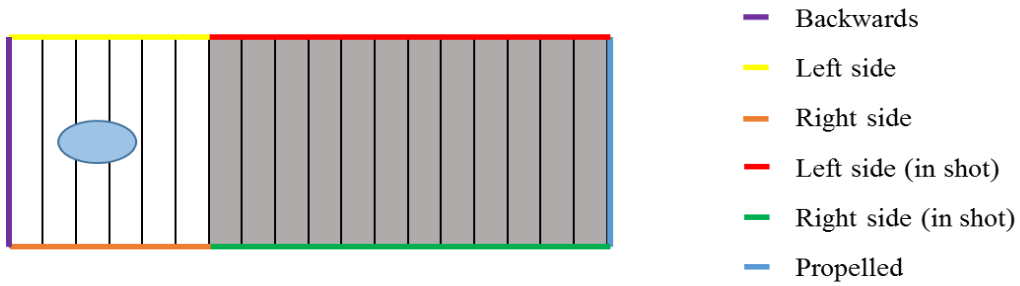

Figure 34. Droplet behaviour grouping diagram. Blue ellipse represents droplet starting zone. Grey background shows droplet detection area (also shown in figure 29).

To consider the reliability of droplets and the range of operation of a specific ratchet configuration the behaviour seen was simply split into two categories: those droplets propelled from the starting point to the starting position to the far edge of the block, and those that were not for any reason. This allows us to define a percentage of droplets that were propelled. This number will be representative of both the working range of a specific ratchet surfaces and the reliability of droplet propulsion within this range. The edges of the propulsion will give an idea of working range, with the rest of the data showing reliability of droplet propulsion.

For those droplets that are propelled, velocity data was taken. MATLAB was used to track droplet data by applying a binary mask to objects that are considered moving. This distinction is made by having a comparison between known background data and a current image. This process uses a Gaussian mixture model – a probabilistic population model based on Gaussian distributions. The position of the geometric centre point of tracked droplets in pixels was recorded against frame number. The initial and final positions of the droplet centre were disregarded to counter the effect of the edge of the tracking region. As the drop enters the region, for example, it appears to grow in size causing the centre of the droplet to move towards the middle of the tracking area and artificially speeding up the droplet. The opposite is true for a droplet leaving the tracking area. An example of the binary mask formed is shown

in figure 35. This code was adapted from example code from MATLAB [55]. A scale factor is applied to translate pixels to mm that follows the equation

$$Scale\ Factor = \left(\frac{Number\ of\ plates\ horizontally\ across\ shot}{Number\ of\ pixels\ horizontally\ across\ shot}\right) \times \frac{t}{\sin(\beta)}. \quad (9)$$

In cases where the number of plates across a shot could not be counted (due to lack of focus, for example) an alternative equation of the form

$$Scale\ Factor = \left(\frac{Width\ of\ plates\ (vertical\ dimension\ in\ the\ shot)}{Number\ of\ pixels\ vertically\ across\ shot}\right). \quad (10)$$

was used. All videos were taken at 60 fps, and this was used to convert frame numbers into time. From the *x* and *z* positions output by the tracking and scaling, a quantity, *s*, was taken equivalent to the distance travelled by the droplet from its initial tracked position, as shown in figure 36.

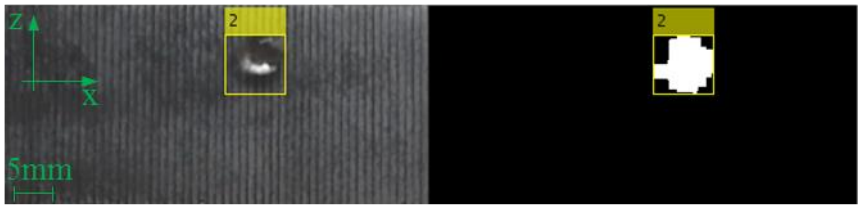

Figure 35. Droplet detection from video data in MATLAB.

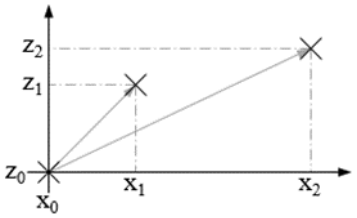

Figure 36. Distance travelled by the droplet, *s*, compared to *x* and *z* positions.

From work by Dodd et al. [53], the motion of a droplet being propelled by a ratchet is governed by a propulsive force from the vapour and an inertial resistance due to the droplet dipping in and out of the teeth and striking the tops of the teeth. This gives an equation of motion of

$$mv_d = \dot{F}_p - c_i v_d^2, \quad (11)$$

where v_d is droplet velocity, m is droplet mass, F_p is the propulsive force on the droplet and c_i is a coefficient representing inertial resistance acting on the droplet. For a droplet starting from rest, the solution to equation 11 at a time t is

$$v_d = v_t \tanh\left(\frac{t}{\tau}\right), \quad (12)$$

where terminal velocity is

$$v_t = \sqrt{\frac{F_p}{c_i}} \tag{13}$$

and relaxation time is given by

$$\tau = \frac{m}{\sqrt{c_i F_p}}. \tag{14}$$

From this, displacement, *s*, at a time *t* is found by integrating equation 12 with respect to time. This gives

$$s = v_t \tau \ln[\cosh\left(\frac{t}{\tau}\right)]. \tag{15}$$

The form of this equation suggests a droplet motion with a decelerating approach to a terminal velocity. At terminal velocity, displacement against time would have a linear form. For the droplets recorded in this experiment, a majority can be reasonably fit with a linear polynomial in displacement against time for the section of the droplet trajectory that is recorded, suggesting most had reached their maximum speed. 98.2% of the droplet trajectories had $R^2 > 0.9$ when fit with a straight line. An example of this is shown in figure 37. There were some sections of data where quadratic fits were better (generally for quicker droplets), indicating terminal velocity was not yet reached by the droplets.

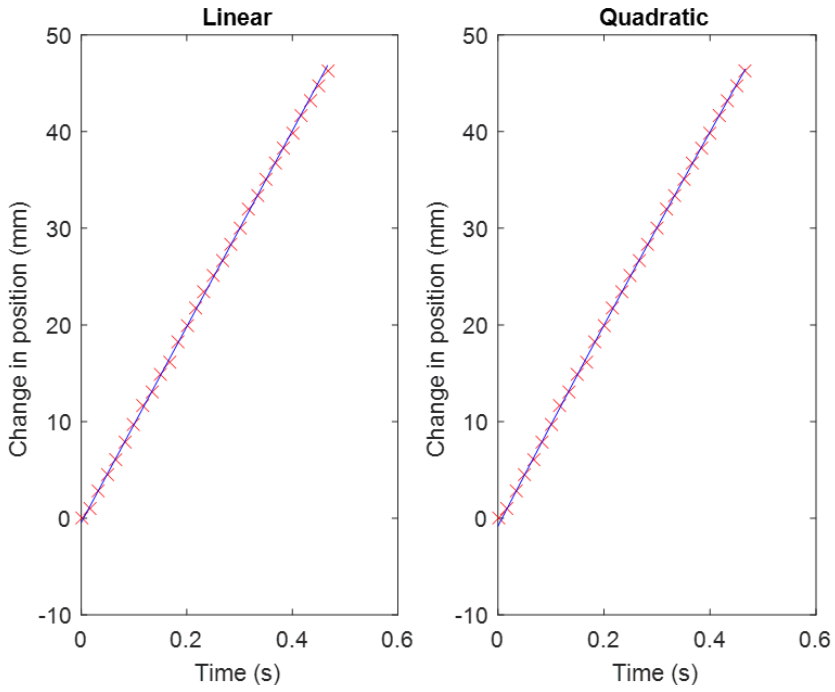

Figure 37. Droplet tracking data with a good linear fit.

These equations are valid for droplets with constant mass. Given the short length of the block and quick time for the droplet to cross the block, it is expected in most cases the mass loss due to evaporation is negligible. There may be some cases where the droplet is slow moving, or there are transition boiling events that rapidly evaporate some of the droplet that it is not the case that this mass loss is negligible. This could be another reason why some of the displacement time data collected fit better with a quadratic polynomial.

3.4 Results and Discussion

First, the reliability and range of operation data will be considered. Figure 38 shows data for the percentage of droplets propelled across the entire tested temperature range of 210-350°C. Here, percentage of droplets propelled increases most at low positive values of overhang angle for all tested block incline values. For the two non-zero incline values, this percentage of propelled droplets decreases again at higher overhang angle. More meaning can be extracted from this data by looking at the percentage of droplets propelled at different α and β values, across temperature bands of 20°C (giving approximately 14 droplets tested in each range). This data is displayed in figure 39. For the non-inclined block 100% reliability across the whole range can be seen within the overhang region, and the range with most droplet propulsion is 250-270°C. The region of propulsion shrinks at higher and lower temperatures. As incline angle increases, the droplet propulsion percentage decreases, shrinking the operational range of the blocks, and often decreasing reliability within these ranges, consistent with other work [33]. The overhang region contains most of the droplet propulsion at the two higher inclines tested. The practical outcome of this data is that overhangs improved the reliability and operational range of propulsion compared to geometries without overhangs.

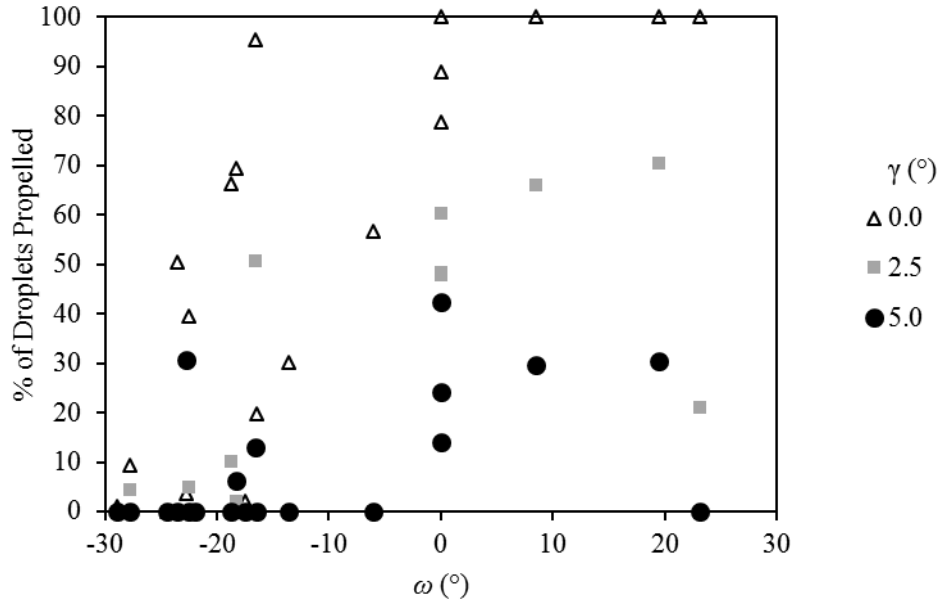

Figure 38. Percentage of droplets propelled over the entire tested range of 210-350°C across three block incline angles.

Note however, only slightly overhanging cases are tested here, and some more significant overhangs might lead to different behaviour.

In the next chapter, CFD data will be considered, and by comparison with this data will be used to understand this result.

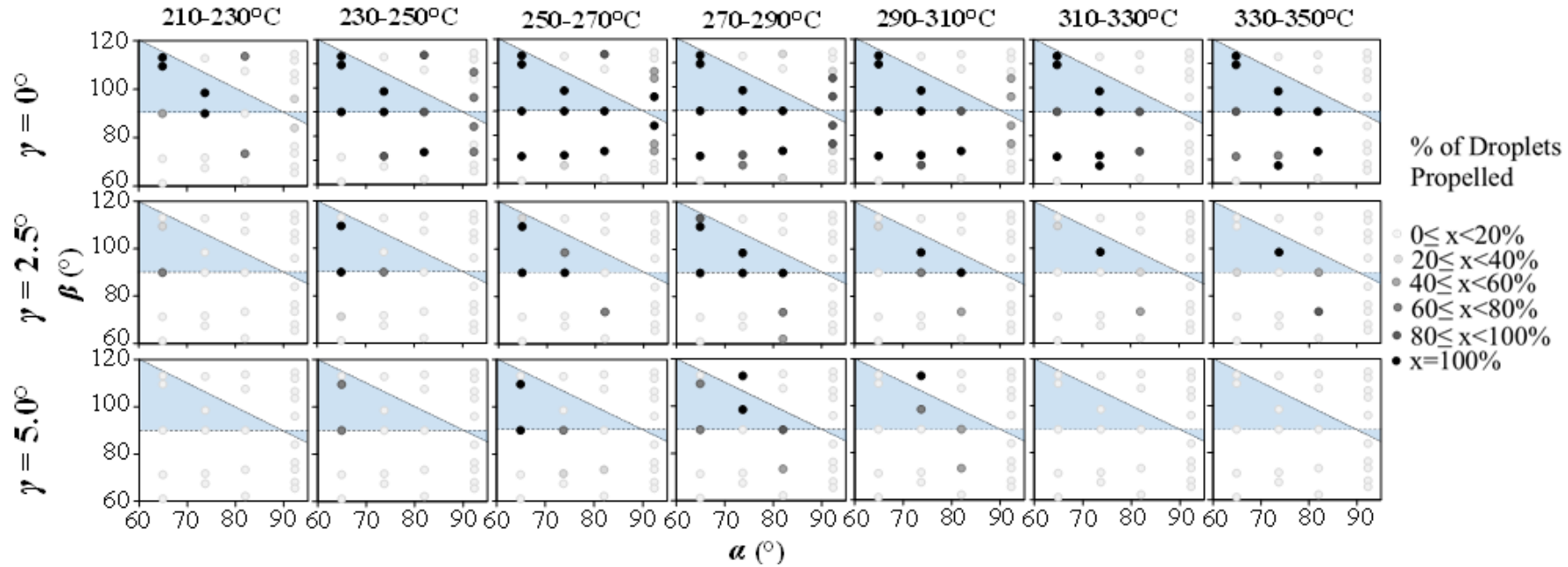

Figure 39. Percentage of droplets propelled for 20 °C temperature bands (columns) and inclinations γ (rows). Shaded boundary denotes areas with an overhang profile.

Secondly, velocity data is displayed in figure 40. For most tests, the velocity increases with temperature, peaks around 270 – 300 °C, and then decreases, which is consistent with other similar tests [40]. This pattern can be broadly explained in terms of four factors:

(a) Vapour layer thickness.
(b) Rate and direction of vapour flow.
(c) Droplet deformation.
(d) Wetting contact.

In the high temperature limit, deep in the Leidenfrost regime, the vapour layer beneath a droplet is complete and supports the droplet. With reducing temperature, the vapour layer thins leading to stronger interaction with the teeth [40, 41]. This can be expected to lead to stronger propulsion as the forwards flow of vapour between the teeth below a droplet is closer to its surface (enhancing drag) and more of the flow is in the forwards direction [34, 35]. However, droplets also deform further in the ratcheted surface at lower temperatures leading to dissipation of translational kinetic energy (TKE) [43]. In the low temperature limit, with a thin vapour layer, teeth may penetrate the droplet surface and wetting and transition boiling affect droplet dynamics. Any wetting contact and transition boiling events increase the spread of velocity data considerably, due to the random nature of the explosive boiling events they generate. This can enhance traction [33] but also leads to dissipation of TKE and complications preventing desired propulsion. All four of these factors are likely to impact the operational range and reliability of droplet propulsion as well. Vapour layers that are too thick or too thin will halt propulsion (a). Some tooth shapes will create flows that do not promote forward flow at all temperatures, theorised to be due to their deformation within the tooth [35] (b and c). Any wetting contact will likely decrease reliability due to the random nature of the contacts (d).

Looking in more detail at the data in figure 40, some specific points of interest can be picked out. References to specific data sets are displayed in the form (α, β). Small tooth heights with shallow front face angles mostly produce the highest velocities, particularly noting points (82.0, 90), (73.7, 90) and (64.9, 109.5). These speeds peak at ~350mm/s which is higher than previously reported for similar size ratchets [2, 3, 40] and droplets [41]. With these shallow ratchets, the ratio of forwards to reverse flow is expected to be highest, and energy dissipation from droplet deformation expected to be low.

An exception to this trend is (64.9, 113.1) which shows a peak velocity of ~200mm/s. This almost flat geometry reaches the Leidenfrost point at a lower temperature. It is proposed that as a result of the small space the teeth occupy, vapour layer quickly becomes thick enough to reduce the interaction between the droplet and the teeth.

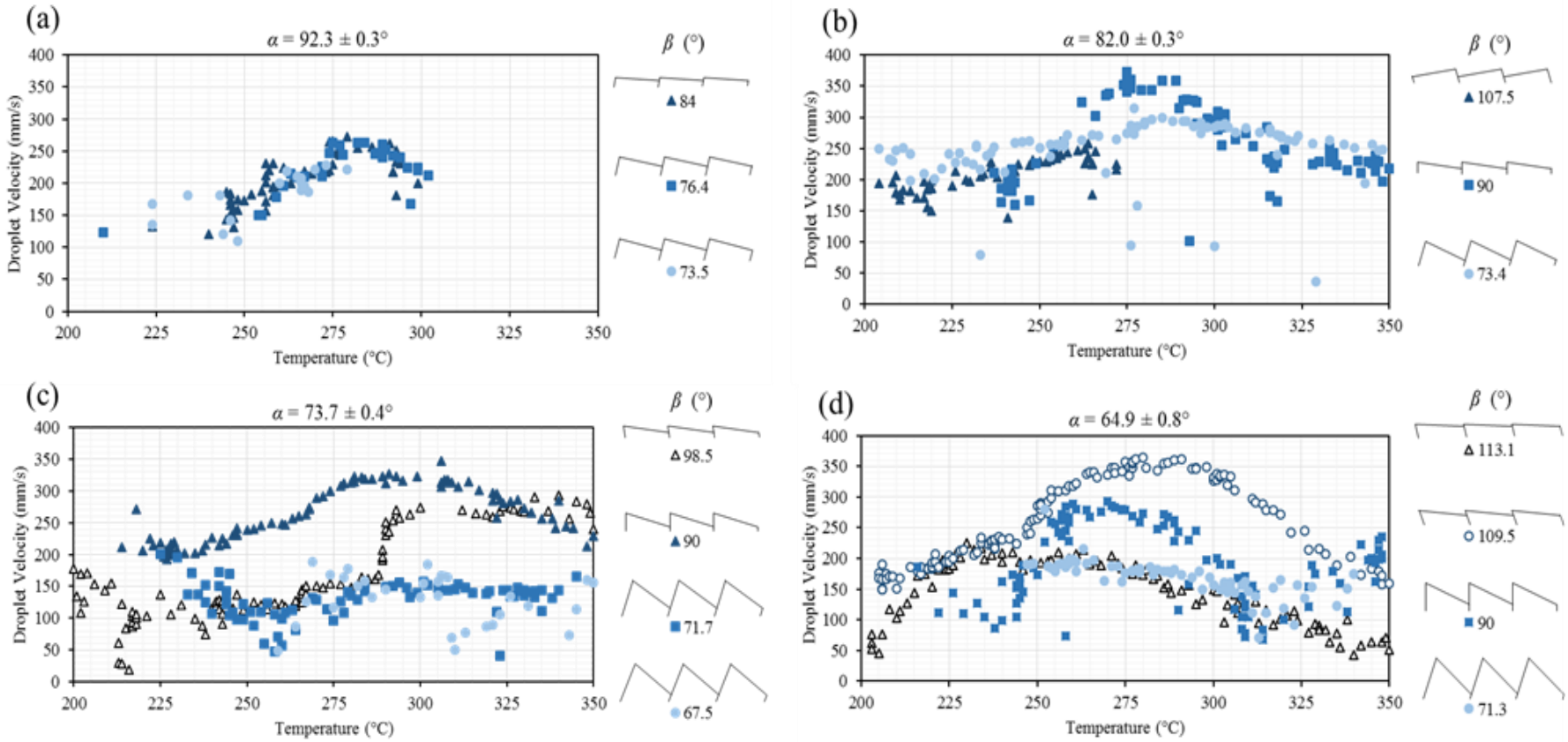

Figure 40. Velocity of propelled droplets for various ratchet profiles. (a) α = 92.3°, (b) α = 82.0°, (c) α = 73.7° and (d) α = 64.9°. Inclination, γ, is 0° for all plots. Open markers denote surfaces with ω > 0°, i.e. overhanging teeth.

Deeper teeth with steeper front face angles such as (82.0, 73.4), (73.7, 71.7) (73.7, 67.5), (64.9, 90) and (64.9, 71.3) produce lower velocities and have more velocity spread in the lower temperature range. The low temperature spread can be attributed to the effect of transition boiling, which will be more pronounced as the deeper teeth require thicker vapour layers to support droplets. With the steeper tooth angles less of the flow of vapour will be directed forwards, reducing droplet velocity.

Teeth with $\omega < 0$ (anti overhangs) generally have a smaller operating temperature range. This explains the small range of the $\alpha = 92.3°$ data, as all of these have anti overhang geometries.

Figure 41 shows stills from the high speed footage taken. Whilst there is clearly significant deformation of the underside of the droplet as it travels over the teeth, it does not appear to be consistent, and has many seemingly random fluctuations. This seems to be in contradiction with Jia et al. [35] basing the direction of droplet movement entirely on the deformation

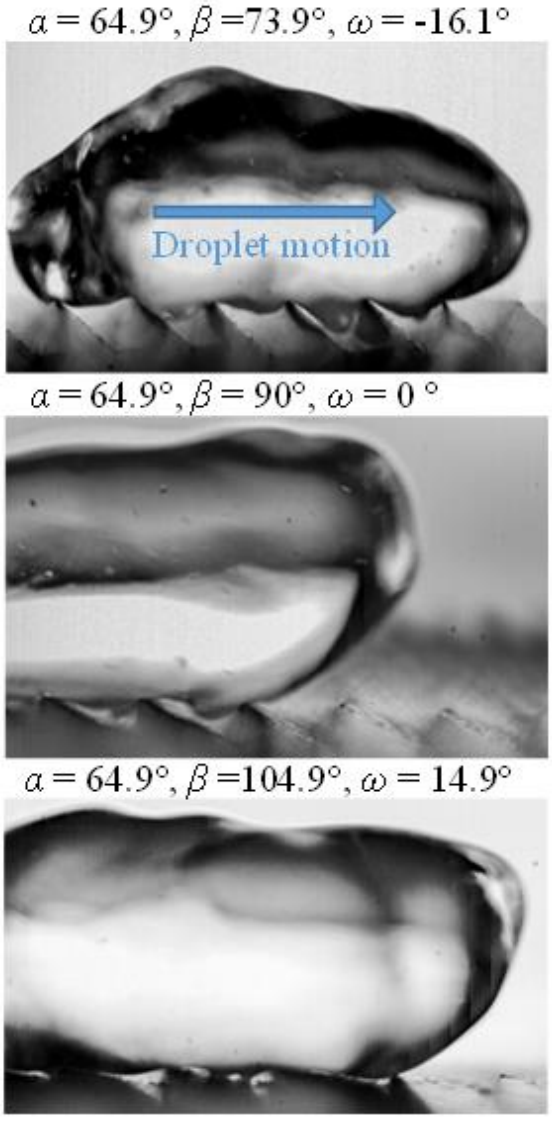

Figure 41. Stills from high speed camera footage of droplets traveling over different configurations of the variable block.

beneath the droplet. Whilst it is certainly a contributing factor, it appears to be much less predictable than suggested. The high-speed data also shows variation in the droplet shapes. Whilst they all stretch in the direction of propulsion, there are obvious rolling surface waves that deform the entire shape of the droplet as it moves. Behind the droplet tiny droplets can be seen being ejected from the droplet from contacts of the droplet with the ratchet surface.

Finally, the broader trajectory data will be considered. Across all tested ranges, clear bands of behaviour can be seen, and have been highlighted in an example Figure 42. Here droplet trajectories are split into droplets being propelled across the entire block, the droplet falling off the sides, the droplet falling off backwards and other events, mostly comprising contact boiling. Contours are added as a guide to the dominant behaviour, based on the points of data displayed. The bands change significantly with small changes to temperature and ratchet geometry.

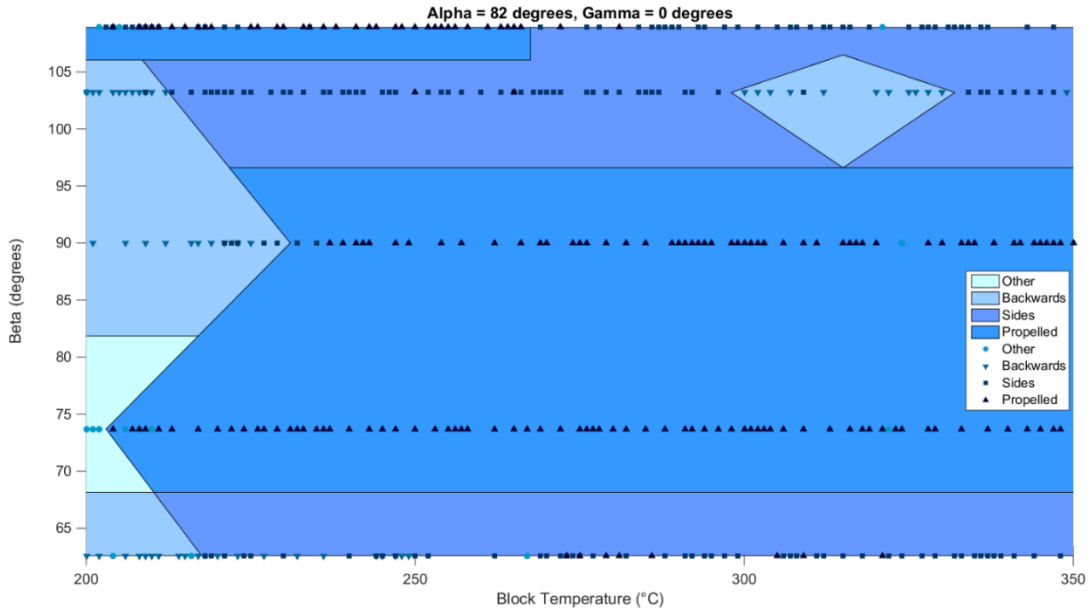

Figure 42. Data points plotted to describe trajectories of tested droplets. Coloured contours added to highlight bands of dominant behaviour.

3.5 Conclusions

The breadth of the data it is possible to take with this experimental setup has been demonstrated and explained in this chapter. The device and setup itself is as important as the results of experiments undertaken with it. The scope for further study with this device and modified versions of it is considerable, as explained in the future work section (5.2).

An important result of this work is overhang geometries improving reliability and operational range of propelled droplets. This is a useful result when trying to use Leidenfrost droplet

propulsion in an engineering application. There are also clear trends of shallower teeth leading to faster droplets and deeper teeth giving slower droplets with a greater chance of contact boiling events. Regions of high-speed droplet propulsion (~350 mm/s) have also been highlighted for millimetric teeth and droplets.

Comparing these results with CFD data of an analogous experiment, as will be done in the next chapter, will give more insight into the underlying mechanisms behind the distribution of droplet dynamics.

4. Computational Fluid Dynamics Simulations of a Dry Ice Puck Above a Ratchet

4.1 Introduction

In this chapter a model for the vapour flow between an infinitely long dry ice puck and a ratchet surface is presented. The motivation for this work was to create a model for comparison with the variable surface experimental data in chapter 3, and thus give a way to investigate the effect of surface profile on vapour flow computationally. Using a model of a dry ice puck gives a real-world comparison, whilst removing the complications of droplet dynamics (due to droplet deformation and internal flow). This work takes inspiration from the modelling performed by Cousins et al. [38].

Some of the parameter study work in this chapter has been published in the article reproduced in appendix 1 [54].

4.2 Simulation Description

4.2.1 Outline

A simulation is set up within ANSYS^{TM} as described by the schematic in figure 43. A puck that extends to periodic boundary conditions in the x direction, effectively making it infinite in this axis, is suspended above three ratchet teeth. The use of periodic boundaries both reduces solution time and removes any complicated behaviour at the edges of the puck. The ratcheted surface was deliberately constructed in a similar way to the variable surface made in the previous experiment and thus it is governed entirely by the variables described in section 3.2. To allow the comparison of the effect of as few variables as possible, when changing the β angle (the plate tilt angle), the plate width was also changed to maintain a constant tooth pitch and remove the effect of this variable. β is used to control the overhang angle, whilst changing α at the same time is used to ensure the front face angle of the tooth, φ remains the same. It is not possible to separate out the effect of single variables as they are intrinsically linked in the geometry of the ratchets.

The teeth were set as no slip wall boundaries. No slip walls make up the top and sides of the puck, with the boundary on the bottom face of the puck producing CO_2, to generate the vapour flow. The normal speed of the mass flow was controlled as a variable v_m. The distance from the top of the tooth to the puck, d, is controlled to supplement this, as in reality, the flow rate and height of puck balance to some equilibrium for a specific temperature. Initially, the fluid body is entirely air at 25°C and 1 atm. The CO_2 introduced is modelled as an ideal gas. Having more than one gas adds an extra mass fraction element to the solution conditions. This extra solution element makes the problem take longer to solve. The external openings at the edge of the fluid body allow air to enter the body, and both gases leave. The height and width to the

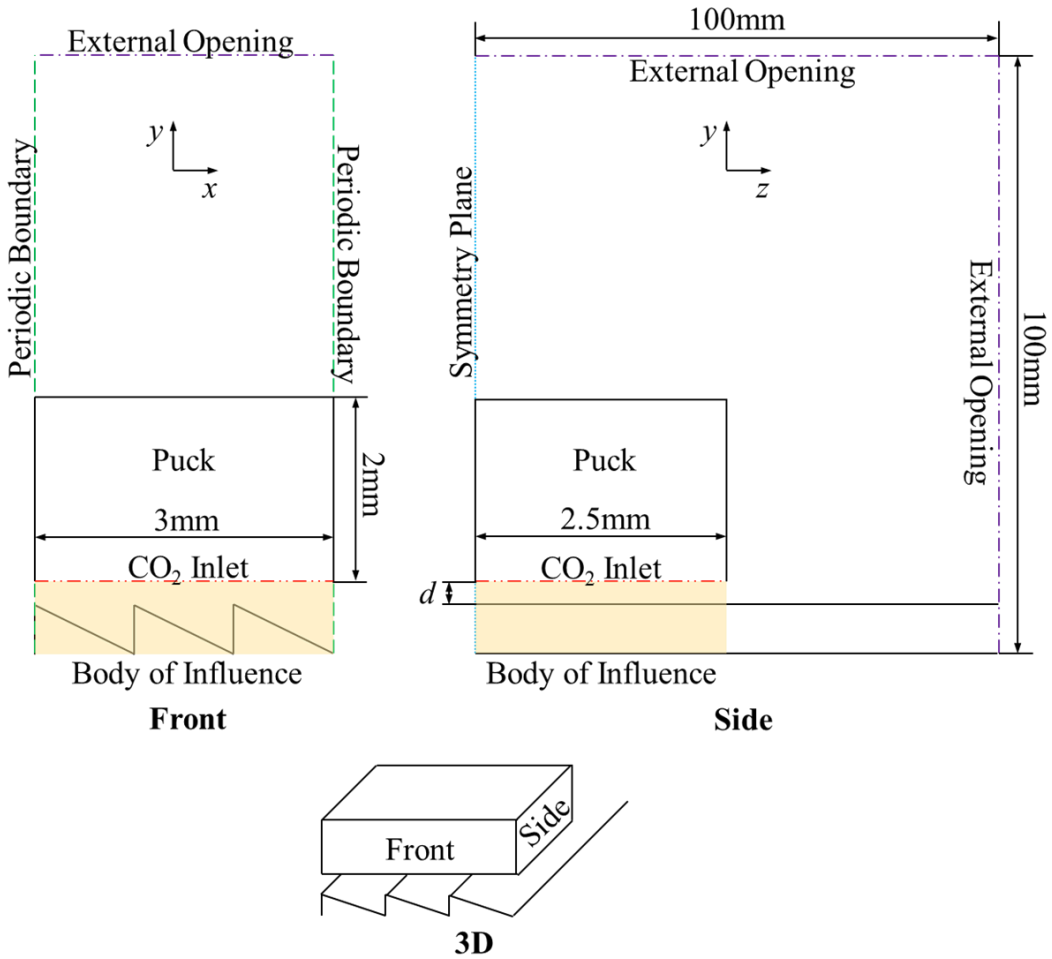

Figure 43. Diagram of the simulations of an infinite CO_2 puck. Not to scale.

opening boundaries were both set to 100mm after a sizing study showed little impact of this size on the overall solution error. These external boundaries are set to maintain atmospheric pressure. A symmetry plane (shown in figure 43) confines the system as if it were reflected across this plane – preventing any flow in or out of the plane, but allowing flow across it.

The problem was modelled in steady state. Turbulence is modelled through the Shear Stress Transport (SST) model. Heat transfer is not considered in this model, the system is set to be isothermal at 25°C. Buoyancy is considered with –g acceleration in the *y* direction. Given that the problem is isothermal and that buoyancy effects are purely due to density difference, this effect is likely to be negligible, with the only density difference being due to the two different gases in the problem. The advection scheme is high resolution. The high-resolution scheme is a total variation diminishing scheme which is accurate to at least second order. The turbulence numerics are accurate to first order. A conservative automatic timescale was set. The timescale represents the time steps due to the pseudo-transient method ANSYS uses to solve problems. The automatic timescale picks a time step that is likely to solve but not in the most time efficient way.

The flow of gas beneath the puck is visualised in component form, with *u*, *v* and *w* being velocities in the *x*, *y* and *z* directions respectively.

4.2.2 Meshing and Convergence Criteria

The mesh is set up with mesh matching at the periodic boundaries, inflation layers on the bottom of the puck and on the teeth beneath the puck and a rectangular body of influence used to control sizing in this area beneath the puck and across the teeth. Mesh matching ensures the mesh at both ends of the periodic boundary precisely match up, to remove any errors from flow moving through this boundary with a mismatched mesh.

A mesh study was conducted to ensure appropriate mesh fidelity and establish errors associated with the mesh applied to the problem. The force in the *x* direction, F_x, applied by the vapour flow across all faces of the puck was used to study the effect of mesh variables, as this was expected to be the output that is most important to simulate accurately, as it relates directly to the movement in the propulsion direction of the puck. Within this study the bulk mesh sizing, the maximum number of inflation layers and the body of influence sizing were varied. The enclosure height and width were also considered. Whilst not strictly a mesh variable, RMS residual target was studied, which gives a measure of the average size of the residual and thus an approximate error of the solution. Finally a general scatter, i.e. variation in the solution value due to moving the mesh points whilst keeping all other settings the same, was tested by nudging the teeth forwards or backwards across the scale of one tooth pitch in the *x* direction, as this should not affect force applied to the puck because it is infinite in this direction. There is an interdependence with all the variables tested. Testing the effect of each variable on the final solution value is accomplished by varying one variable whilst keeping all others fixed. This process was repeated several times to determine how much each variable affected the final solution value. Final variable values were settled on by primarily focusing on reducing the error in F_x, and secondarily reducing simulation time and maintaining stable solutions across a wide selection of test cases. The data shown in this subsection therefore shows variation of F_x due to a single variable, with all other variables set to their final values. For this study the ratchet tooth overhang case of (64.9, 109.5) was used as it was a point from experimental data from the chapter 3 that was both fairly typical in its geometry and a harder case to mesh due to its overhang profile. A mass flow normal velocity value of 0.15 m/s was used as it was estimated to be in the typical range of tests to be performed with this simulation.

The three factors, shown in figure 44, that had most effect on the F_x in the range tested were the residual target, max number of inflation layers and mesh sizing in the body of influence. Figure 45 shows the effect on F_x for the other variables tested. Dependence of F_x on number of teeth was also tested and found to be linear.

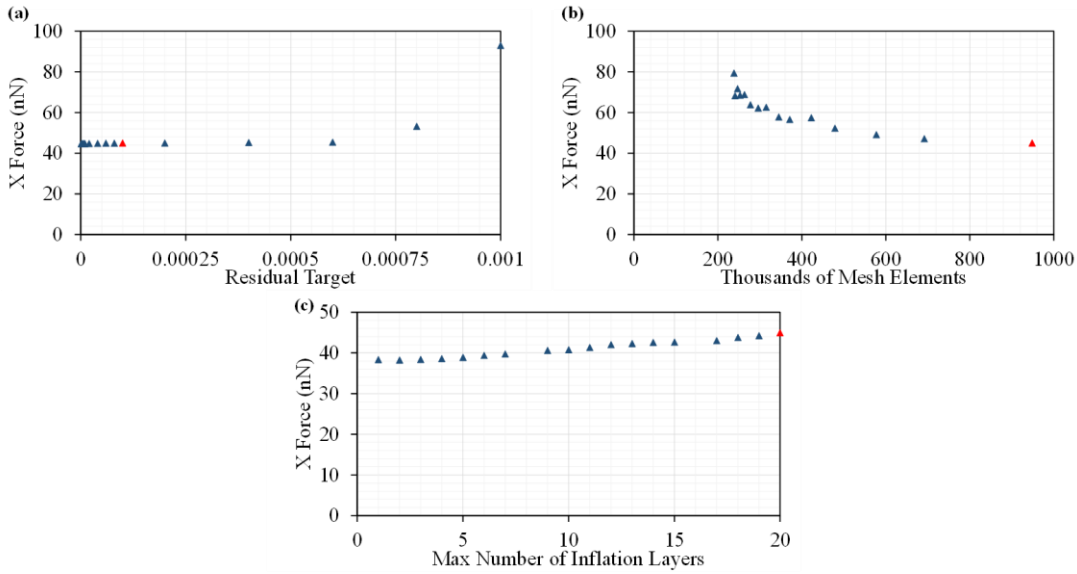

Figure 44. Convergence plots from mesh study for (a) RMS residual target, (b) body of influence sizing and (c) maximum number of inflation layers. Red points show chosen values for simulation.

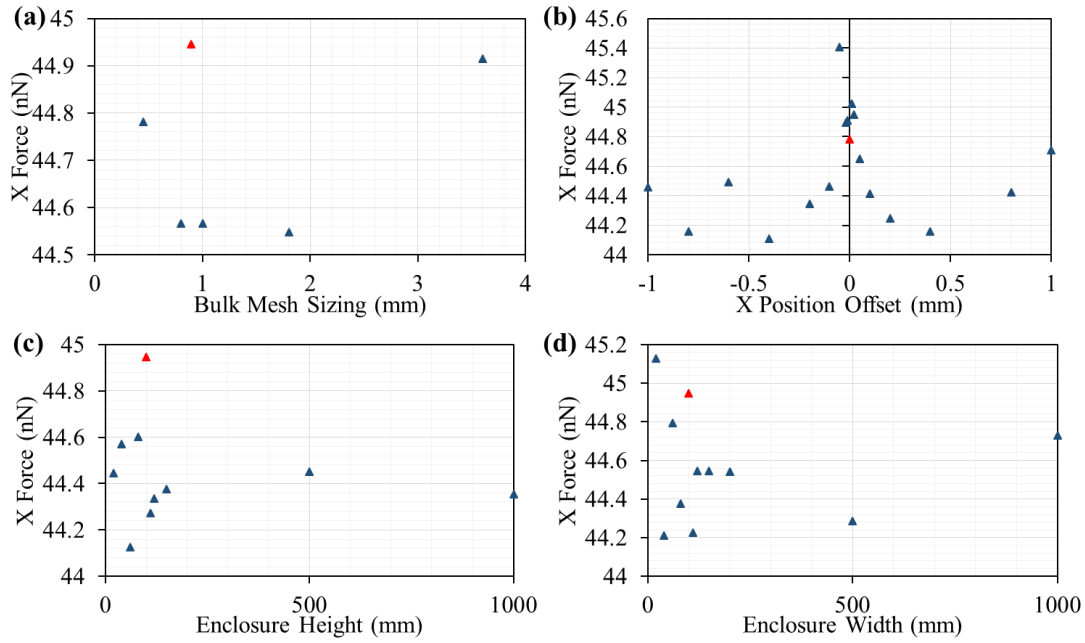

Figure 45. Convergence plots from mesh study for (a) bulk mesh sizing, (b) scatter, (c) enclosure height and (d) enclosure width. Red points show chosen values for simulation.

For the variables displayed in figure 44, a function is fitted with a horizontal asymptote (representing the estimated true value), and the difference between that asymptote and the simulated value used as an error. For inflation layers and the body of influence sizing, mesh elements against the logarithm of force was fitted as N^{-1} (where N is mesh elements). Logarithm of force is used here to improve the curve fit performed. From figure 44 (c) and the size of the error for inflation layers, it is clear this is not as well converged as the other variables. However, above 20 inflation layers the problem would not reliably solve. For the

RMS residual target, the asymptote was fitted from the value with the lowest residual target simulated, and the error taken from the difference to this value as before. For the variables displayed in figure 45, the error was taken as three times the standard deviation of the data set. Note that the variables in figure 45 varied on scales magnitudes lower than those in figure 44 and thus the final values chosen were based on running speed of the solution and ease of convergence. The final chosen values for each variable is presented along with their associated errors in table 2. The total error in the F_x is combined from these components to be approximately 11 nN, and in F_y 4000 nN. Converting to a shear stress (described in the next subsection) in x, the error becomes approximately 700 μPa.

Variable	Value	Associated Error in F_x (nN)
Bulk Mesh Sizing	0.9 mm	0.6
Body of Influence Sizing	0.03 mm	5.2
Maximum Number of Inflation Layers	20	8.8
Enclosure Height	100 mm	0.7
Enclosure Width	100 mm	0.9
RMS Residual Target	10^{-4}	0.2
Scatter	N/A	1.1

Table 2. Final values for meshing and boundary parameters with their error contribution to F_x given to 0.1nN.

Figure 46 shows the mesh from the symmetry plane. The effect of the body of influence decreasing mesh element size and the created inflation layers can be seen along the teeth and the bottom of the puck.

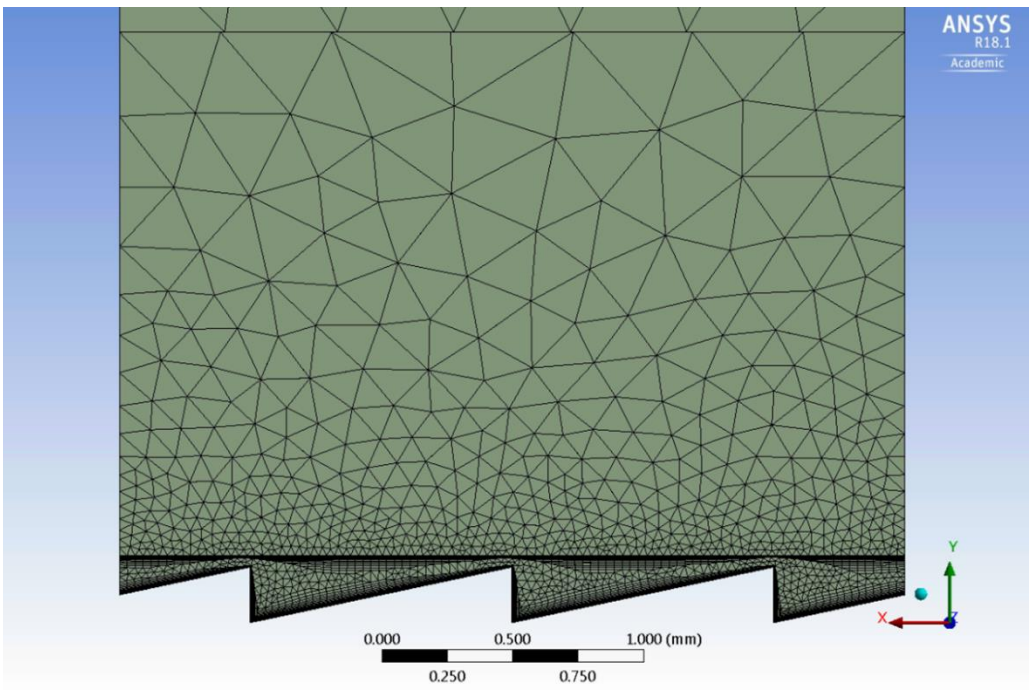

Figure 46. Example of mesh viewed from the symmetry plane. α = 78°, β = 90°, d = 43.4μm.

4.2.3 Shear Stress Sampling

It is often more useful to discuss the impact of the vapour flow on the puck in terms of shear stress in the *x* direction rather than force applied, as this removes the specific size of the puck as a factor when comparing values. For the total shear stress applied, $\langle \tau_x \rangle_{total}$, (where $\langle\ \rangle$ is the arithmetic mean) the force acting on the underside of the puck (which makes up almost the entire force acting on the puck) is divided through by the area of the bottom puck face. As well as this, two sampling integrals are defined $\langle \tau_x(x) \rangle_z$ and $\langle \tau_x(z) \rangle_x$. The average shear stress, $\langle \tau_i(j) \rangle_k$, is the shear stress in the direction *i* averaged over *k* for each location *j*. These are calculated from line integrals of d*u*/d*y* taken in lines along the *z* direction at different *x* positions on the underside of the puck (e.g. vertical blue line figure 47), for $\langle \tau_x(x) \rangle_z$, and in lines along the *x* direction at different *z* positions on the underside of the puck (e.g. horizontal red line figure 47), for $\langle \tau_x(z) \rangle_x$. The average of these line integrals were multiplied by the negative of the dynamic viscosity of CO_2 (to account for the coordinate system used).

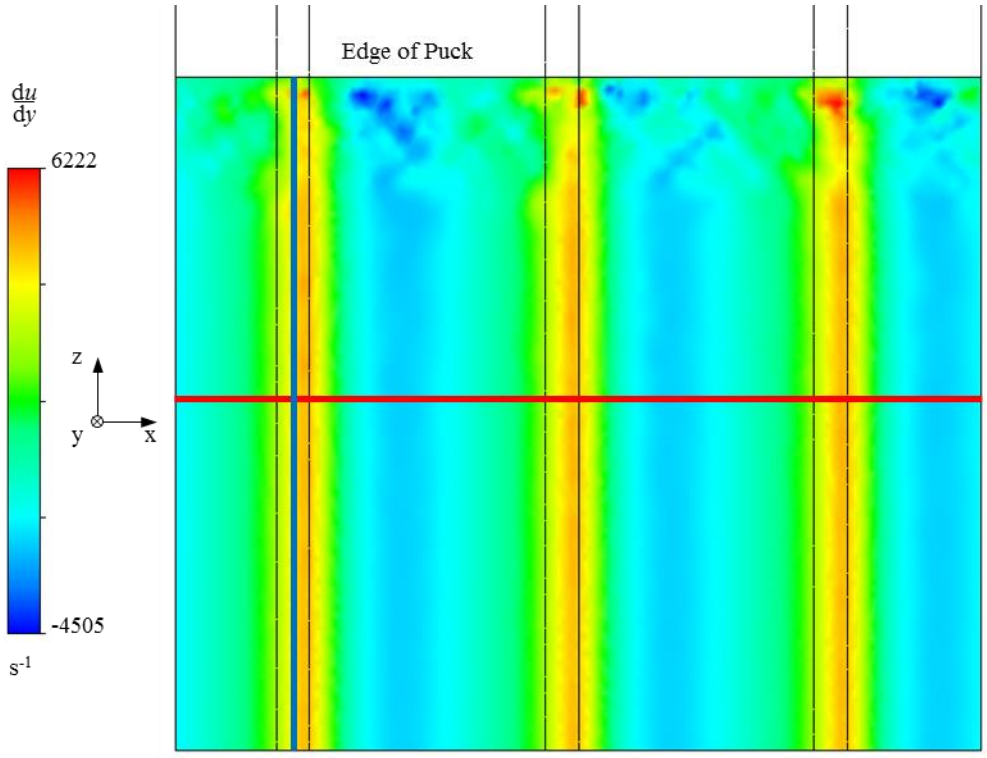

Figure 47. d*u*/d*y* at the underside of the dry ice puck for an example case. Blue and red lines are integral sampling lines. Blue is $\langle \tau_x(x) \rangle_z$ and red is $\langle \tau_x(z) \rangle_x$.

4.2.4 Equilibrium and Validity

To understand whether a dry ice puck is levitating within the simulation in a realistic manner three factors need to be considered: the height of the puck from the top of the teeth, *d*, the

mass flow normal velocity, v_m, and the tooth shape. Each combination of these gives a value for *y* force (F_y) acting on the puck.

For droplets, the vapour layer height has been seen to be on the order of 10-100μm [7]. This gives a sensible starting point for our ranges of height from the top of the teeth. This range is further limited by lack of convergence for simulations with heights below 35μm. An appropriate value for v_m can be estimated using an equation from Baier et al. [4],

$$v_m = \frac{\lambda \Delta T}{\Lambda \rho_{CO2} \Delta H_{subl}}, \tag{16}$$

where λ is the thermal conductivity of the vapour, ΔT is the temperature difference across the gap, Λ is some length scale of the order of the gap width between ratchet and ice, ρ_{CO2} is the density of CO_2 and ΔH_{subl} is the latent heat of sublimation. Using the distance d as the length scale, at a temperature of 300°C, for d = 35μm, v_m = 0.44 m/s and for d = 100μm, v_m = 0.15 m/s. By comparing the mass of dry ice in the puck with the mass flow of CO_2 an estimate for puck lifetime can be made. This gives a lifetime of

$$t = \frac{\rho_{dry} h_{puck}}{\rho_{CO2} v_m}, \tag{17}$$

where h_{puck} is the height of the puck (2mm) and ρ_{dry} is the density of dry ice. This gives t = 5.9s for d = 35μm and t = 17.3s for d = 100μm both of which are, given the simplicity of the model, of the right order for a puck of this size at this temperature.

To evaluate a dry ice puck at equilibrium, F_y acting on the puck must balance its weight, which for the 5x2x3mm puck that has been simulated here is calculated as 459μN. To find the height a puck would sit at, given a specific tooth geometry and v_m, a range of heights are simulated between d = 0.035-0.1mm. The output of F_x and F_y are fitted against these heights with power laws. At each mass flow/geometry combination this allows an equilibrium height, d_{eq}, to be calculated from the F_y power law and an equilibrium F_x, F_{eqx}, to be calculated from this d_{eq}.

To compare with experimental droplet data from figure 40, mass flow rates need to be linked to temperature. Given the broad range of heights and mass flows, and thus temperatures, this simulated data spans, the simple conduction relationship given by equation 16 is not sufficiently accurate. Equation 16 is therefore adapted with a radiative heat term, as radiative heat is expected to become significant at higher temperatures. This gives ratchet temperature, T, the form

$$v_m \rho_{CO2} \Delta H_{subl} + \frac{\lambda}{\Lambda} T_{subl} + \sigma \varepsilon_{dry} T_{subl}^4 = \frac{\lambda}{\Lambda} T + \sigma \varepsilon_{ratchet} T^4, \tag{18}$$

where T_{subl} is the sublimation temperature of dry ice, σ is the Stefan-Boltzmann constant, ε_{dry} is the emissivity of dry ice (set at 0.9 which is appropriate for H_2O ice and snow) and $\varepsilon_{ratchet}$ is

the emissivity of the ratchet surface (set at 0.07, appropriate for polished steel). In this case, to account for the geometry of the teeth, Λ is set to an average height from the tooth to the puck, calculated by integrating this distance across a pitch of the tooth, and dividing through by the pitch, P. Note that, for overhang geometries, the highest point of the tooth is considered. This gives

$$\Lambda = d + \frac{x_2^2}{2P}\tan(\beta) - \frac{x_1^2}{2P}(\tan(\alpha+\beta) + \tan(\beta)), \tag{19}$$

$$\text{where } x_1 = \frac{P\sin(\beta)\sin(\alpha+\beta)}{-\sin(\alpha)\tan(\alpha+\beta)}$$

$$\text{and } x_2 = P - x_1.$$

For $\beta \geq 90°$ this simplifies to

$$\Lambda = d - \frac{P}{2}(\tan(\alpha+\beta)). \tag{13}$$

These equations can be solved, and the single real positive root used as an estimate for the temperature in Kelvin at that geometry/mass flow pairing. Clearly, this estimate breaks down near to and below the sublimation temperature of dry ice as the dry ice would no longer be held at sublimation temperature at this point (assuming the ratchet is the sole source of heat in the system).

The model will break down at very low d_{eq} as instabilities in the flow will allow contact with the tooth surface and cause rapid sublimation. For comparison with experimental droplet data, the displayed equilibrium heights have been limited to between 10-100μm as this is a reasonable film height for droplets [7], as well as containing the range which heights were modelled in this set of simulations (35-100μm). For temperature the range displayed was from -100 to 500°C, i.e. from just below the sublimation temperature of dry ice to the maximum temperature a simple ratchet on a hotplate could be heated to with the equipment available.

4.3 Results and Discussion

4.3.1 Parameter Study

A parameter study was performed across a range of seven values of d (35-100μm), ten values of v_m (0.1-1.0 m/s) and thirty three tooth shapes (φ = 60-89°, β = 60-120°). The main output of interest in this case is the force in the x direction acting on the puck, as this would represent a propulsive force applied to it. Contour plots can be formed from this data. Gaps in the data, created by variable combinations where a solution would not converge, were filled by interpolating with a cubic spline across the missing points. The contours were bounded to zero

F_x at v_m = 0 m/s and at a front face angle, φ = 90° (a flat block). An example of the evolution of F_x with d can be seen by comparing figures 48-50.

Comparing figure 48 and 50, there is a difference in maximum force of two orders of magnitude owing to the difference in height from the tooth. Both data sets contain an obvious rise in force around the area of 85-90° front face angle, at the higher end of mass flow rate from 0.5-1 m/s. Given the range of mass flow rates this feature occurs at, compared with previous estimates of mass flow rates and puck lifetimes, it is not going to be a feature of a standard dry ice puck with a reasonable lifetime. There is a considerable difference across the data sets in the lower mass flow range, where a dry ice puck might be expected to exist. In figure 50 a secondary local peak in force can be seen between 0.1-0.2 m/s and 70-80°. Qualitatively, these contour plots remain much the same for changing β angles. To further

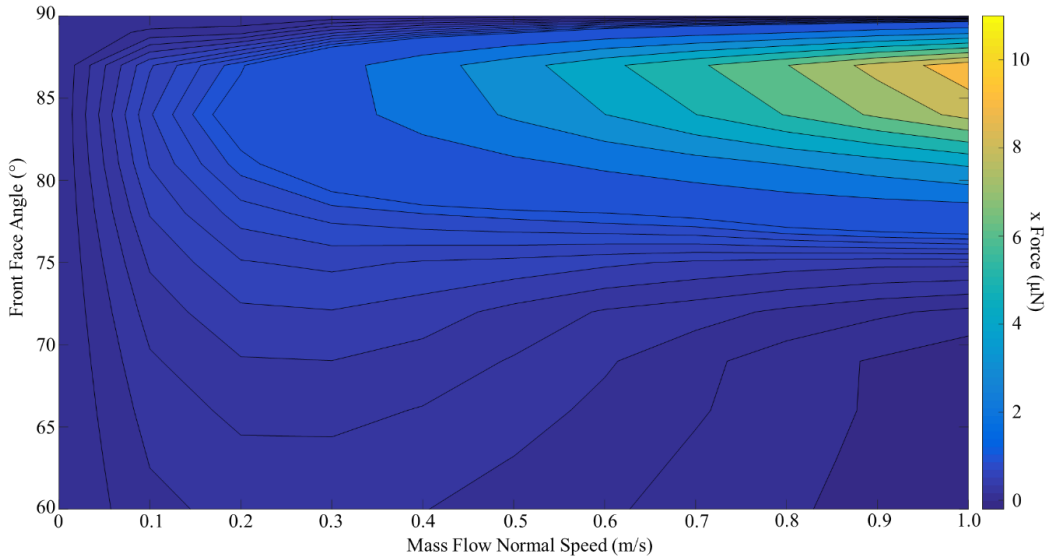

Figure 48. Simulation data for force acting on a dry ice puck in the x direction. d = 35μm, β = 90°.

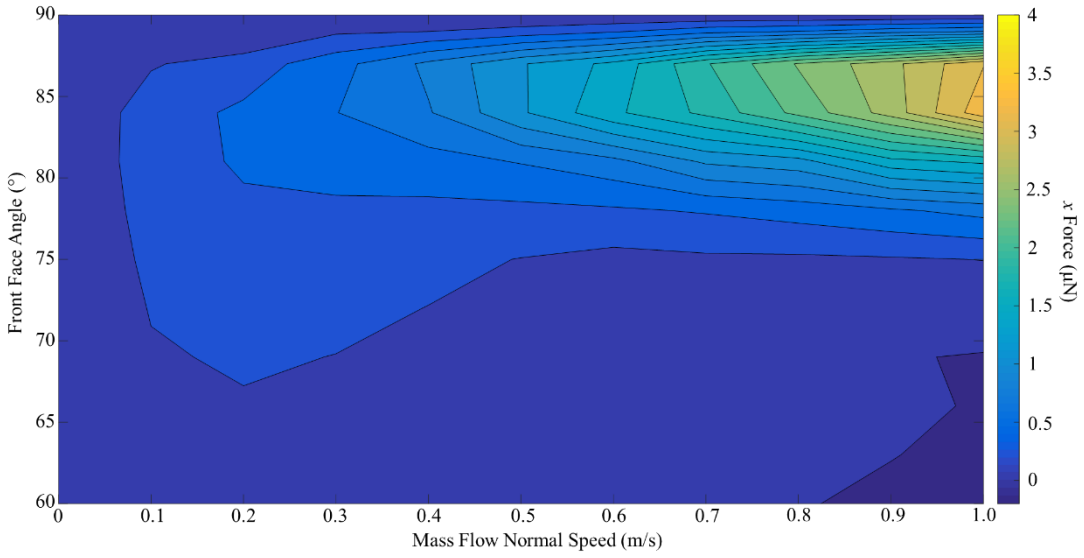

Figure 49. Simulation data for force acting on a dry ice puck in the x direction. d = 50μm, β = 90°.

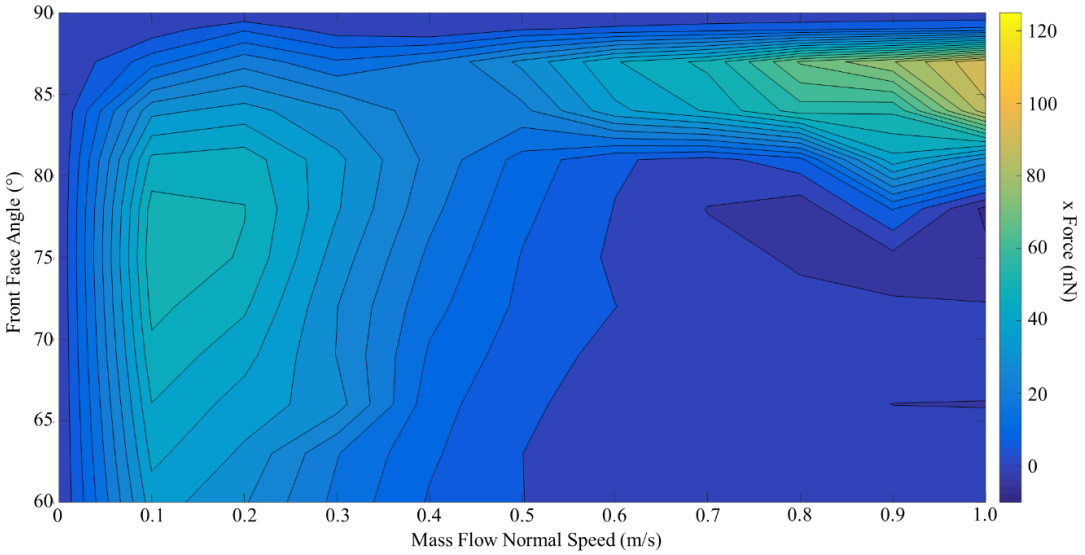

Figure 50. Simulation data for force acting on a dry ice puck in the x direction. d = 100μm, β = 90°.

understand the features described, and how height and beta angle affect them, F_x data at constant front face angle is evaluated.

From plots of F_x against v_m, shown in figure 51, for the majority of cases with low flow rate a slight increase in force can be seen with increasing overhang angle. Unexpectedly, in the high

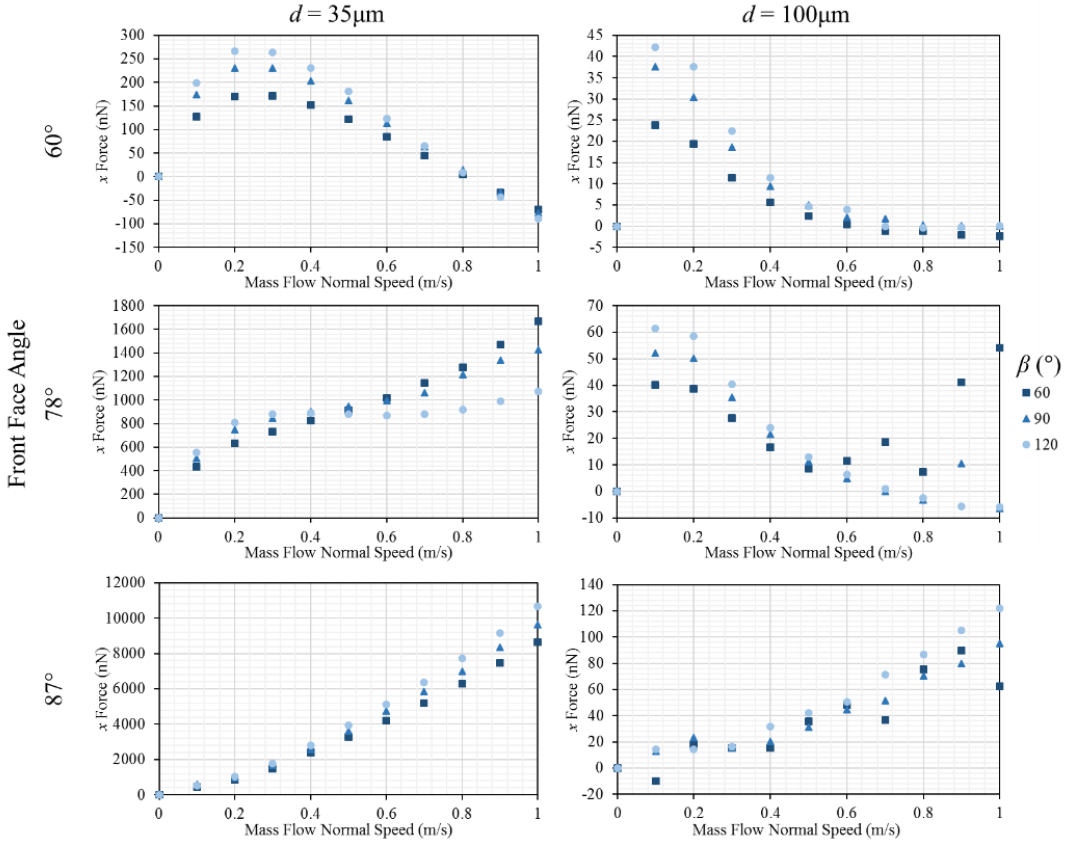

Figure 51. F_x data for lines of constant front face angle for different distances from tooth peak to puck underside and values of β.

flow rate φ = 78° case, an area of behaviour is revealed where there is an increase in F_x with an anti-overhang profile. Also, looking at the φ = 78° case, d = 100μm and both of the φ = 60° cases the peak previously seen at low mass flow (between 0-0.3 m/s) in the contour plots is obvious. This peak in force decreases in its prominence compared to the force values at higher mass flow with decreasing d and β and increasing φ, all of which decrease the volume beneath the puck and within the teeth – suggesting a link between this volume and this peak. Contrary to this, the increase then decrease of force of the peak with φ seen in the d = 100μm case suggests this is not the only important factor and that the angle of the tooth must also have an impact. To further evaluate this data set a more detailed examination of individual cases will be performed.

First the typical low mass flow case of φ = 60°, d = 35μm, v_m = 0.2 m/s will be examined. Considering figure 52, a reasonably uniform shear contribution can be seen across the z positions of the block, with a change near the edge of the block. The flow near the edge of the block will change as it transitions to a position where it is not bounded by the solid puck. In this example there is a clear difference in shear between all three β in the bulk flow, but this difference contracts at the edge of the puck. In this regime, increasing overhang (ω, the overhang angle) increases forward force on the puck.

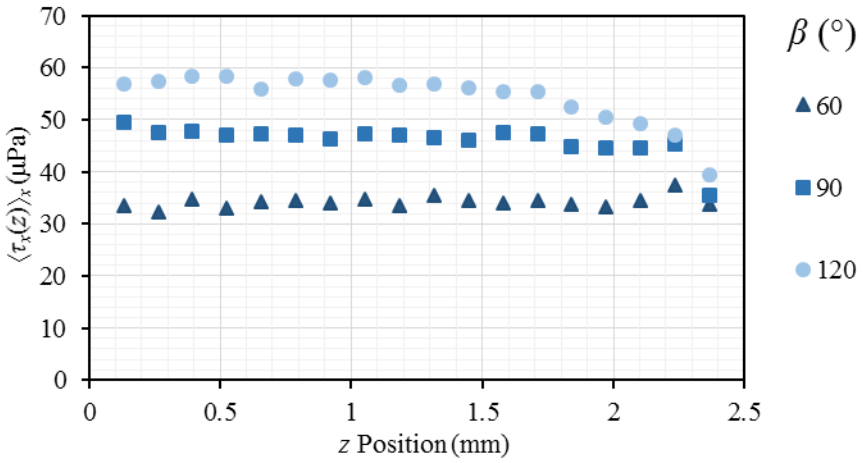

Figure 52. Shear stress on the underside of the puck in the x direction, $\langle \tau_x(z) \rangle_x$ for φ = 60°, d = 35μm, v_m = 0.2 m/s. Displayed for three β values. The centre symmetry plane of the puck is at 0 mm and the edge at 2.5 mm.

Figure 53 shows the x velocity profiles midway between the centre and edge of the puck for the cases displayed in figure 52. Increasing in overhang angle increases the maximum and minimum u value. As well as this, the distribution of forwards and backwards flow shifts towards having a larger area of forwards flow and a smaller area of backwards flow directly beneath the puck. Both of these factors will increase the overall forwards viscous driving force

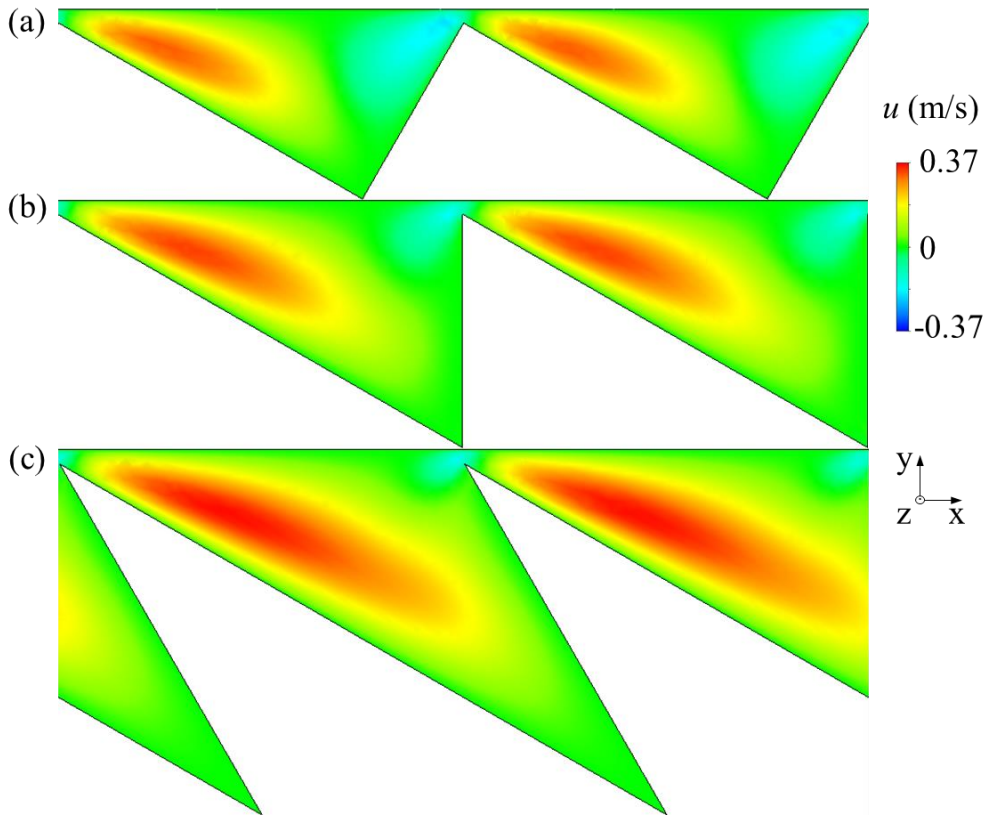

Figure 53. Velocity in the *x* direction on a plane 1.25 mm from the centre of the puck at φ = 60°, d = 35µm, v_m = 0.2 m/s. (a) β = 60°, (b) β = 90° and (c) β = 120°.

in the *x* direction acting upon the puck, and account for the increase in shear stress with β angle seen in figure 52.

The profile seen in figure 53 (b) for the vertical backed problem is very similar to the profile seen in work by Baier et al. [4] and the profile away from the edges of the puck modelled by Cousins et al. [38] discussed in subsection 2.4.2 and shown in figures 15 and 16. For completeness, figure 54 shows the *y* and *z* velocity profiles for the same case as in figure 53 (b). Here, it can be seen that the outflow (*w*) dominates the interaction in magnitude – a fact

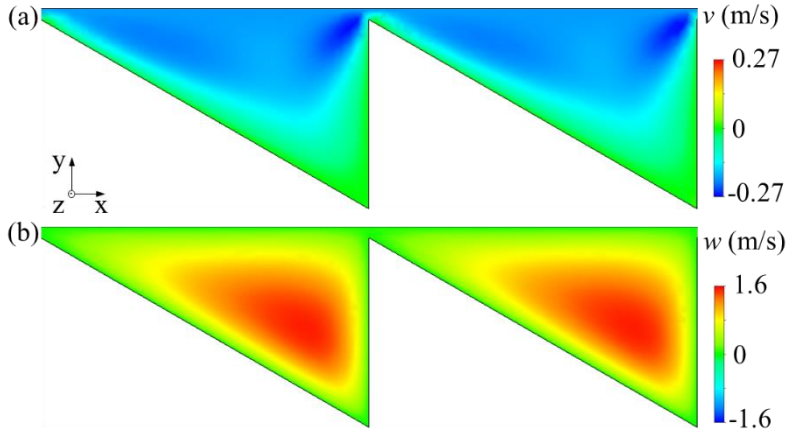

Figure 54. Velocity in the (a) *y* direction and (b) *z* direction on a plane 1.25 mm from the centre of the puck at φ = 60°, d = 35µm, v_m = 0.2 m/s, β = 90°.

which is important when considering the impacts of overhangs and their reliability, as an overhang separates a portion of the base of an ice puck from the main outflow source. This lateral flow can impact reliability in the case of the previous experimental work by causing a droplet to move sideways instead of forwards. Comparing to the same work as before (figures 15 and 16), the profiles again seem similar in shape.

The previous case of φ = 60°, d = 35µm, v_m = 0.2 m/s can be compared with the high mass flow deep tooth case of φ = 60°, d = 35µm, v_m = 1 m/s. Figure 55 shows the $\langle \tau_x(z) \rangle_x$ values and x velocity profile for the vertical backed case. The shear in the high mass flow case has a large spike near the edge of the block, and much more fluctuation in the values in the bulk flow. It is hard to tell where the force separation due to the different overhangs arises in this case, and fittingly looking at figure 51 the separation in question is small at these values. The velocity profile shows a greater extent of the forward flow across the tooth than in figure 53 (b), but a negative forward force overall. This would appear to be because the increased mass flow from the puck forces the forward flow down into the tooth, and thus it interacts much less with the puck itself. The reverse flow on the other hand has changed very little in terms of its extent and depth into the tooth. This explains the lobe of higher force at low mass flow and low φ and its subsequent decrease at higher values of mass flow seen in figures 48-50.

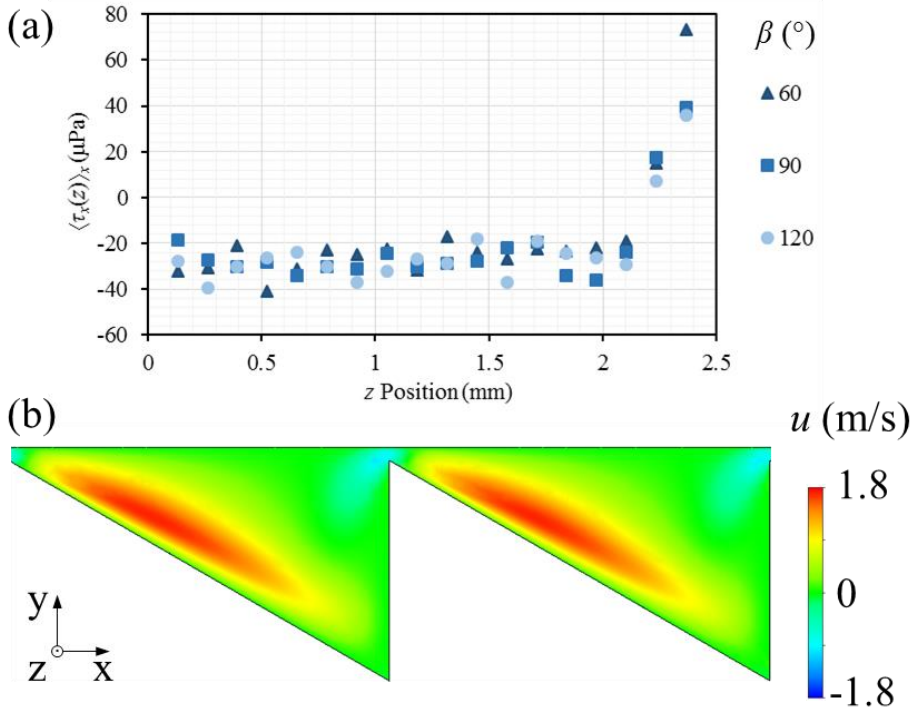

Figure 55. φ = 60°, d = 35µm, v_m = 1 m/s case. (a) Shear stress on the underside of the puck in the x direction, $\langle \tau_x(z) \rangle_x$. Displayed for three β values. The centre symmetry plane of the puck is at 0mm and the edge at 2.5 mm. (b) Velocity in the x direction on a plane 1.25 mm from the centre of the puck at, β = 90°.

Figure 56 shows the shear stresses for a low and high mass flow case for a very shallow tooth. The low mass flow case has a more significant drop at the edge than the comparable deep tooth case (figure 52), but otherwise these graphs are qualitatively very similar to the deep tooth case previously discussed.

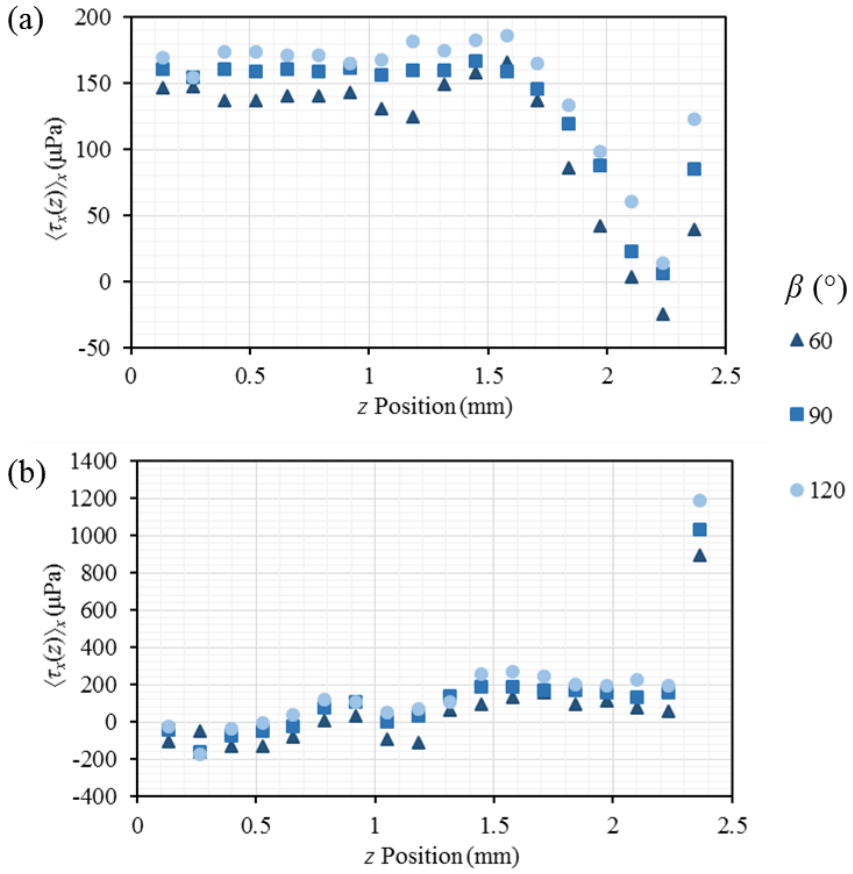

Figure 56. Shear stress on the underside of the puck in the x direction, $\langle \tau_x(z) \rangle_x$ for φ = 87°, d = 35μm, (a) v_m = 0.2 m/s and (b) v_m = 1 m/s. Displayed for three β values. The centre symmetry plane of the puck is at 0 mm and the edge at 2.5 mm.

Comparing the x velocity profiles in figure 57 with those in figure 53 (b) and figure 55 (b) however, show a significant difference between the deep and shallow tooth case. There is so little space for the flow to be pushed down into at higher mass flow rates, the flow is interacting well with the puck at high mass flow as well as at low mass flow. As a result, the viscous force acting on the puck will continue to increase as mass flow rate increases. This is the main reason for F_x continuing to increase with mass flow in the case of shallow teeth.

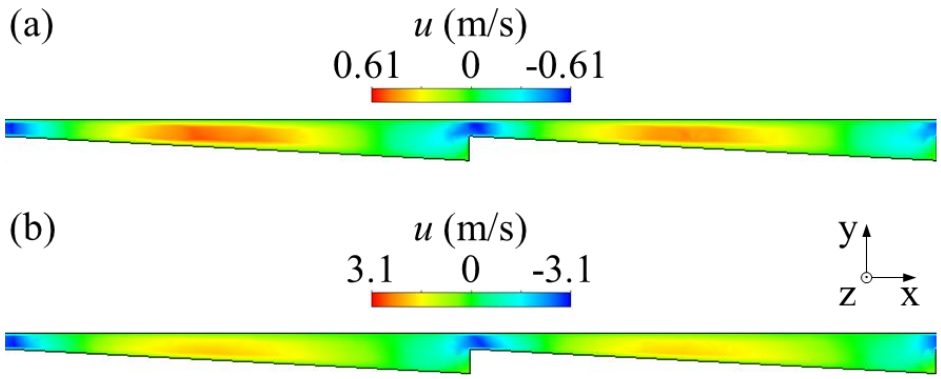

Figure 57. Velocity in the *x* direction on a plane 1.25 mm from the centre of the puck at φ = 87°, *d* = 35µm, β = 90° (a) v_m = 0.2 m/s and (b) v_m = 1 m/s.

The effect of increasing the distance between the puck and the teeth is to reduce the force acting on the puck. Comparing example vapour flows at *d* = 100µm in figure 58 (a) and (b) with their *d* = 35µm counterparts in figure 59 (c) and (d) (replotted from figure 53 (b) and 55 (b)) it can be seen that the maximum velocity in the negative direction is much closer to

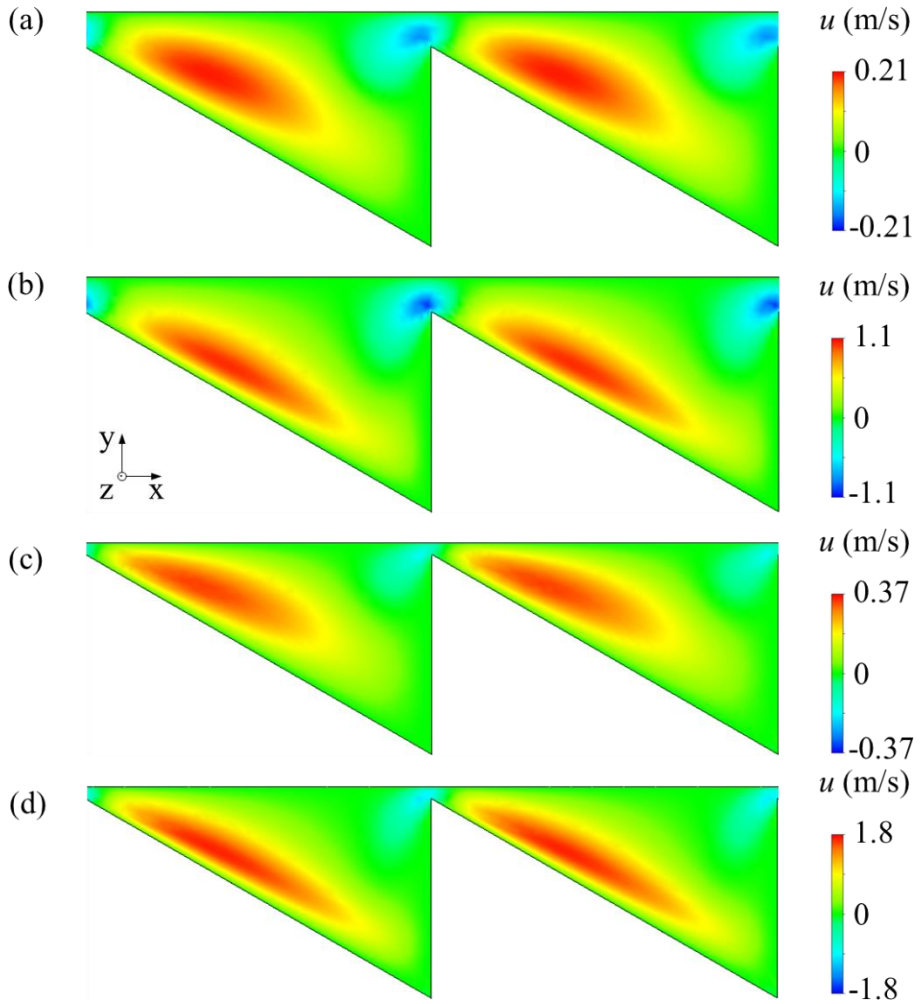

Figure 58. Velocity in the *x* direction on a plane 1.25 mm from the centre of the puck at φ = 60°, β = 90° (a) v_m = 0.2 m/s, *d* = 100µm, (b) v_m = 1 m/s, *d* = 100µm, (c) v_m = 0.2 m/s, *d* = 35µm, (b) v_m = 1 m/s, *d* = 35µm. (c) and (d) are replotted from figure 53 (b) and 55 (b), respectively.

matching the maximum velocity in the positive direction for the d = 100μm case. Also, for the d = 100μm case, the negative velocity flow has more of an impact on the positive velocity flow, appearing to constrict it. Considering the meshing of the simulation, there are less mesh elements across the gap for a smaller d value. In the results displayed, it appears this increases the size of fluctuations in the data, and as such errors here are larger than for cases with more mesh elements across this gap.

The unexpected case of φ = 78° high mass flow rate will be considered next, where anti-overhang geometries have larger F_x. Figure 59 shows $\langle\tau_x(z)\rangle_x$ for the φ = 78°, d = 100μm, v_m = 1 m/s case, in which a clear qualitative difference can be seen in the β = 60° flow to the other cases. A noticeable dependence of the overall force on shear near the edge of the block is also evident.

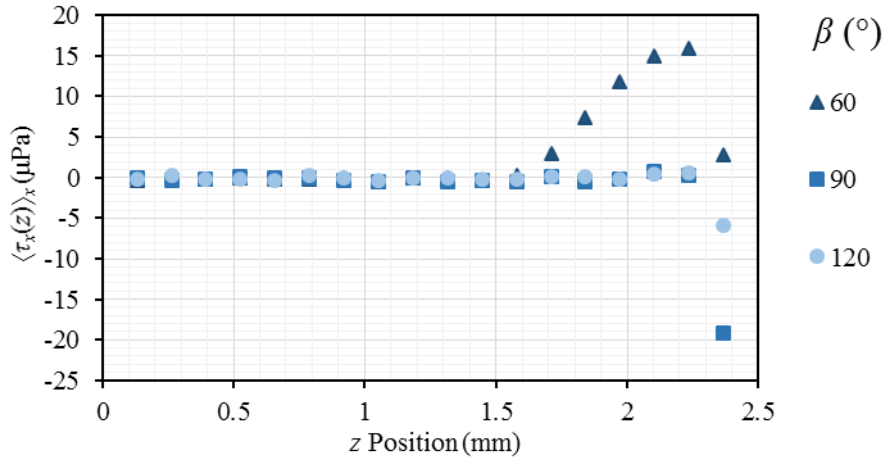

Figure 59. Shear stress on the underside of the puck in the x direction, $\langle\tau_x(z)\rangle_x$ for φ = 78°, d = 100 μm, v_m = 1 m/s. Displayed for three β values. The centre symmetry plane of the puck is at 0 mm and the edge at 2.5 mm.

Figure 60 shows the flow velocity in the x direction for a plane 2.2 mm from the centre of the block, lining up with the peak in shear stress for β = 60° in figure 59. A clear increase in the

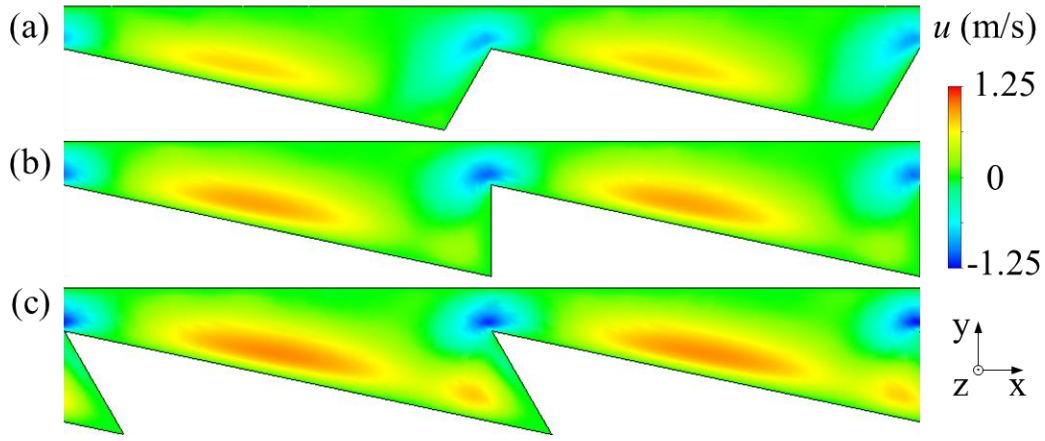

Figure 60. Velocity in the x direction on a plane 2.2 mm from the centre of the puck at φ = 78°, d = 100 μm, v_m = 1 m/s. (a) β = 60°, (b) β = 90° and (c) β = 120°.

backwards flow can be seen with increasing overhang, as well as an increase on the effect it has on the forwards flow as it splits the forward flow component in the $\beta = 90°$ and $\beta = 120°$ cases. The backflow also becomes more horizontal with increasing overhang. These factors are likely responsible for the negative dependence on overhang seen in figure 51 for $\varphi = 78°$, $d = 100\mu m$ at high mass flows.

This case can be compared to the $\varphi = 78°$, $d = 35\mu m$, $v_m = 1$ m/s case, for which $\langle \tau_x(z) \rangle_x$ is displayed in figure 61 (a). Again the edge of the puck can be seen to have the most contribution

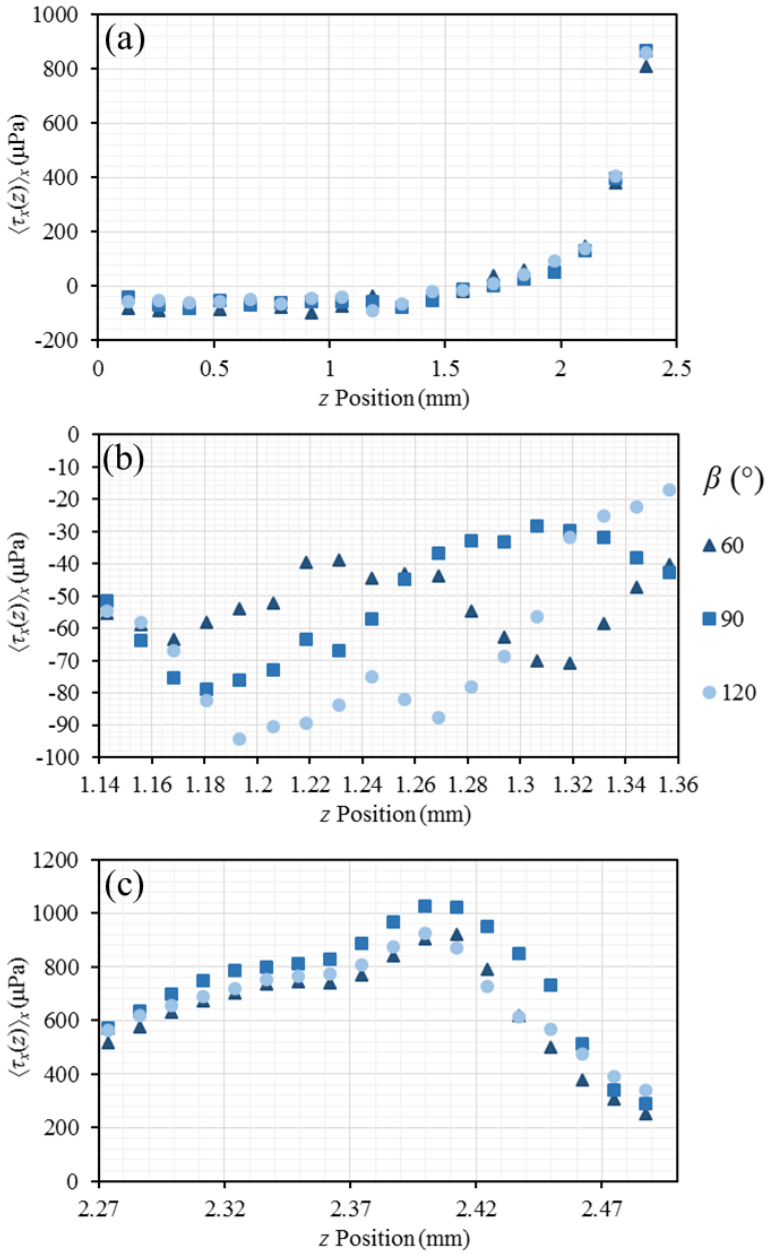

Figure 61. Shear stress on the underside of the puck in the x direction, $\langle \tau_x(z) \rangle_x$ for $\varphi = 78°$, $d = 35\mu m$, $v_m = 1$ m/s. Displayed for three β values. The centre symmetry plane of the puck is at 0 mm and the edge at 2.5 mm. (a) displays the whole data set, (b) zooms in to the structure midway between the symmetry plane and the puck edge and (c) zooms in to the structure at the edge of the puck.

to the forward force acting on it. Considering the effect of overhang, there is no such qualitative difference in the shear stress structure across the different β cases, even though β = 60° has a noticeably larger F_x. Looking at a finer resolution sample in figure 61 (b) there is a lot of fluctuation in the shear across the z dimension of the block. Taking a similar sample from the edge of the block, as shown in figure 61 (c), it can be seen that the flow at the edge of the block favours β = 60° having a lower F_x. This suggests in this case, despite the large jump in shear at the edge of the block, the bulk flow dictates the difference in propulsion of the β cases.

As well as F_x, F_y acting on the puck was output from the simulations. F_y gives information about what height the puck would sit at above the teeth, by balancing the weight of the puck with this force. This is crucial in evaluating realistic CO_2 puck behaviour to use as a comparison to droplet behaviour. The next subsection on the equilibrium case will discuss this in more detail. Here, the form of F_y is evaluated, and found to be mostly dependent on the mass flow in and the volume of space between the puck and the ratchet teeth. An example of a contour plot for F_y against φ and v_m is given in figure 62. All the contour plots seen in the tested range are qualitatively the same. F_y is found to decrease slightly as overhang angle increases, as this introduces more volume beneath the puck. In reality, this would mean that droplets and pucks sit lower in teeth with larger overhangs.

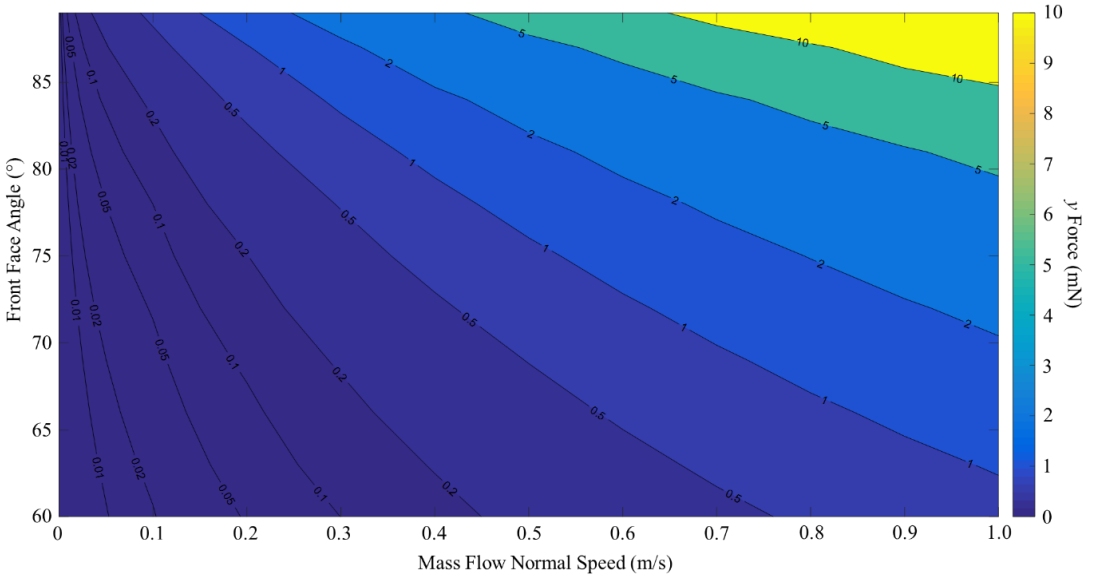

Figure 62. Simulation data for force acting on a dry ice puck in the y direction. d = 100μm, β = 120.

4.3.2 Equilibrium Case

Data for anti-overhang, vertical backed and overhang teeth is show in figures 63-65. The graphs of $F_{eqx}(T)$ are to be compared with those in figure 40, with F_{eqx} being the driving force leading to the velocity experienced by the droplets/pucks.

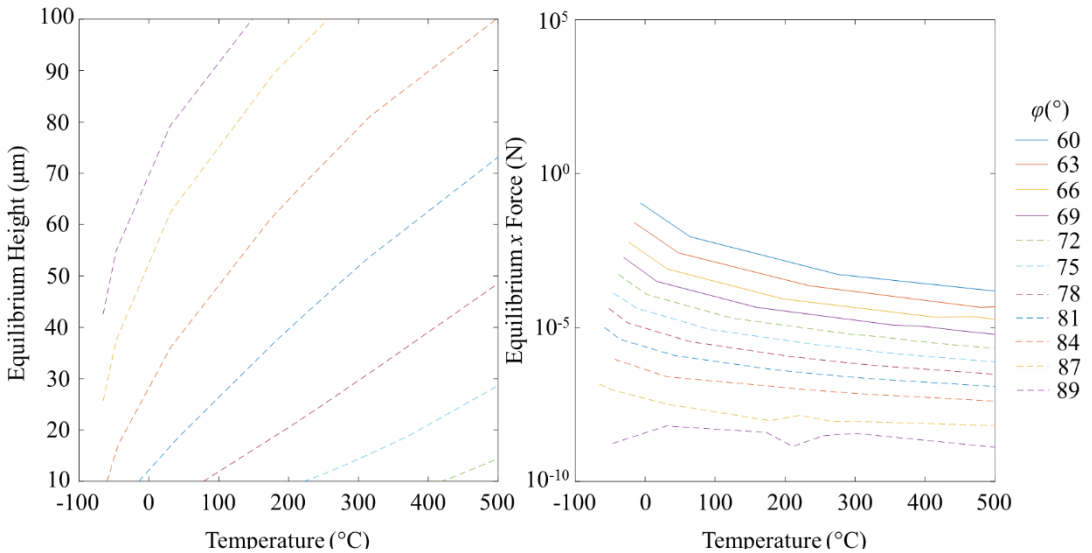

Figure 63. Equilibrium height and F_x across values of the front face angle, φ, for $\beta = 60°$.

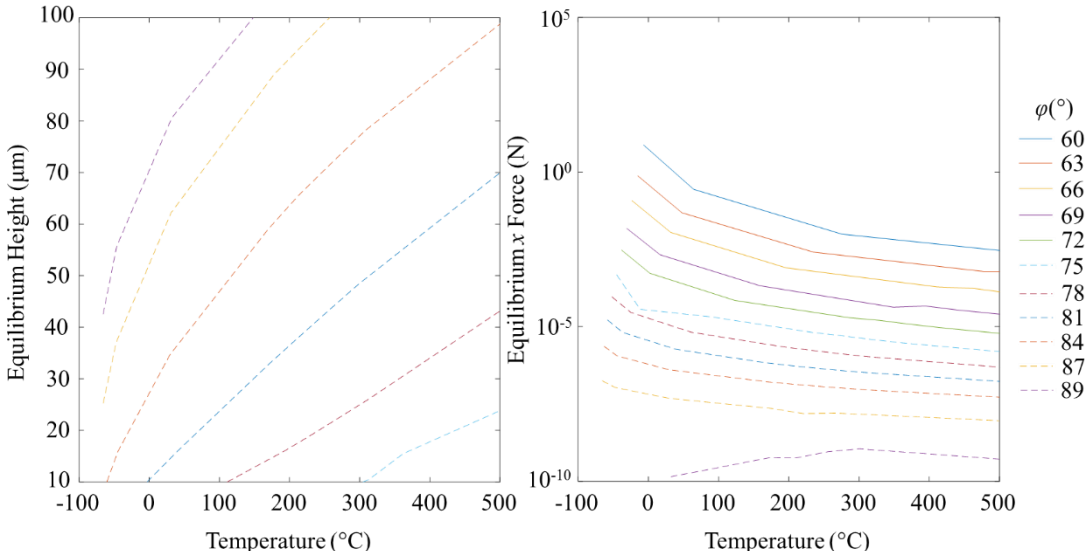

Figure 64. Equilibrium height and F_x across values of the front face angle, φ, for $\beta = 90°$.

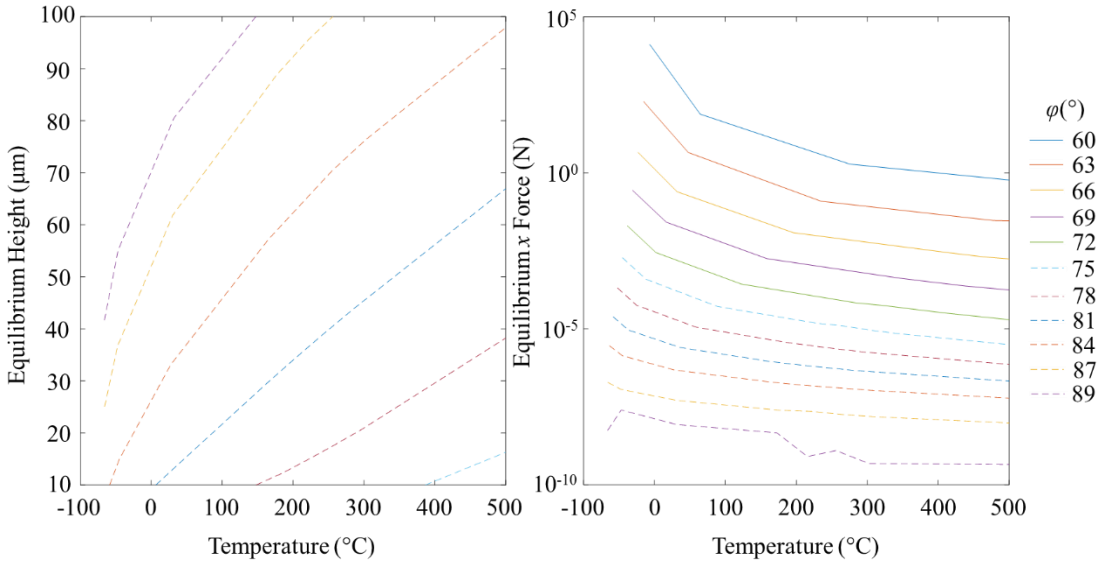

Figure 65. Equilibrium height and F_x across values of the front face angle, φ, for $\beta = 120°$.

For each β value, at a specific temperature, pucks above deeper teeth experience a larger driving force whilst sitting at a lower height above the teeth. The height decrease is simply a result of the extra space beneath the teeth reducing F_y acting on the puck. As seen in the parametric study, increasing height reduces overall force on the puck. The result of force increasing with deepening teeth for a dry ice puck is also predicted in figure 4 of reference [4]. This would seem counter to what is seen in experimental droplet studies as deeper teeth produce some of the slowest droplet movements recorded. Here droplet deformation needs to be considered as the reason for this disparity. This deformation adds a frictional force due to collisions with the tops of teeth and the potential energy barriers the drop must overcome from moving in and out of the teeth [5, 43]. These two components scale the frictional force with h (tooth height) and h^2 respectively [43]. This frictional force therefore increases for deeper teeth and would appear to contribute significantly to the overall force acting on droplets for all but the shallowest of teeth. It is entirely possible therefore that for pucks, acceleration and therefore terminal velocity does increase with tooth depth, although no experimental data currently exists to support this conclusion. It is hypothesised that, past some critical value of φ, F_{eqx} would begin to decrease, as the direction of the flow becomes directed increasingly into the teeth by the steepening gradient of the teeth.

F_{eqx} is seen to decrease with increasing temperature for specific geometry as well as the puck sitting at a lower equilibrium height. For droplets, the velocity increases to a peak then decreases with temperature. The difference in behaviour is hypothesised to be due to the lack of transition behaviour for dry ice pucks when compared to droplets. This transition behaviour has been seen to give increase droplet velocity through explosive contact boiling events at the tops of the ratchet teeth [33, 40]. As well as this, the previously-discussed frictional force has a higher contribution at lower temperatures, as the droplets would deform more into the teeth at the lower equilibrium heights. Both of these factors could cause the peaking behaviour seen for the droplet data. For both droplets and pucks, the equilibrium height increasing would be expected to cause a lower velocity, as the flow would interact less and less with the teeth.

Equilibrium data can be compared to the flow patterns seen in the parametric study by considering the distributions of heights and mass flow rates for each tooth shape. It is hypothesised that all shallow tooth flows are qualitatively similar to those seen in figure 57 for the majority of the temperature range, moving away from this shallow constricted flow at very low mass flow rates/temperatures. Deep teeth are expected to move qualitatively from flow patterns seen in figure 53 to figure 58 (b) as temperature increases.

It is also possible to feed points from the equilibrium curves back into the simulation to produce flow visualisations under these conditions. Figures 66-68 give an example of this for

a mid-depth tooth at the high end of temperatures considered for equilibrium data on an *xy* plane midway between the symmetry plane and the edge of the block. Similarities in the flow shape and the evolution of the backwards facing flow components with changing overhang can be seen with the previously discussed flow patterns in the parametric study.

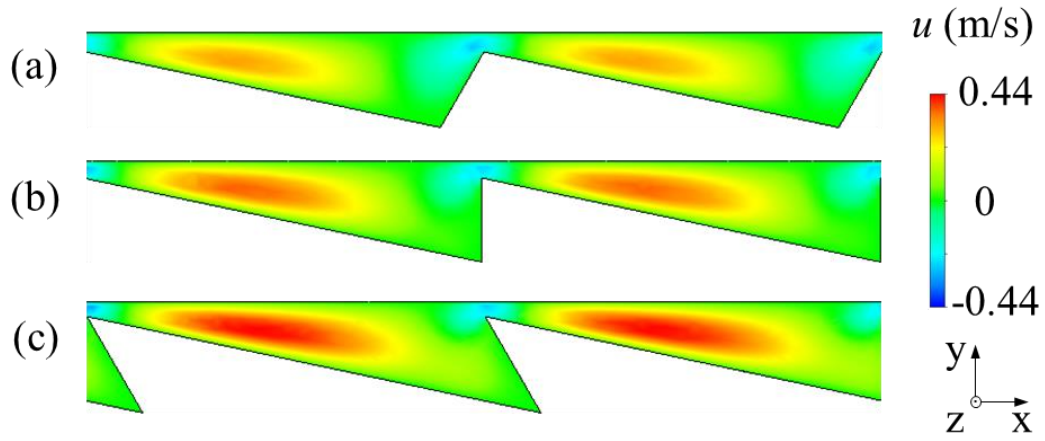

Figure 66. Equilibrium *x* flow velocity data for φ = 78° at *T* = 500°C halfway between the puck centre and edge. (a) β = 60°, (b) β = 90° and (c) β = 120°.

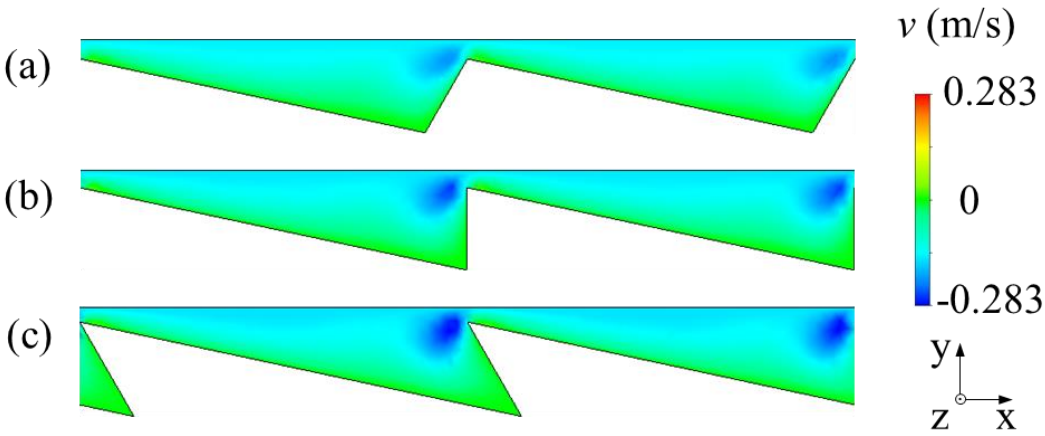

Figure 67. Equilibrium *y* flow velocity data for φ = 78° at *T* = 500°C halfway between the puck centre and edge. (a) β = 60°, (b) β = 90° and (c) β = 120°.

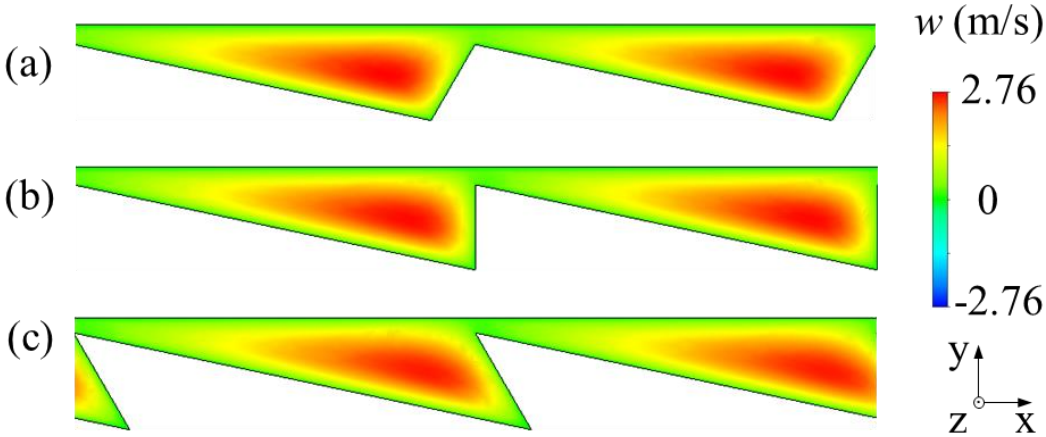

Figure 68. Equilibrium *z* flow velocity data for φ = 78° at *T* = 500°C halfway between the puck centre and edge. (a) β = 60°, (b) β = 90° and (c) β = 120°.

In the same way, an *xz* plane can be taken midway between the tooth top and the puck as in figure 69. All the plots shown in figure 68 show a clear difference between bulk flow and flow at the edge of the block. There is also a clear increase in the size of the forward *u* region with increasing overhang angle.

Finally, figure 70 shows a vector representation of the flow in the same *xy* plane as in figure 66-68. The vectors are projected onto the plane and scaled in size based on their magnitude.

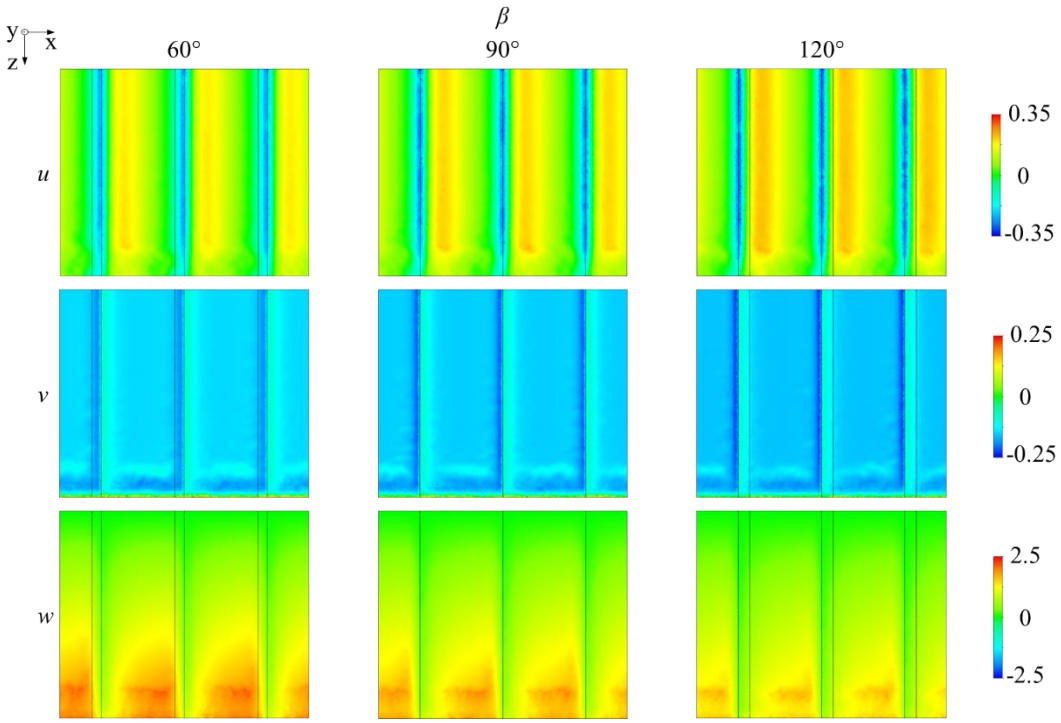

Figure 69. Equilibrium flow velocity data for φ = 78° at T = 500°C halfway between the tooth top and the underside of the puck.

4.3.3 Discussion on Overhang Geometries

Bouillant et al. [20] have experimentally shown that Leidenfrost droplets can be subject to symmetry breaking resulting from vapour flow. The flow visualisation from the parameter study (figure 53) shows a noticeable leaning towards forward flow dominating with higher overhang angles, this could improve reliability in the droplets by biasing flow forwards. Similarly, the overhang allows and escape route for outflow that had less influence on the underside of the puck/droplet (as the flow is separated from the drop by the tooth). This will reduce any lateral bias droplets may experience from this outflow, enhancing reliability in cases where droplets may have otherwise left the block sideways.

From the equilibrium data it can be seen increasing overhang decreases equilibrium height, as this creates more space in the tooth. Force increases with this height decrease. The same flow

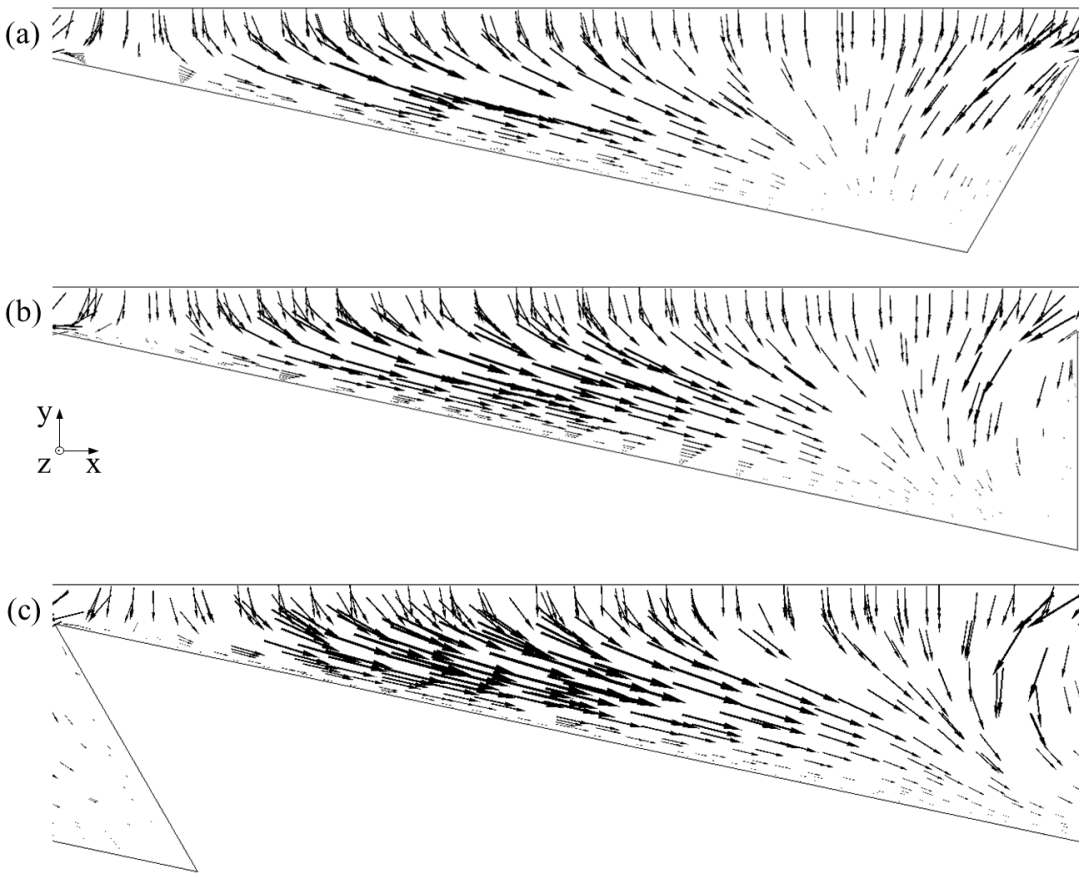

Figure 70. Equilibrium flow velocity data for $\varphi = 78°$ at $T = 500°C$ halfway between the puck centre and edge. (a) $\beta = 60°$, (b) $\beta = 90°$ and (c) $\beta = 120°$. Vectors projected onto this plane and scaled in size based on their magnitude.

characteristic changes seen in the parametric study can be seen within the equilibrium data, as shown in figures 66-68.

The limited effect of overhang on the equilibrium F_x of shallower teeth (as seen in figures 63-65) confirms the area being introduced by the overhang to be the most important component in its effect on puck driving force, as increasing the overhang of shallower teeth introduces much less space beneath the tooth than for deeper teeth.

4.4 Conclusions

The performed parameter study reveals many points of interest on how vapour between a solid puck and ratchet teeth flows, and how this affects the force on the puck. There is always a clear quantitative difference of the x shear contributions on the puck between the main body of the puck and positions close to its edge, although the nature of this difference is not consistent from case to case. At high mass flow these edge effects contribute significant amounts of the overall shear acting on the block. Also at high mass flow, for deeper teeth the forward flow is pushed down into the block, reducing its interaction with the bottom surface of the puck. This causes F_x acting on the puck to decrease at high mass flow for deeper teeth.

For shallow teeth, the forward flow has no space to be pushed down into at higher mass flow rates, within the range tested, so the flow looks qualitatively similar across mass flows, and F_x continues to increase for shallow teeth at high mass flow. Changing the overhang angle changes the flow pattern noticeably beneath the block. The extension of the forward and backward flows across the block, the depth they descend to in the tooth, and their relative strengths are all affected by ω. In most cases, F_x increases with overhang and F_y decreases with it. It does not seem to be simply the case that where the edge effects are dominating, the difference in vapour behaviour of the different overhang cases at the edge of the block would be representative of the different forces acting on the overall block.

It is possible to envisage a direct application of this situation described by the parameter study cases with air bearings. Combining air bearings with components with a ratchet surface could engineer a situation where the gas supplied by the air bearing both reduces friction and induces movement of the component.

Further to other models seen in the literature [4, 38], this work looks at the equilibrium cases for a puck of dry ice on a ratchet, as well as the simpler set height and mass flow case, allowing visualisation of the flow in these cases. The results compare favourably to other models. The equilibrium flow patterns are qualitatively similar to those seen within the parametric study. Pucks are seen to get a higher driving force for deeper teeth, owing to the extra space in the teeth allowing them to sit at a lower equilibrium height, and the lower heights favouring forward flow due to increased interaction of the flow with the teeth (as seen in the parametric study). Teeth with higher overhang angle experience a similar increase in driving force in the same way – as increasing overhang increases the space beneath the tooth. The simplifications that modelling dry ice allow when compared to droplets can be seen to affect the data considerably, further highlighting the importance of deformations in droplets on their dynamics.

5. Conclusions and Future Work

5.1 Conclusions

A variable Leidenfrost ratcheted surface has been designed and manufactured, which allowed for a broad range of ratchet shapes to be tested with self-propelling droplets, as well as the testing of new overhang geometries. Overhangs were found to increase the operational range and reliability of propelled droplets. Shallower teeth are found to produce faster droplets, with maximum speeds of 350mm/s.

Intended as a comparison to this data, a CFD model of a semi-infinite dry ice puck above variable ratchet teeth was set up. A parameter study was conducted, and a model of the equilibrium behaviour of the puck was devised. In the parameter study, a clear distinction is seen between the shear on the puck caused by vapour flow at the pucks edge, compared to the shear on the puck caused by the bulk flow beneath the puck. This distinction is a quantitative difference in the contribution of shear of the flow at these points. The nature of this difference changes on a case by case basis. A qualitative difference can be seen between the effects of having shallow and deeper teeth. As mass flow increases for deeper teeth, the flow is angled downwards and pushed further into the tooth, reducing force on the puck. Shallower teeth have no space to push the flow into, so the force keeps increasing with mass flow.

Within the parameter study, changing the overhang angle of the block changes the flow pattern significantly changing how far the forward and backward u flow extends across the block and their relative strengths. F_x increases slightly with overhang angle and F_y decreases with it in all but a few outlying cases. For the equilibrium case overhang angle decreases equilibrium height and forward driving force increases with this height decrease. The changes in the flow visualisation seen in the parameter study are repeated in the equilibrium case. Lateral flow bias is also reduced by the overhang separating the outflow from the underside of the puck. The combination of these effects is hypothesised to increase the reliability of pucks and droplets on an overhang surface.

In the equilibrium case, driving force is found to increase as teeth get deeper. This is because the puck sits at a lower height, constricting the gap between the teeth and the puck and increasing the interaction of the flow with the teeth.

In summary, the experimental and computational data have been combined to deepen understanding effect of the surface geometry on the droplet velocity, reliability and its vapour flow. A ratcheted pipe has been evaluated as an application for this phenomenon.

5.2 Future Work

This section looks at ways that the work performed here could be extended and expanded, as well as considering what such expansions might reveal.

On the experiments performed with the variable topography ratchet device, improvements could be made to allow it to generate a larger range of ratchet shapes. The device limits shown in figure 27 are purely a function of how far the set of plates can be inclined (as the alpha angles were also cut in the device). As mentioned in the description of the block, some of the plate incline angles, particularly near the extrema, required the addition of cap blocks to the clamping bars, to force the plates to a certain angle. Reducing the thickness of these components would allow the plates to incline more, and thus allow the device to access more of the space in figure 27. If an adjustable angle could be incorporated to the clamping end bar, it would also remove the need to make extra end caps for these angles. This adjustable angle would need to be able to be set rigid. Another alternative would be to find a different way to cut the plates, outside the device, improving the range in α angles reached.

By removing a small amount of material on one side of the plate, whilst leaving the full width of the plates at the edges, a new surface can be generated with the device that has air gaps at the base of the teeth. From previous work on the effect of porosity on film boiling [9, 14] it is likely that this would increase the Leidenfrost point, and depending on the size of the gap introduced, it may not be possible to support a film boiling droplet on it at a reasonable temperature. As such the gap should be kept small. The effect the gap would have on the flow beneath the droplet and thus droplet dynamics is unknown and would be the focus of such a study.

Another variable that could be considered to broaden this study is droplet size. This would be easy to vary with different diameter tubes and nozzles applied to the droplet dispensing pump. Considering some cases below, at and above the capillary length would give an overview of the effect of droplet size on ratchet shape dependence.

For the CFD simulations, future work involves moving towards a more realistic scenario, and experimentation with tooth shape. In terms of changing the tooth shape, the limitations are down to what can and cannot be meshed. Flats or rounds could be added to the peaks and/or troughs of the teeth to represent their degradation over time or poor manufacturing quality. Air gaps could be introduced to consider their effect on self-propulsion.

Another useful improvement to make to these simulations would be the refinement of the mesh, possibly using a different meshing package, to allow smaller values of d to be modelled. This would likely also reduce the size of errors due to the mesh.

To move to a more realistic simulation, the effects of temperature could be introduced, and the periodic boundaries removed. In general, the simulation would need to be moved towards a multiphase problem, with a droplet instead of a Leidenfrost solid.

Another option for an intermediate step to a more realistic solution would be to change the shape of the solid puck to one that has droplet deformation like protrusions into the ratchet teeth, and then model this with water vapour being produced on the underside of this puck.

Performing simple experiments of a dry ice puck on the variable ratchet used in chapter 3 would allow for a validation of the performed simulations.

All the improvements suggested here focus on increasing the scope of work already performed, either by increasing the range of variables already considered or adding more effects that have not already been tested. Increasing this scope will increase understanding of the underlying mechanics to the droplet self-propulsion.

5.3 Preliminary Study: Leidenfrost Pipes

5.3.1 Introduction

As part of efforts to move towards engineering applications an initial study was performed to investigate the possibility of moving liquid by coating the interior of pipes with ratchets. In this section the effects of lining a pipe with ratchets are evaluated in terms of the ability of the pipe to move liquid and its heat transfer properties. The pipe is tested initially in an open unpressurised state. It is hypothesised that this type of pipe may see use in a cooling application within a closed system, so its operation was tested under these conditions. Such an application would likely be within an engine system.

5.3.2 Unpressurised Test

To test the idea of a Leidenfrost Pipe a small pipe section was manufactured from thin plates with countersunk holes in them, held together in much the same way as the variable ratchet surface, within a tightening frame (shown in figure 71). A syringe was used to introduce slugs of water into the device, and within a similar temperature range to a standard ratcheted block, water was propelled through the device. High speed footage of water flowing through the device was taken, and air bubbles could be seen to be drawn into the water flow. These images can be seen in figure 72.

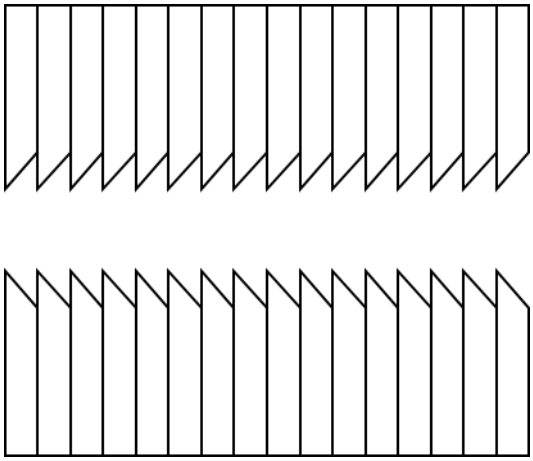

Figure 71. Diagram of plates with countersunk holes forming a pipe with a ratcheted interior.

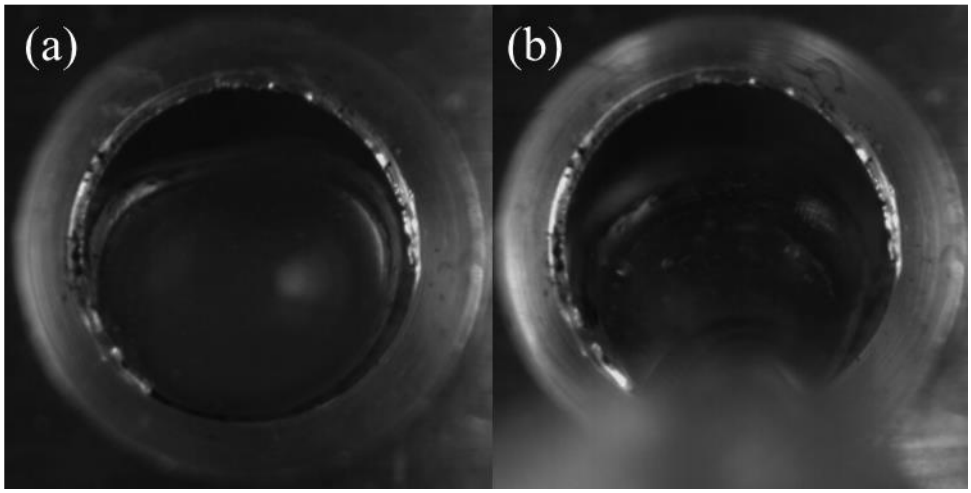

Figure 72. Stills from high speed footage of water moving through a pipe with ratchets along its length. Water is moving towards camera. (a) Shows the front of a slug. (b) Shows the middle of a slug with air bubbles in the water.

A solid block version of this device was constructed by cutting each of the teeth individually. Due to the size of the tool used, there was a limit on the length of the pipe that could be constructed of 30mm. A half pipe was created by cutting a full pipe block in half and used to introduce water droplets into the full blocks. At a temperature of approximately 300°C water droplets would propel through these pipes. To construct longer pipes these shorter pipes could be bound together with a threaded bar through their corners, and a thin gasket sheet between each pair of sections.

Having proved that the concept works in an unpressurised scenario, the next stage of this process was to develop a more rigorous experiment to determine the heat transfer properties of a Leidenfrost pipe as compared to a clean pipe.

5.3.3 Experimental Methods

5.3.3.1 Leidenfrost Pipe

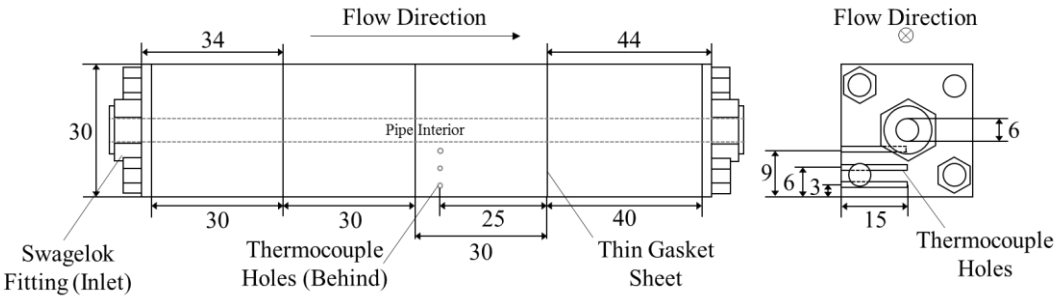

Figure 73. Schematic of pipe test block. Dimensions in mm.

Figure 73 shows a schematic diagram of the Leidenfrost pipe test block. To create the pipe section four lengths of ratcheted pipe were cut and bound as described in subsection 5.3.2. The ratchets were 0.3mm in height and 1mm in pitch with a vertical back and a 6mm inner diameter (extending to a 6.6mm outer diameter). This gives a front face angle, φ = 73.3°. In each of the two end sections of the pipe space for a threaded Swagelok fitting was also cut. The tool used to cut the teeth could only cut teeth facing in one direction, so the first (inlet) block had to have space for the Swagelok fitting cut destructively, i.e. it removed teeth to make space for the fitting. The last (outlet) block could simply be made longer to provide space for the fitting. The Swagelok fitting connected to a copper pipe to join the test pipe section to the rest of the system. The four pipe sections were connected using a threaded bar in two diagonally opposite corners of the block, with nuts tightening the complete block together. A thin gasket sheet was placed between each pair of sections of the pipe, and a steel end plate at each end of the pipe, with a hole for the Swagelok fitting. Three holes were used to measure temperature with thermocouples on the third block, placed in the centre of the ratcheted section, drilled through to the centre of the block, at 3, 6 and 9 mm from the base. A pipe with no ratchets was created in the same way, except a standard hole was cut instead of ratchet teeth. The hole was diameter 6mm to match with the inner diameter of the ratcheted pipe.

5.3.3.2 Experimental Setup

Figure 74 shows the experimental setup. Data from the flow meter (Atrato Ultrasonic Flow Meter), pressure sensor (Jumo Pressure Sensor), and thermocouples inserted into the test pipe are recorded in a LabVIEW program. Thermocouples are read once every ~0.4s and the flow meter and pressure sensor are read 100 times a second. Deionised water is added to the system at the water inlet until it fills the glass condenser at least halfway. The water is no further forward than the peristaltic pump (as it cannot pass this unless the pump is running). The pressure relief valve is set to 1 bar above atmospheric pressure. The test pipe is covered in a

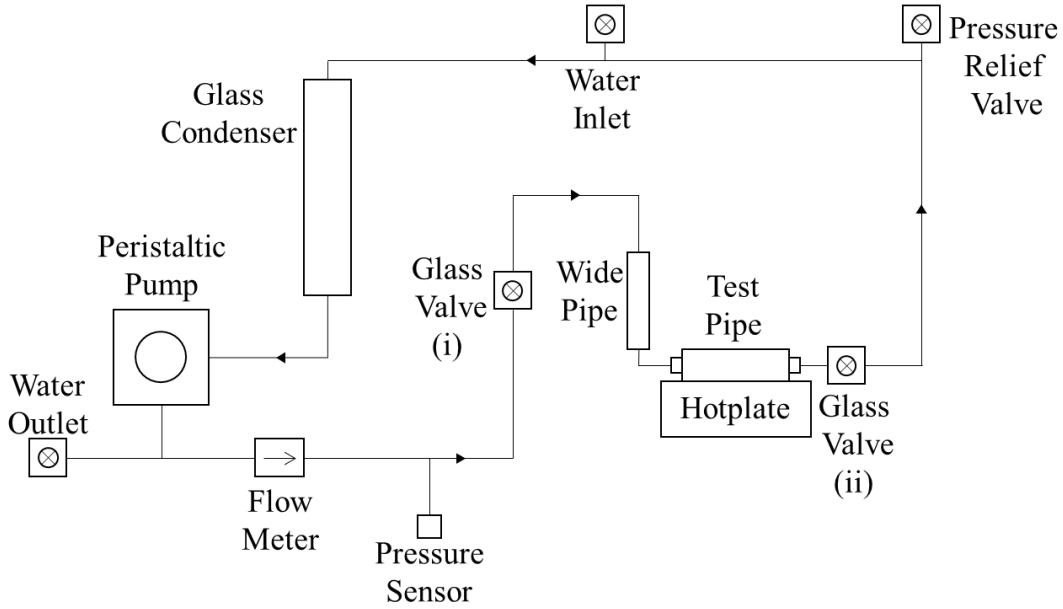

Figure 74. Diagram of experimental setup for testing heat transfer properties of the test pipe. Fluid flow in direction of arrows.

glass fibre based insulating material to increase the temperature it can be heated to. It is also tightened to a plate of aluminium to hold it in place and increase the thermal contact between it and the ceramic hotplate.

To perform a test, the test pipe starts with no water in it and is heated by the hotplate. When the pipe reaches equilibrium at a high temperature, the water pump is turned on at 3% of its maximum speed. This is the slowest the pump can be run without stalling. The pump is run at this speed to reduce the cooling power of the water flow to allow the pipe to maintain temperature. The water movement due to the pump alone is not registered by the flow meter, which detects a minimum flow rate of 0.0256 L/min. The point where the water passes the first glass valve (i) is marked as the start of the experiment, although it is a short time (on the order of seconds) before the point where the water will reach the test pipe, it is not possible see when the water contacts the pipe.

The wide pipe section before the test pipe is designed to cause the water to drip past the section of pipe that is at transition boiling temperature and straight onto a section that is above the Leidenfrost temperature, reducing cooling on the test pipe and allowing it to maintain a higher temperature.

Once water is flowing through the test pipe, the pressure, flow and temperature data is recorded until the thermocouple temperatures reach some equilibrium, or the water level in the system reduces such that is no longer visible in the glass condenser. The heat flux is estimated by approximating the heat flow to 1D and linear from the thermocouple closest to

the hotplate to the thermocouple farthest from the hotplate. In practice this means that the heat flux is calculated as

$$q = \frac{k(T_1 - T_3)}{s_t}, \tag{14}$$

where k is the thermal conductivity of the test pipe (made of aluminium, which has a conductivity of 205 $Wm^{-1}K^{-1}$), T_1 is the temperature of the thermocouple closest to the hotplate, T_3 is the temperature of the thermocouple closest to the pipe centre, and s_t is the distance between these two thermocouples.

5.3.4 Results and Discussion

The temperature profiles for tests with an unratcheted and ratcheted pipe are presented in figure 75. The clean pipe cools slower, but reaches an equilibrium temperature of 235℃, whereas the ratcheted pipe does not reach equilibrium before the test ends. This temperature data can be used to calculate heat flux for heating and cooling across the temperatures reached. The heating is recorded as the pipe heats with no water in it before the test begins, the cooling is recorded during the test as the water flows through the pipe. This data is displayed in figure 76.

Here, substantially different heat flux profiles can be seen across the two cases. This, coupled with the temperature data seen in figure 75, suggests that for the duration of the experiment the different pipes contain water in different boiling states. The clean pipe with its smoother temperature profile and equilibrium temperature is in the film boiling regime, whereas the ratcheted pipe, with its spikier, more random, temperature profile, is in a transition boiling regime. The ratcheted pipe also has higher heat flux, which also correlates with a transition boiling state, as the surface contacts in this regime cause explosive boiling, and thus cooling in the pipe. To complement this, at the higher temperature end of the heat flux data, as the liquid state should be moving towards Leidenfrost boiling, the heat flux profile becomes much less spread.

For both pipes, pulses of water are seen flowing through the second clear glass valve, and the flow meter detects this pulsing. Whilst the pulsing was observed to be more forceful in the case of the ratcheted pipe (with the pipes visibly shaking much more) there is no way to determine from the flow data which flow is due to the ratchets self-propelling droplets/slugs and what flow is due to pressure build up in the system from steam production.

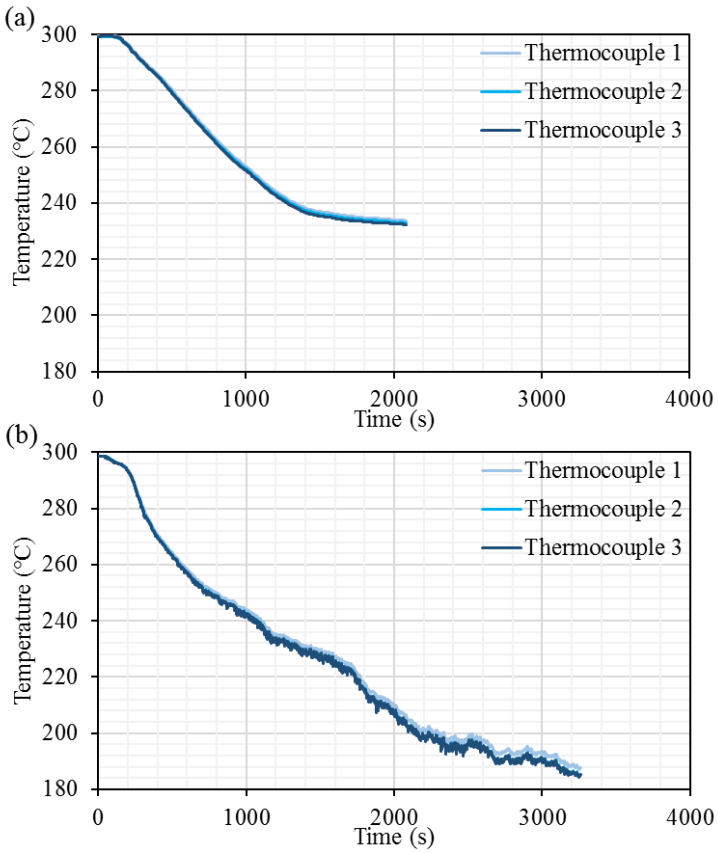

Figure 75. Thermocouple temperatures (1 closest to plate, 3 farthest from plate) in the test pipe from the point water reaches the glass valve. (a) Clean pipe. (b) Ratcheted pipe.

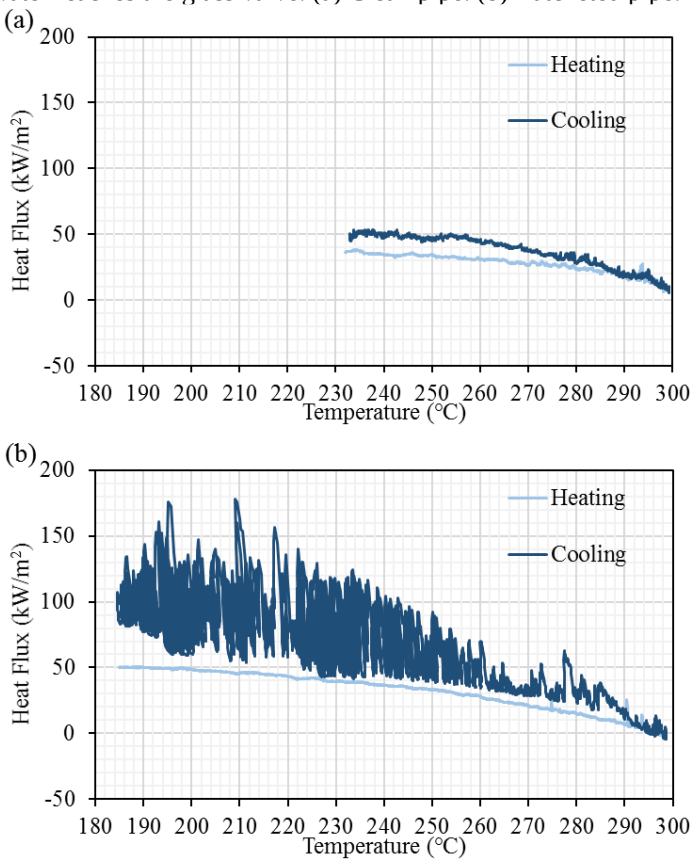

Figure 76. Heat flux across thermocouples 1 and 3. The cooling data maps to the thermocouple data in figure 75. (a) Clean pipe. (b) Ratcheted pipe.

The evolution of pressure with time is shown in figure 77. Here it can be seen that the pressure never reaches the 1 bar that the pressure relief valve was quoted to be set to. However, gas was seen to be released from the valve at points throughout both experiments, although considerably more noticeably and consistently in the case of the ratchet pipe. The ratchet pipe had also decreased significantly in water level by the end of the experiment. Therefore, it is concluded that the pressure relief valve opens, at least partially, well below its stated pressure value. Also, there is much more steam production for the transition boiling case. As it is in the transition state, the boiling can be expected to be explosive, which accounts for the larger pressure fluctuations seen in 75 (b).

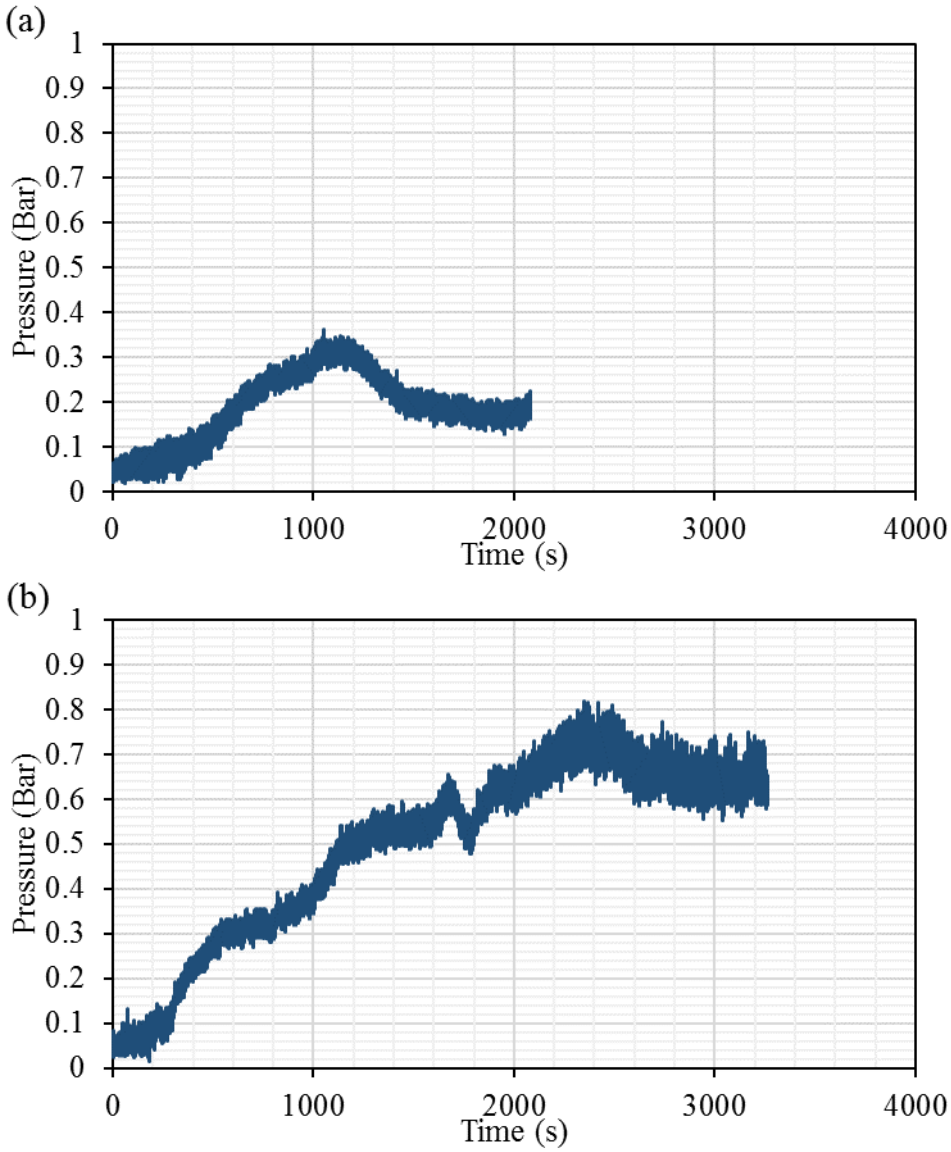

Figure 77. Gauge pressure within the closed pipe system, measured from the point water reaches the glass valve. (a) Clean pipe. (b) Ratcheted pipe.

5.3.5 Conclusions and Future Work

From the data obtained, it is clear that adding ratchets to a pipe interior changes the boiling profile of the water, increasing the cooling of the pipe by increasing the temperature range of the transition boiling regime. This result suggests that the Leidenfrost pipes could be used in a cooling application.

In terms of liquid movement, it cannot currently be said which of the two pipes moves liquid more efficiently. Further work will be required to conclude this.

There are two clear ways to improve the work on Leidenfrost pipes. The first is to try to confirm if the ratchets are improving the flow of water around the closed system. One way to move towards testing this would be to increase the temperature of the pipes, so that they were both in the Leidenfrost regime. This would require a more powerful hotplate, a more even heating system or more efficient insulation than is currently available. This would reduce the disparity in water flow that is due to pressure build up across the two cases.

Testing more tooth shapes at different pressures would help to increase the understanding of these pipes. The previous studies in this work could be used to inform which teeth to test. To move entirely towards a cooling pipe, deeper teeth might be tested for example, as the deformations of droplets into these would be expected to increase the chance of transition boiling contacts. To have a pipe move water more quickly it would be expected to need shallower teeth.

References

[1] J. G. Leidenfrost, "On the fixation of water in diverse fire," *International Journal of Heat and Mass Transfer,* vol. 9, no. 11, pp. 1153-1166, 1966.

[2] H. Linke, B. J. Aleman, L. D. Melling, M. J. Taormina, M. J. Francis, C. C. Dow-Hygelund, V. Narayanan, R. P. Taylor, and A. Stout, "Self-propelled Leidenfrost droplets," *Phys Rev Lett,* vol. 96, no. 15, p. 154502, Apr 21 2006.

[3] D. Quéré, "Leidenfrost Dynamics," *Annual Review of Fluid Mechanics,* vol. 45, no. 1, pp. 197-215, 2013.

[4] T. Baier, G. Dupeux, S. Herbert, S. Hardt, and D. Quere, "Propulsion mechanisms for Leidenfrost solids on ratchets," *Phys Rev E Stat Nonlin Soft Matter Phys,* vol. 87, no. 2, p. 021001, Feb 2013.

[5] G. Lagubeau, M. Le Merrer, C. Clanet, and D. Quéré, "Leidenfrost on a ratchet," *Nature Physics,* vol. 7, no. 5, pp. 395-398, 2011.

[6] J. D. Bernardin and I. Mudawar, "The Leidenfrost point: Experimental study and assessment of existing models," *Journal of Heat Transfer-Transactions of the Asme,* vol. 121, no. 4, pp. 894-903, Nov 1999.

[7] A.-L. Biance, C. Clanet, and D. Quéré, "Leidenfrost drops," *Physics of Fluids,* vol. 15, no. 6, p. 1632, 2003.

[8] B. S. Gottfried, C. J. Lee, and K. J. Bell, "The Leidenfrost Phenomenon: Film Boiling of Liquid Droplets on a Flat Plate," *International Journal of Heat and Mass Transfer,* vol. 9, no. 11, pp. 1167-1188, 1966.

[9] C. T. Avedisian and J. Koplik, "Leidenfrost Boiling of Methanol Droplets on Hot Porous Ceramic Surfaces," (in English), *International Journal of Heat and Mass Transfer,* vol. 30, no. 2, pp. 379-393, Feb 1987.

[10] J. D. Bernardin and I. Mudawar, "A Cavity Activation and Bubble Growth Model of the Leidenfrost Point," *Journal of Heat Transfer,* vol. 124, no. 5, p. 864, 2002.

[11] Y. Takata, S. Hidaka, J. M. Cao, T. Nakamura, H. Yamamoto, M. Masuda, and T. Ito, "Effect of surface wettability on boiling and evaporation," *Energy,* vol. 30, no. 2-4, pp. 209-220, 2005.

[12] G. Bleiker and E. Specht, "Film evaporation of drops of different shape above a horizontal plate," *International Journal of Thermal Sciences,* vol. 46, no. 9, pp. 835-841, 2007.

[13] J. H. Snoeijer, P. Brunet, and J. Eggers, "Maximum size of drops levitated by an air cushion," *Phys Rev E Stat Nonlin Soft Matter Phys,* vol. 79, no. 3 Pt 2, p. 036307, Mar 2009.

[14] H. Kim, B. Truong, J. Buongiorno, and L.-W. Hu, "On the effect of surface roughness height, wettability, and nanoporosity on Leidenfrost phenomena," *Applied Physics Letters,* vol. 98, no. 8, p. 083121, 2011.

[15] J. C. Burton, A. L. Sharpe, R. C. van der Veen, A. Franco, and S. R. Nagel, "The Geometry of the Vapor Layer Under a Leidenfrost Drop," *Phys Rev Lett,* vol. 109, no. 7, p. 074301, Aug 17 2012.

[16] B. Sobac, A. Rednikov, S. Dorbolo, and P. Colinet, "Leidenfrost effect: Accurate drop shape modeling and refined scaling laws," *Phys Rev E Stat Nonlin Soft Matter Phys,* vol. 90, no. 5-1, p. 053011, Nov 2014.

[17] F. Celestini, T. Frisch, and Y. Pomeau, "Take off of small Leidenfrost droplets," *Phys Rev Lett,* vol. 109, no. 3, p. 034501, Jul 20 2012.

[18] L. Maquet, M. Brandenbourger, B. Sobac, A. L. Biance, P. Colinet, and S. Dorbolo, "Leidenfrost drops: Effect of gravity," *EPL (Europhysics Letters),* vol. 110, no. 2, p. 24001, 2015.

[19] T. Roques-Carmes, A. Domps, P. Marchal, and L. Marchal-Heussler, "Equivalent capacitive thickness of the vapor layer below Leidenfrost drops," (in English), *Experiments in Fluids,* vol. 59, no. 7, Jul 2018.

[20] A. Bouillant, T. Mouterde, P. Bourrianne, A. Lagarde, C. Clanet, and D. Quéré, "Leidenfrost wheels," *Nature Physics,* 2018.

[21] Y. M. Qiao and S. Chandra, "Experiments on adding a surfactant to water drops boiling on a hot surface," (in English), *Proceedings of the Royal Society a-Mathematical Physical and Engineering Sciences,* vol. 453, no. 1959, pp. 673-689, Apr 8 1997.

[22] F. Moreau, P. Colinet, and S. Dorbolo, "Explosive Leidenfrost droplets," *Physical Review Fluids,* vol. 4, no. 1, 2019.

[23] F. Celestini and G. Kirstetter, "Effect of an electric field on a Leidenfrost droplet," *Soft Matter,* vol. 8, no. 22, p. 5992, 2012.

[24] K. Piroird, C. Clanet, and D. Quéré, "Magnetic control of Leidenfrost drops," *Phys Rev E Stat Nonlin Soft Matter Phys,* vol. 85, no. 5 Pt 2, p. 056311, May 2012.

[25] B. T. Ng, Y. M. Hung, and M. K. Tan, "Suppression of the Leidenfrost effect via low frequency vibrations," *Soft Matter,* vol. 11, no. 4, pp. 775-84, Jan 28 2015.

[26] B. T. Ng, Y. M. Hung, and M. K. Tan, "Acoustically-controlled Leidenfrost droplets," *J Colloid Interface Sci,* vol. 465, pp. 26-32, Mar 01 2016.

[27] T. Y. Xiong and M. C. Yuen, "Evaporation of a Liquid Droplet on a Hot Plate," (in English), *International Journal of Heat and Mass Transfer,* vol. 34, no. 7, pp. 1881-1894, Jul 1991.

[28] S. Chandra and C. T. Avedisian, "On the Collision of a Droplet with a Solid-Surface," (in English), *Proceedings of the Royal Society-Mathematical and Physical Sciences,* vol. 432, no. 1884, pp. 13-41, Jan 8 1991.

[29] J. D. Bernardin, C. J. Stebbins, and I. Mudawar, "Mapping of impact and heat transfer regimes of water drops impinging on a polished surface," *International Journal of Heat and Mass Transfer,* vol. 40, no. 2, pp. 247-267, 1997.

[30] J. D. Bernardin, C. J. Stebbins, and I. Mudawar, "Effects of surface roughness on water droplet impact history and heat transfer regimes," *International Journal of Heat and Mass Transfer,* vol. 40, no. 1, pp. 73-88, Jan 1997.

[31] G. P. Celata, M. Cumo, A. Mariani, and G. Zummo, "Visualization of the impact of water drops on a hot surface: effect of drop velocity and surface inclination," *Heat and Mass Transfer,* vol. 42, no. 10, pp. 885-890, 2006.

[32] A.-L. Biance, C. Pirat, and C. Ybert, "Drop fragmentation due to hole formation during Leidenfrost impact," *Physics of Fluids,* vol. 23, no. 2, p. 022104, 2011.

[33] A. Grounds, R. Still, and K. Takashina, "Enhanced droplet control by transition boiling," *Sci Rep,* vol. 2, p. 720, 2012.

[34] G. Dupeux, M. Le Merrer, G. Lagubeau, C. Clanet, S. Hardt, and D. Quéré, "Viscous mechanism for Leidenfrost propulsion on a ratchet," *EPL (Europhysics Letters),* vol. 96, no. 5, p. 58001, 2011.

[35] Z. H. Jia, M. Y. Chen, and H. T. Zhu, "Reversible self-propelled Leidenfrost droplets on ratchet surfaces," (in English), *Applied Physics Letters,* Article vol. 110, no. 9, p. 5, Feb 2017, Art. no. 091603.

[36] A. Wuerger, "Leidenfrost Gas Ratchets Driven by Thermal Creep," *Physical Review Letters,* vol. 107, no. 16, Oct 13 2011, Art. no. 164502.

[37] S. Hardt, S. Tiwari, and T. Baier, "Thermally driven flows between a Leidenfrost solid and a ratchet surface," *Phys Rev E Stat Nonlin Soft Matter Phys,* vol. 87, no. 6, p. 063015, Jun 2013.

[38] T. R. Cousins, R. E. Goldstein, J. W. Jaworski, and A. I. Pesci, "A ratchet trap for Leidenfrost drops," *Journal of Fluid Mechanics,* vol. 696, pp. 215-227, 2012.

[39] Q. Li, Q. J. Kang, M. M. Francois, and A. J. Hu, "Lattice Boltzmann modeling of self-propelled Leidenfrost droplets on ratchet surfaces," *Soft Matter,* vol. 12, no. 1, pp. 302-12, Jan 07 2016.

[40] J. T. Ok, E. Lopez-Oña, D. E. Nikitopoulos, H. Wong, and S. Park, "Propulsion of droplets on micro- and sub-micron ratchet surfaces in the Leidenfrost temperature regime," *Microfluidics and Nanofluidics,* vol. 10, no. 5, pp. 1045-1054, 2010.

[41] A. G. Marin, D. A. del Cerro, G. R. B. E. Romer, B. Pathiraj, A. H. in 't Veld, and D. Lohse, "Capillary droplets on Leidenfrost micro-ratchets," (in English), *Physics of Fluids,* vol. 24, no. 12, Dec 2012, Art. no. 122001.

[42] G. Dupeux, P. Bourrianne, Q. Magdelaine, C. Clanet, and D. Quere, "Propulsion on a superhydrophobic ratchet," *Sci Rep,* vol. 4, p. 5280, Jun 13 2014.

[43] G. Dupeux, M. Le Merrer, C. Clanet, and D. Quere, "Trapping Leidenfrost Drops with Crenelations," *Phys Rev Lett,* vol. 107, no. 11, p. 114503, Sep 09 2011.

[44] G. G. Wells, R. Ledesma-Aguilar, G. McHale, and K. Sefiane, "A sublimation heat engine," *Nat Commun,* vol. 6, p. 6390, Mar 03 2015.

[45] A. Cole, B. Jury, and K. Takashina, "A Leidenfrost Thermostat," *Journal of Heat Transfer,* vol. 137, no. 3, p. 034502, 2014.

[46] A. Hashmi, Y. Xu, B. Coder, P. A. Osborne, J. Spafford, G. E. Michael, G. Yu, and J. Xu, "Leidenfrost levitation: beyond droplets," *Sci Rep,* vol. 2, p. 797, 2012.

[47] G. Dupeux, T. Baier, V. Bacot, S. Hardt, C. Clanet, and D. Quéré, "Self-propelling uneven Leidenfrost solids," *Physics of Fluids,* vol. 25, no. 5, p. 051704, 2013.

[48] R. L. Agapov, J. B. Boreyko, D. P. Briggs, B. R. Srijanto, S. T. Retterer, C. P. Collier, and N. V. Lavrik, "Asymmetric Wettability of Nanostructures Directs Leidenfrost Droplets," *Acs Nano,* vol. 8, no. 1, pp. 860-867, Jan 2014.

[49] R. L. Agapov, J. B. Boreyko, D. P. Briggs, B. R. Srijanto, S. T. Retterer, C. P. Collier, and N. V. Lavrik, "Length scale of Leidenfrost ratchet switches droplet directionality," *Nanoscale,* vol. 6, no. 15, pp. 9293-9, Aug 07 2014.

[50] C. Kruse, I. Somanas, T. Anderson, C. Wilson, C. Zuhlke, D. Alexander, G. Gogos, and S. Ndao, "Self-propelled droplets on heated surfaces with angled self-assembled micro/nanostructures," *Microfluidics and Nanofluidics,* vol. 18, no. 5-6, pp. 1417-1424, 2015.

[51] J. Li, Y. Hou, Y. Liu, C. Hao, M. Li, M. K. Chaudhury, S. Yao, and Z. Wang, "Directional transport of high-temperature Janus droplets mediated by structural topography," *Nature Physics,* vol. 12, no. 6, pp. 606-612, 2016.

[52] D. Soto, G. Lagubeau, C. Clanet, and D. Quéré, "Surfing on a herringbone," *Physical Review Fluids,* vol. 1, no. 1, 2016.

[53] L. E. Dodd, P. Agrawal, M. T. Parnell, N. R. Geraldi, B. B. Xu, G. G. Wells, S. Stuart-Cole, M. I. Newton, G. McHale, and D. Wood, "Low-Friction Self-Centering Droplet Propulsion and Transport Using a Leidenfrost Herringbone-Ratchet Structure," (in English), *Physical Review Applied,* vol. 11, no. 3, Mar 27 2019.

[54] J. M. Arter, D. J. Cleaver, K. Takashina, and A. T. Rhead, "Self-propelling Leidenfrost droplets on a variable topography surface," (in English), *Applied Physics Letters,* vol. 113, no. 24, Dec 10 2018.

[55] Mathworks. (9/10/2017). *Motion-Based Multiple Object Tracking*. Available: http://uk.mathworks.com/help/vision/examples/motion-based-multiple-object-tracking.html

Appendix 1: Self-Propelling Leidenfrost Droplets on a Variable Topography Surface [54]

The following pages are a copy of the paper published on this work in Applied Physics Letters.

Self-propelling Leidenfrost droplets on a variable topography surface

James M. Arter,[1] David J. Cleaver,[1] Kei Takashina,[2] and Andrew T. Rhead[1,a)]
[1]Department of Mechanical Engineering, University of Bath, Bath BA2 7AY, United Kingdom
[2]Department of Physics, University of Bath, Bath BA2 7AY, United Kingdom

(Received 13 September 2018; accepted 21 November 2018; published online 12 December 2018)

Leidenfrost water droplets can self-propel on heated surfaces with ratcheted topography, a very useful characteristic for systems with excess heat where fluid flow without moving parts is desirable. Reliability and flow rate are significant concerns for such systems. Here, the effect of the surface profile on reliability and droplet velocity are investigated on a single device with a continuously adjustable millimetre-scale ratcheted surface. Conditions are described under which the droplet velocity can exceed 350 mm/s. The reliability of droplet propulsion is shown to be improved for ratchet geometries with an overhang. *Published by AIP Publishing.* https://doi.org/10.1063/1.5056249

Droplets on a heated surface in the Leidenfrost regime sustain sufficient vapour flow to levitate them, greatly reducing droplet-surface friction and evaporation time.[1] Asymmetrically ratcheted surfaces channel vapour flow beneath the droplets[2,3] (or sublimating solids such as dry ice[4–6]) asymmetrically enabling them to self-propel.

A recent experimental study[7] has found that qualitatively different behaviour can result from small changes in ratchet geometry. Thus, the effect of surface geometry on propulsion requires investigation. However, experimental work[3,7–9] has generally been limited by the need to fabricate a new surface for every different ratchet geometry. Similarly, theoretical and numerical models describing the physics of propulsion which have appeared in the literature[1,5,7,10–13] have considered only a few specific ratchet profiles. Hence, a comprehensive description of how droplet propulsion depends on the ratchet profile is still missing. In a similar vein, recent research has led to proof-of-principle temperature control, power generation, and transportation devices.[14–16] Such, and similar future, devices would benefit from increased physical understanding enabling control of flow velocity and improved flow reliability.

To this end, a device is presented whose surface geometry can be adjusted continuously. Data from twenty distinct ratchet configurations are presented, revealing conditions under which droplet velocity can exceed 350 mm/s and propel uphill. An overhang geometry is found to significantly improve propulsion reliability. The device (Fig. 1) consists of a frame that enables a stack of rectangular plates of steel to be tilted but also held rigidly. For each plate, two faces are exposed: the edge and a thin strip on the plate surface between the edge and the neighbouring plate. These faces act as the triangular periodic surface on which droplets are propelled. The angle, α, between the edge-flat and the plate's face is set by locking the plates at a specific incline β and then planarising the surface on a mill. The angle, β, can then be tuned without further machining [Fig. 1(c)] allowing a continuous range of ratchet geometries to be achieved. Slip between plates during the device setup inevitably leads to small relative variations in h (average standard deviation of 88 μm), and so, surface topography was confirmed by contact profilometry (supplementary material). Individual tooth faces have a roughness of 3.3 μm (supplementary material). Whilst surface roughness is known to have a significant effect on droplet motion,[14] this is believed to be secondary to the change in the surface topography here as the plates have been machined in the same manner each time α is changed. Figure 2 shows how the tooth height, h (see contours), and pitch, P, vary with α and β. Insets (i)–(xx) illustrate the range of periodic surfaces investigated in this study. Shaded regions indicate an overhang geometry, that is, there is space beneath the apex of each tooth, see (ii) and (vii).

During experiments the entire device was placed on a hotplate. Thermocouples inserted into holes drilled into the side of the plates [Fig. 1(b)] were used to monitor plate temperature. The hotplate was clamped onto a single axis tilting stage to control the incline, γ, which in turn was mounted on an angle-adjustable stage for fine adjustment. A peristaltic pump was used to dispense 57 ± 3 mg droplets of de-ionised water (giving them a radius slightly below the capillary length of water) at a rate of 4–5 drops per minute, whilst the device temperature was slowly increased ($200 < T < 350\,^{\circ}$C). A video of each droplet was recorded using a Nikon D750 camera with a 28 mm lens. The position of droplets as a function of time was extracted from the videos via a modified Matlab script[17] which binarises the extracted images and returns the droplet's geometric centre.

Not all droplets followed the intended trajectory. Velocity data were only extracted for droplets propelled across the entire length of the device (in the direction of downward incline of the larger of the two tooth-faces [Fig. 1]). For all droplet paths captured, the droplet initially accelerated rapidly over a few ratchet teeth before reaching an approximately steady velocity (supplementary material).

For most surface profiles (Fig. 3), droplet velocity initially increases with temperature, peaks around 270–300 °C, and then decreases. This pattern can be broadly explained in terms of four factors: (a) vapour layer thickness; (b) rate and direction of vapour flow; (c) droplet deformation; and (d) wetting contact. That is, in the high temperature limit, deep in the Leidenfrost regime, the vapour layer beneath a droplet is complete and supports the droplet. With reducing temperature, the

a)Author to whom correspondence should be addressed: a.t.rhead@bath.ac.uk

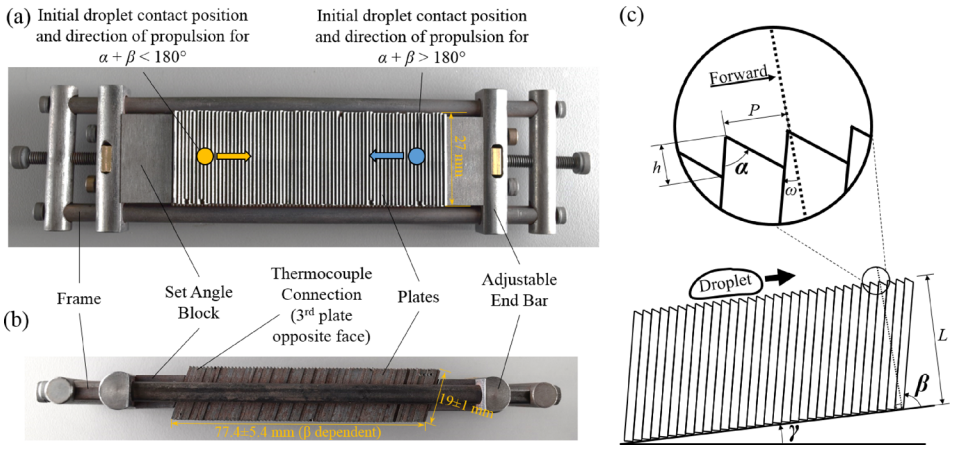

FIG. 1. The device is formed of 1 mm thick plates each with an initial height of ~20 mm. (a) Plan and (b) side views of the device; (c) conveys key variables, ω is negative in this diagram.

vapour layer thins, leading to stronger interaction with the teeth.[8,11] This can be expected to lead to stronger propulsion as the forward flow of vapour between the teeth below a droplet is closer to its surface (enhancing drag) and more of the flow is in the forward direction.[5,7] However, droplets also deform further in the ratcheted surface at lower temperatures, leading to dissipation of translational kinetic energy (TKE).[18] In the low temperature limit, with a thin vapour layer, teeth may penetrate the droplet surface and wetting and transition boiling may affect droplet dynamics. This might enhance traction[3] but could also lead to dissipation of TKE and complications preventing desired propulsion.

Up to a limit, small tooth heights, e.g., (α, β) = (92.3°, 84.0°), (82.0°, 90°), (73.7°, 98.5°), (73.7°, 90°), and (64.9°, 109.5°), produce the highest velocities peaking at ~350 mm/s in the range of 275–300 °C. This is higher than that previously

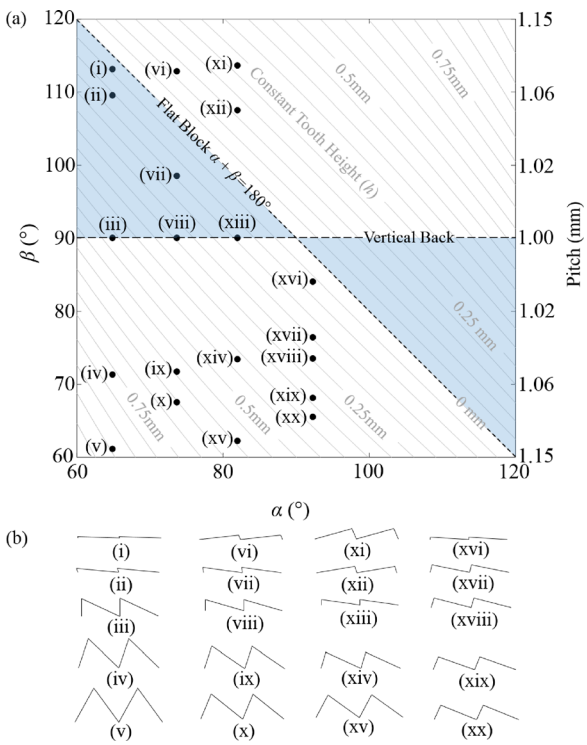

FIG. 2. (a) Tooth height and pitch given by varying α and β within the limits of the device. Curves indicate configurations with constant tooth height h. Shaded regions indicate teeth with an overhang geometry. (b) Example tooth geometries from (a).

reported for similar size ratchets[1,2,8] and droplets.[11] This is expected to be due to minimised dissipation of TKE and an optimum ratio of forward to reverse flow under the droplet. However, data for a very small tooth height, (α, β) = (64.9°, 113.1°) in Fig. 3(d), shows a peak velocity at ~230 °C. It is assumed that this almost flat geometry reaches the Leidenfrost limit at a lower temperature and is unable to create strong propulsive force. For this profile, higher temperatures produce sufficient vapour flow to create a vapour layer thick enough to reduce droplet/teeth interaction. Forward flow is also thought to be reduced owing to increased outflow.

Conversely, deep troughs between teeth (largest tooth heights), e.g., (α, β) = (82.0°, 73.4°), (73.7°, 71.7°), (73.7°, 76.5°), (64.9, 90), and (64.9°, 71.3°), produced comparatively low velocities and had less reliable behaviour in the low temperature range. This is due to the transition boiling region extending to higher temperatures owing to a thicker vapour layer being required to both prevent penetration of the teeth and to provide sufficient forward flow for propulsion.[19]

An overhang profile, described by the angle ω, where $\omega > 0$ indicates overhang, $\omega = 0$ no overhang, and $\omega < 0$ anti-overhang [see Fig. 1(c)] can be used to further parametrise teeth. Teeth with $\omega < 0$ generally have a smaller operating temperature range, e.g., (α, β) = (92.3°, 84.0° and 76.4°, 73.5°), (82.0°, 107.5°, and 73.4°), (73.7°, 71.7°, and 67.5°), and (64.9°, 71.3°), and also exhibit a larger scatter of results hinting at less stable flow dynamics, e.g., (73.7°, 67.5°) and (64.9°, 71.3°).

Reliability of propulsion (greyscale in Fig. 4) is quantitatively assessed by considering the proportion of droplets successfully propelled within a temperature band. Figure 4 shows reliability in seven different temperature bands for α and β axes that map directly onto Fig. 2. For no incline ($\gamma = 0°$), data points within the boundaries of the shaded (overhang) region strikingly show 100% reliability. The extent of this reliable region (w.r.t. α and β) is generally greatest in the temperature range of 250–270 °C, shrinking at higher/lower temperatures.

The second and third rows of Fig. 4 show data taken at inclines of $\gamma = 2.5°$ and 5°. Consistent with our previous work,[3] the temperature range over which propulsion is reliable reduces with increasing incline. Regions where propulsion is maintained with increasing incline correlate with the shaded triangular region (indicating an overhang profile) although the reliable region is reduced.

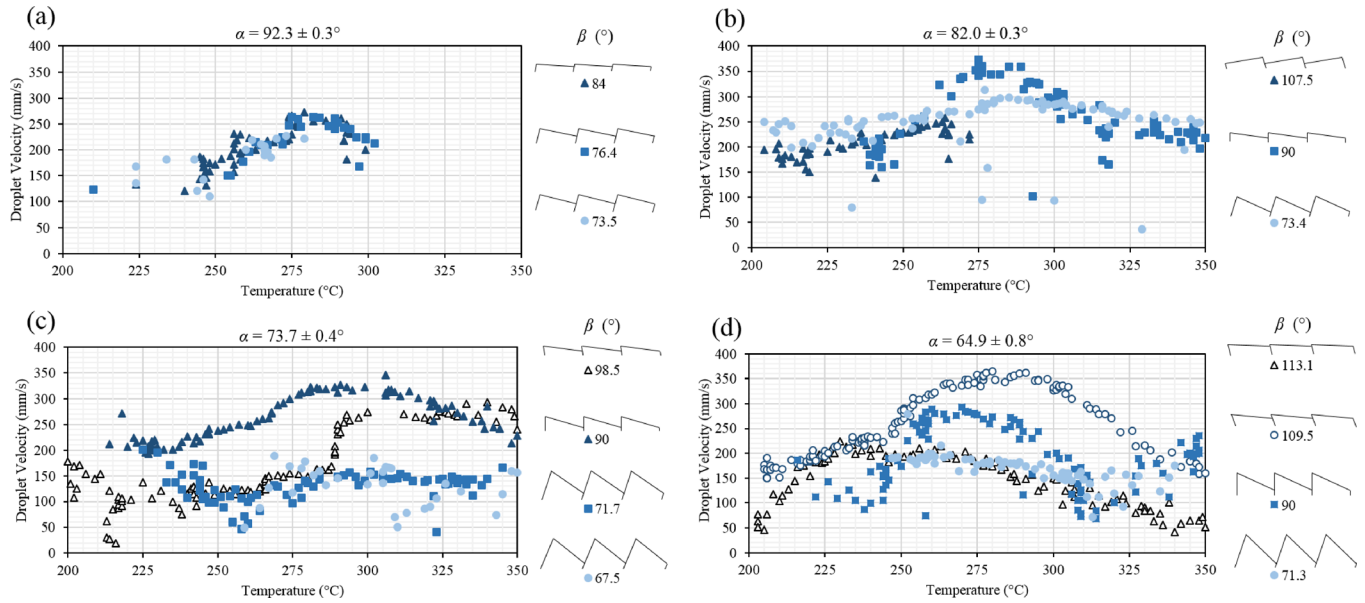

FIG. 3. Velocity of propelled droplets for various ratchet profiles. (a) $\alpha = 92.3°$, (b) $\alpha = 82.0°$, (c) $\alpha = 73.7°$, and (d) $\alpha = 64.9°$. Inclination, γ, is 0° for all plots. Open markers denote the surfaces with $\omega > 0°$, i.e., overhanging teeth.

It is hypothesised that an overhang profile enhances reliability by changing the flow of vapour beneath the droplets[4,5,13] (Fig. 5). Here, following the work of Cousins *et al.*,[13] an ANSYS™ computational fluid dynamics (CFD) model of an infinitely long but finite width dry ice puck above a ratcheted surface is used to investigate the effect of overhang on general flow behaviour. This puck model specifically removes complications such as droplet surface distortion (Fig. 5), ripples, and internal retro-rolling flow leaving purely the effect of vapour flow. The 5 mm wide puck has an inlet boundary on the base with a flow rate of CO_2 of 0.15 m/s. A symmetry boundary condition at the mid-width and periodic boundary conditions in the x-direction (effectively making the puck infinite length) reduce computational effort. Full details of the simulation method are available in the supplementary material. In order to address the effects of overhang ω, teeth with a constant pitch and slope of the longer horizontal surface are considered. ω is varied by changing the slope of the shorter vertical surface (Fig. 5).

The average shear stress, $\langle \tau_i(j) \rangle_k$, shown in Figs. 5 and 6(b) is the shear stress in direction i averaged (where $\langle\ \rangle$ is the arithmetic mean) over k for each location j, see supplementary material for details. In Fig. 6(a), total shear stress, $\langle \tau_x \rangle_{\text{total}}$, associated with the viscous force acting on the base of the puck, is calculated by dividing the sum of the x forces acting on the base by the base area.

Comparison of orange areas in Fig. 5 shows that, with increasing overhang, the region of positive u-velocity increases in size as flow propagates into the overhang and the region of negative u-velocity diminishes. As a result, the region of positive shear force increases in size, while the region of negative shear force reduces, leading to an increase in total shear force [Fig. 6(a)]. Figure 6(b) shows that this behaviour is consistent across all z locations. Furthermore, Fig. 6(c) shows that as ω increases, y force decreases. This is due to the increasing outflow area with increasing ω reducing the magnitude of w-velocity as shown in Fig. S16 in the supplementary material. The consequent reduction in y-force

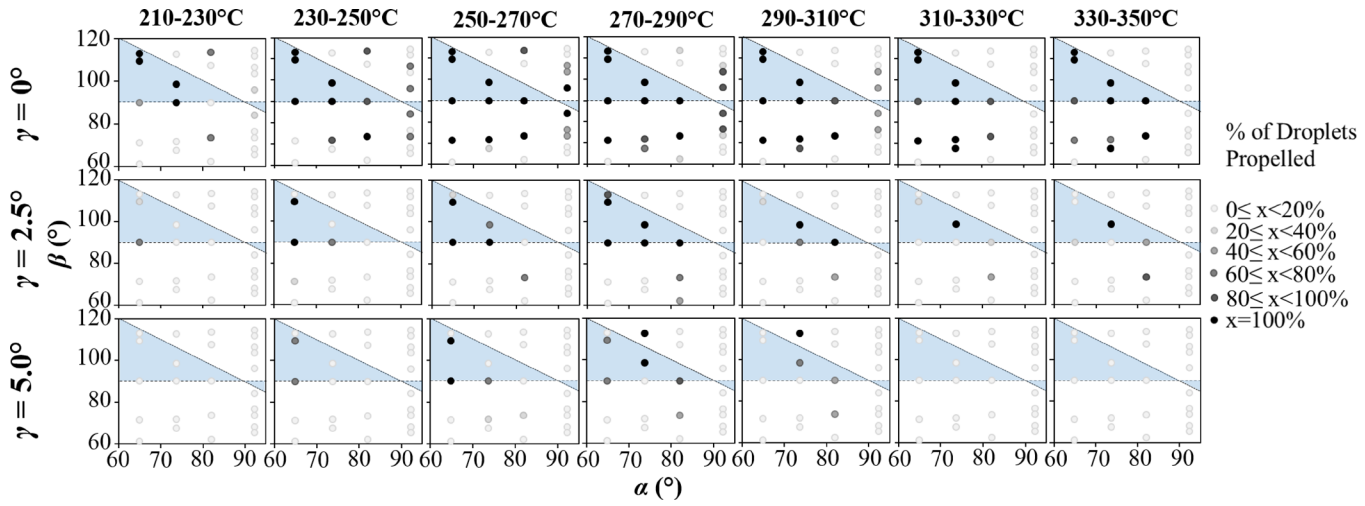

FIG. 4. Percentage of droplets propelled for 20 °C temperature bands (columns) and inclinations γ (rows).

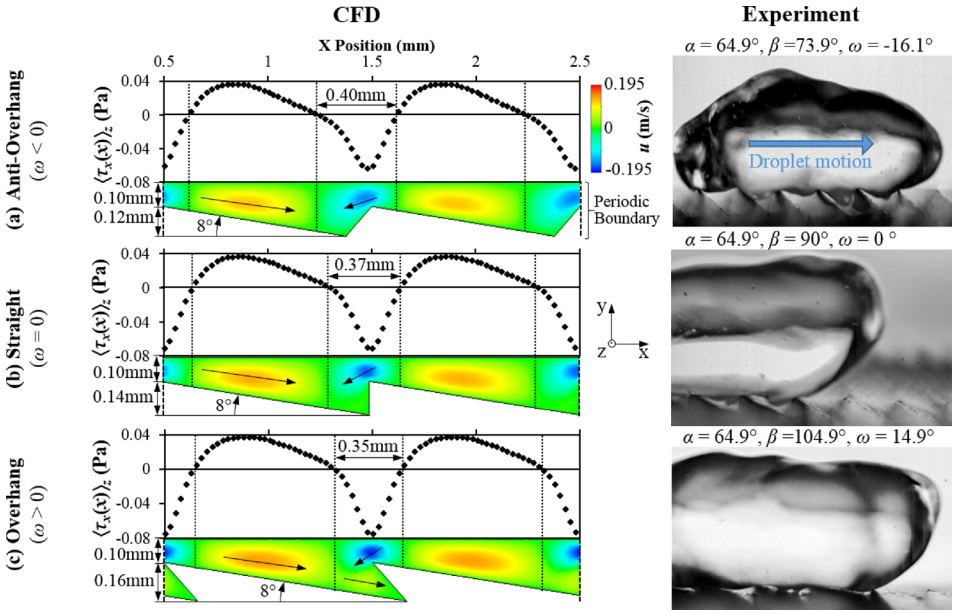

FIG. 5. CFD images of flow velocity u in the x-direction and results for $\langle \tau_x(x) \rangle_z$ together with images of droplets for tooth geometries with (a) $\omega < 0$, (b) $\omega = 0$, and (c) $\omega > 0$. CFD data are from the x-y plane halfway between the symmetry plane and the edge of the block. Arrows indicate the flow direction.

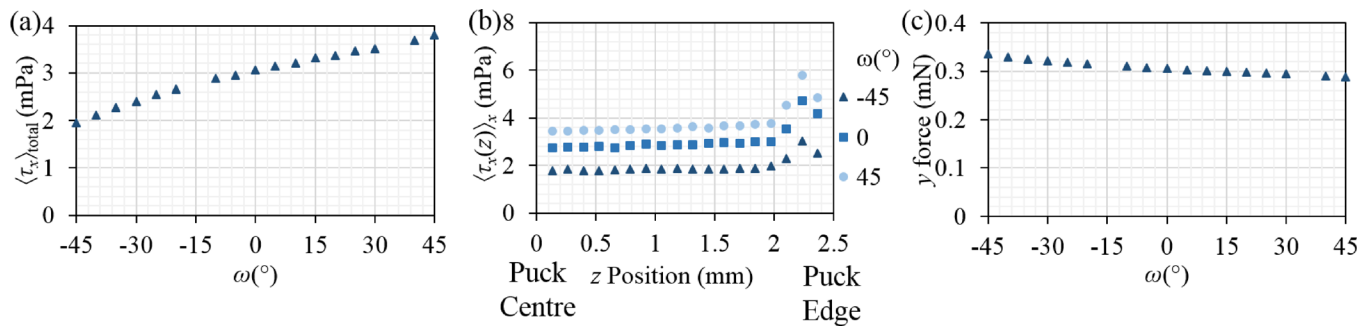

FIG. 6. CFD data for (a) $\langle \tau_x \rangle_{\text{total}}$ as a function of ω, (b) $\langle \tau_x(z) \rangle_x$ as a function of z position, and (c) y force as a function of ω.

would result in the distance between the puck/droplet surface reducing until vertical equilibrium is reached, likely further increasing x-force. In addition, the reduction in w-velocity will reduce the magnitude of shear in the z-direction, see S17 of the supplementary material. For the symmetric case, this is inconsequential; however, when considering reliability, Bouillant *et al.* have experimentally shown that Leidenfrost droplets can be subject to symmetry breaking resulting from vapour flow.[20] Based on the results presented in Figs. 5 and 6, it is hypothesized that overhang could bias the droplet towards propulsion in the x-direction, thereby improving reliability, through three effects: (i) stronger x-shear force; when the droplet is accelerating from zero velocity, the larger u-component of velocity and the resulting larger shear force shown in Fig. 5(c) create a strong bias. (ii) Reduced z-shear force; the overhang creates an "escape route" for flow beneath the droplet that reduces the magnitude of lateral velocity, further increasing the relative bias in the x-direction. (Supplementary material, S16 and S17). (iii) Reduced lateral tilt; the reduced lateral velocity makes it less probable that the droplet will tilt laterally (Bouillant *et al.*) accelerating the droplet in the z-direction. (Supplementary material, S17).

To conclude, a device has been demonstrated whose ratcheted surface topography can be changed continuously. Specifically, it enables tooth geometries with overhang. Such tooth profiles, as a consequence of reducing vapour flow in the opposite direction to droplet motion, lead to a dramatic improvement in the reliability of propulsion over a wide range of operating conditions, an important feature for future industrial uptake. The device and supporting CFD simulations also highlight the interplay of forward and outward flow enabling the identification of geometries under which droplets self-propel with speeds in excess of 350 mm/s.

See supplementary material for device geometry (S.I.), surface topography (S.II.), experimental procedure (S.III.), data acquisition and analysis (S. IV), further data analysis (S.V), and CFD details (S.VI).

The authors gratefully acknowledge the support of James Arter by the EPSRC (EP/M50645X/1) and thank Paul Reddish and Michael Linham for manufacturing support and Prof. Chris Bowen for his help with profilometry.

[1]D. Quéré, Annu. Rev. Fluid Mech. **45**(1), 197 (2013).
[2]H. Linke, B. J. Aleman, L. D. Melling, M. J. Taormina, M. J. Francis, C. C. Dow-Hygelund, V. Narayanan, R. P. Taylor, and A. Stout, Phys. Rev. Lett. **96**(15), 154502 (2006).
[3]A. Grounds, R. Still, and K. Takashina, Sci. Rep. **2**, 720 (2012).
[4]T. Baier, G. Dupeux, S. Herbert, S. Hardt, and D. Quere, Phys. Rev. E **87**(2), 021001 (2013).
[5]G. Dupeux, M. Le Merrer, G. Lagubeau, C. Clanet, S. Hardt, and D. Quéré, EPL **96**(5), 58001 (2011).
[6]A. Wuerger, Phys. Rev. Lett. **107**(16), 164502 (2011).

[7]Z. H. Jia, M. Y. Chen, and H. T. Zhu, Appl. Phys. Lett. **110**(9), 091603 (2017).
[8]J. T. Ok, E. Lopez-Oña, D. E. Nikitopoulos, H. Wong, and S. Park, Microfluid. Nanofluid. **10**(5), 1045 (2011).
[9]G. Dupeux, P. Bourrianne, Q. Magdelaine, C. Clanet, and D. Quere, Sci. Rep. **4**, 5280 (2014).
[10]G. Lagubeau, M. Le Merrer, C. Clanet, and D. Quéré, Nat. Phys. **7**(5), 395 (2011).
[11]A. G. Marin, D. A. del Cerro, G. R. B. E. Romer, B. Pathiraj, A. H. in 't Veld, and D. Lohse, Phys. Fluids **24**(12), 122001 (2012).
[12]Q. Li, Q. J. Kang, M. M. Francois, and A. J. Hu, Soft Matter **12**(1), 302 (2016).
[13]T. R. Cousins, R. E. Goldstein, J. W. Jaworski, and A. I. Pesci, J. Fluid Mech. **696**, 215 (2012).
[14]A. Cole, B. Jury, and K. Takashina, J. Heat Transfer **137**(3), 034502 (2015).
[15]G. G. Wells, R. Ledesma-Aguilar, G. McHale, and K. Sefiane, Nat. Commun. **6**, 6390 (2015).
[16]A. Hashmi, Y. Xu, B. Coder, P. A. Osborne, J. Spafford, G. E. Michael, G. Yu, and J. Xu, Sci. Rep. **2**, 797 (2012).
[17]See http://uk.mathworks.com/help/vision/examples/motion-based-multiple-object-tracking.html, for "Motion Based Multiple Object Tracking, Mathworks" (last acessed June 22, 2018).
[18]G. Dupeux, M. Le Merrer, C. Clanet, and D. Quere, Phys. Rev. Lett. **107**(11), 114503 (2011).
[19]J. D. Bernardin and I. Mudawar, J. Heat Transfer-Trans. ASME **121**(4), 894 (1999).
[20]A. Bouillant, T. Mouterde, P. Bourrianne, A. Lagarde, C. Clanet, and D. Quéré, "Leidenfrost Wheels," Nature Phys. 2018.